Near-real time volcano monitoring and modelling using radar interferometry

Karsten Hermann Spaans

Submitted in accordance with the requirements for the degree of
Doctor of Philosophy

The University of Leeds
School of Earth and Environment

July 2016

The candidate confirms that the work submitted is his own, except where work which has formed part of jointly authored publications has been included. The contribution of the candidate and the other authors to this work has been explicitly indicated below. The candidate confirms that appropriate credit has been given within the thesis where reference has been made to the work of others.

The work in Chapter 2 of the thesis has appeared in publication as follows:
Karsten Spaans and Andrew Hooper (2016), *InSAR processing for volcano monitoring and other near-real time applications*, Journal of Geophysical Research:Solid Earth, 21, doi:10.1002/2015JB012752.

The methodology presented in this paper was developed together with my co-author. I implemented and refined the method, and did the data processing, testing and validation. I also led the writing of the paper.

The work in Chapter 3 of the thesis has appeared in publication as follows:
Karsten Spaans, Sigrún Hreinsdóttir, Andrew Hooper and Benedikt Gunnar Ófeigsson (2015), *Crustal movements due to Iceland's shrinking ice caps mimic magma inflow signal at Katla volcano*, Scientific Reports, 5, doi:10.1038/srep10285.

Part of this work, namely the InSAR analysis, was done prior to starting my PhD. Besides the InSAR analysis, I did the the comparison to the GIA model, incorporating the GPS measurements, the modelling of the contracting signal, and led the writing of the paper. S.H. processed the GPS data. All authors contributed to the ideas presented in this paper, and its writing.

The work in Chapter 4 of the thesis is a manuscript to be submitted as follows: **Karsten Spaans** and Andrew Hooper, *Constraints on the crustal stress field from the 2014 Bárðarbunga rifting event.*

I performed the InSAR analysis and the modelling, as well as lead the writing of the paper.

The work in Chapter 5 of the thesis is a manuscript to be submitted as follows: **Karsten Spaans** and Andrew Hooper, *Sentinel-1 for large earthquakes: Application to the 2015 Chile and 2016 Ecuador earthquakes.*

I performed the InSAR analysis, calculated the spectral diversity azimuth offsets and did the modelling. I also led the writing of the paper.

Acknowledgements

Undoubtedly my supervisor, Andy Hooper, is the reason I was able to not only complete, but actually start this Ph.D. It has been eight years since I started working with Andy, and I am still not done learning from him. Let's assume it is because he has a lot to teach, not because I am a slow learner. Andy been a very understanding and supportive supervisor, and I wouldn't be half the scientist I am today without his help. Andy, thank you for everything you have done over the last few years, and I look forward to continue to work with you.

Arguably, I landed at the School of Earth and Environment, University of Leeds by chance. I remember the uncertainty of moving to an institute and city I knew little about, with the exception of a few people I had met at conferences and summer schools. Looking back, it turned out to be a blessing. I have found the institute and its people to provide a very stimulating work environment, and have thoroughly enjoyed the wide range of Earth science disciplines within the school. I would particularly like to single out the members of the tectonics, volcano and InSAR groups, for the interesting meetings and discussions. Special mentions of course go to Ekbal and David: you made the lunch breaks, conferences and general office life so much better. We'll keep in touch.

I would like to thank my colleagues at the FutureVolc project for the great science and interesting meetings. Some of the people that spring to mind are Michelle, Stéphanie, Vincent, Benni and many more. The FutureVolc project was tirelessly led by Freysteinn Sigmundsson. Freysteinn is one of those amazing scientists that can immediately see to the core and implications of research. I consider myself lucky to have been able to work with and learn from Freysteinn for two year during my stay in Iceland, as well as during my Ph.D. Freysteinn, you have my eternal gratitude for providing me with these opportunities.

I will never be able to repay the debt I owe my parents, Dirk and Gertrud, for the long, long years of support. While I wasn't the fastest ever student to complete his undergraduate degree, they never wavered in their belief and support. Mum, Dad, thank you so much for everything, and I look forward to the many visits and trips we will share in the future, accompanied by good food, drink and good humour.

Lastly and more importantly, my lovely wife, Amandine. It takes someone who has completed a Ph.D. to know how difficult it can be at times. I have been incredibly lucky to have you by my side, and I cannot begin to thank you for your support during the Ph.D., and the sacrifices you have made on our behalf. Our future is slowly taking shape, and I can't wait to see where it will lead us.

Abstract

Radar interferometry has become an important technique for studying volcanic activity. The dense sampling of centimeter to millimeter precision deformation measurements that can be achieved with the method has allowed us to study and quantify subsurface magma movements ever more effectively over the last two and a half decades. The current generation of satellites provides superior acquisition frequencies over volcanic areas, making it feasible for the first time to monitor volcanic areas in near-real time. However, this is only possible if we can process the data in a timely fashion, and requires a rethink of current processing strategies. Also, measuring the deformation signal is not enough; we need to infer from the surface measurements what is happening beneath the surface. This requires us to distinguish volcanic from non-volcanic signals, and to accurately model volcanic signals. In this thesis, I address the above challenges, with the ultimate goal of using InSAR to monitor volcanoes and other surface deforming process in near-real time, and to improve our ability to qualify and quantify signal sources.

The processing time and flexible ingestion of new images becomes critical when considering near-real time monitoring of volcanoes. I developed Rapid time series InSAR (RapidSAR), a new fast and flexible algorithm to estimate coherence and select points on an interferogram-by-interferogram basis. Compared to the conventional boxcar ensemble method, RapidSAR overcomes the severe limitations the method has in areas of marginal coherence. Alternative time series methods are typically slow and are unable to ingest new images without reprocessing the entire dataset. To calculate the individual coherence estimate for every point in each interferogram, I use an ensemble of points which show on average similar amplitude behaviour throughout the dataset, ensuring points within the ensemble have related scattering mechanisms. By assuming that the scattering behaviour of nearby points does not change rapidly in time, I can select the ensemble for each point on an initial set of interferograms, significantly reducing processing costs for newly acquired images, as only combinations that include the new image have to be considered. I show that the coherence estimate is superior to the boxcar method, and that the individual coherence estimate avoids the selection compromise that other time series methods suffer from. I also discuss the effectiveness of RapidSAR to extract deformation measurements in areas of marginal coherence, using the 2016 Ecuador earthquake as an example. Even though the coherence for the 24-day interferogram covering the earthquake is very poor, the signal extracted by RapidSAR is sufficient to constrain a first model of the slip on the fault, information vital to evaluate the current earthquake hazard in the area.

Ensuring that what we measure is actually magmatic in origin is critical when assessing volcano activity. When GNSS and InSAR measurements first became available in selected volcanic regions, many deformations were observed. However, a lack of coverage in space and time meant that limited information was available to determine the origin of observed deformations. I give an example of this at Katla volcano, Iceland, where, in the early 2000s, horizontal deformations were observed at two continuous GNSS stations on the south flank of the volcano, pointing away from the central part of the caldera. Combined with campaign measurements on the ice cap covering the volcano showing uplift, these deformations were interpreted as indicating large scale pressure increase in the magma chamber. The same deformations continued to be observed for several years, with the same interpretation lingering. I use InSAR and additional GNSS measurements collected between 2001 and 2010 to show that the horizontal motions observed at the two stations in fact follow the regional trend, and that no deformation signal that could be related to magma movements beneath Katla are detectable outside the ice cap. Instead, the horizontal motions follow the predictions of an ice unloading model well. Iceland is home to several large icecaps, including the largest icecap in Europe, Vatnajökull. Melting of ice at these icecaps leads to an isostatic rebound of the earth surface, resulting in uplift and movement away from the icecaps. When ice caps cover volcanoes, as is the case for many Icelandic volcanoes, this can mimic a volcanic signal, which is what happened at Katla between 2001 and 2010. With our rapidly expanding number of observations, we will be able to detect ever smaller deformation signals. This will also increase the number of nuisance signals, and careful evaluation of the source of the deformations will become both more challenging and important.

To translate any magmatic deformations we measure into interpretations and increase our understanding of the processes happening subsurface, models are required. Analytical models for simple geometries exist, and these can often be useful to provide fast approximate answers to questions like location and volume of magma movements involved. But, as I show for the propagating dike at the 2014/2015 Holuhraun eruption of Bárðarbunga, the resulting models are not always physically realistic. By using the Boundary Element Method (BEM), we can place stress constraints on the model directly, yielding more realistic answers to our questions. In the case of the Holuhraun dike, I use the BEM to show that a significant part of the opening at the tip of the dike was caused by external deviatoric stress as expected, due to plate spreading. However, in dike segments further south, I show that plate spreading has very little influence and internal overpressure of the magma with respect to the host rock alone can explain the observations.

The Sentinel-1 satellite constellation is expected to be the driving force that will take the use of InSAR for deformation measurements to the next level in the years to come, not just for volcano deformations, but for other applications as well. I use the 2015 Illapel, Chile earthquake and the 2016 Ecuador earthquake to explore some of three key potential advantages that Sentinel-1 offers us: i) The ability to cover large swaths ii) The ability to extract azimuth motions from burst and subswath overlap regions with high precision, and iii) High overall coherence due to consistently short revisit times. I show that the wide swath mode allows us to capture both large earthquakes in single interferograms. The Chile earthquake is imaged in great detail, demonstrating the benefit of short baseline combinations on coherence. On the other hand, the Ecuador earthquake clearly shows us that for particularly challenging areas, even 12-day coherence can be marginal. I show that coregistration issues related to the wide swath acquisition mode have been solved for most applications, although azimuth movements and/or ionospheric influence can still cause burst discontinuities, which may or may not hamper the phase unwrapping. The overlap regions of both burst and subswaths resulting from the TOPS acquisition mode offer us the possibility to detect azimuth offsets, which I demonstrate for the co-seismic deformation. For smaller scale azimuth offsets, I demonstrate that ionospheric signals hamper the accuracy of these signals, making it difficult to achieve the theoretical centimeter level precision predicted in previous works.

Contents

List of Figures

List of Tables

Nomenclature

List of acronyms

BEM	Boundary Element Modelling
DEM	Digital Elevation Model
EVZ	Eastern Volcanic Zone
GIA	Glacio-Isostatic Adjustment
GNSS	Global Navigation Satellite System
GPS	Global Positioning System
IGS	International GNSS Service
InSAR	Interferometric Synthetic Aperture Radar
LOS	Line Of Sight
MAP	Maximum a posteriori probability
MAR	Mid-Atlantic Ridge
ML	Maximum Likelihood
NVZ	Northern Volcanic Zone
PS	Persistent (also: Permanent) Scatterer
RP	Reykjanes Peninsula
SAR	Synthetic Aperture Radar
SB	Small Baseline
SHP	Statistically Homogeneous Pixel
SISZ	South Iceland Seismic Zone
TEC	Total Electron Content

TOPS	Terrain Observation by Progressive Scanning	
WVZ	Western Volcanic Zone	

List of symbols

ΔA	Amplitude difference	
Δf	Frequency difference	[Hz]
Δt_{azi}	Azimuth pixel time per pixel	[s]
ΔV	Volume change	[m^3]
γ	Coherence magnitude	
γ_c	Complex coherence	
ν	Poisson's ratio	
ϕ	Double difference phase difference	[rad]
ψ	TOPS sweep angle	[rad]
ρ	Distance projected on surface	[m]
σ^2	Variance	
θ	Look angle	[rad]
A	Amplitude	
c	Speed of light	[m/s]
D	Locking depth	[m]
d	Depth	[m]
k	Number of patches	
k_ψ	TOPS sweep angle rate	[rad/s]
M	Master image signal	
N	Number of points in ensemble	
p	Pressure	[Pa]
p_e	Excess pressure	[Pa]
p_o	Magma overpressure	[Pa]

R	Apparent ramp caused by oscillator drift	[m/yr]
S	Slave image signal	
T	Two-way travel time	[s]
T_d	Traction in dip-slip direction	[Pa]
T_n	Traction in normal direction	[Pa]
T_s	Traction in strike-slip direction	[Pa]
u	Displacement	[m]

Chapter 1

Introduction

Volcanic eruptions can cause massive disruptions on a regional to global scale, ranging from human casualties, destruction of building and infrastructure and economic disruptions. Perhaps the most well known disruptive eruption in recent memory is the 2010 Eyjafjallajökull eruption (*Sigmundsson et al.*, 2010a), which intermittently interrupted air traffic for several weeks and damaged the global economy for several billions of dollars. However, it is important to remember that this eruption was relatively small, and that a large scale eruption like the 1784 Laki eruption could have far more serious consequences, such as climate change and more wide-spread air closures (*Schmidt et al.*, 2012).

Monitoring volcanic activity in the form of subsurface magma movements allows us to prepare for and mitigate some of the disruptive effects of volcanic eruptions. Seismicity is often a good indicator of magmatic movements, but deformation monitoring can tell us more about the shape and volume of magma involved. A significant amount of volcanic systems around the world are monitored by continuous GNSS stations, but it is expensive to cover a volcano with sufficient stations to model magmatic movements with sufficient reliability. In fact, the majority of volcanoes are not monitored at all. Radar interferometry is an opportunistic spaceborne method, that has the advantage of not requiring any equipment on the ground. It can measure surface deformations accurately, with very dense spatial sampling. Often used in conjunction with GNSS measurements (if available), the radar interferometry method has been proven to be a game changer for studying earth surface movements over the last two decades.

However, measuring earth surface deformations is not sufficient; we need to also interpret the signal and relate it to what might be happening beneath the surface. First of all, we must be certain the measured deformations are actually due to magmatic activity. Any nuisance signals must be identified and either corrected, or taken into account during the modelling. Secondly, we need to quantify the magmatic activity by accurately modeling any magmatic signals we detect, and classify the uncertainties involved.

This thesis is focused on using InSAR to monitor volcanoes and other processes in near-real time, and to improve our ability to qualify signal sources and quantify magmatic movements. The improved data quality and availability of recent radar satellites has made near-real time monitoring feasible for the first time, signalling a big leap forward for radar interferometry. The tools we need to take full advantage of this, however, still need development. In this chapter, I will provide background on relevant concepts in radar interferometry and volcano modelling. Tools developed in this thesis are being applied operationally over Iceland, and I will therefore follow up by giving a brief overview of volcanism in Iceland, highlighting three volcanic systems in particular. I will conclude this chapter by describing the aims and objectives of my thesis, and providing a roadmap for the remainder of this thesis.

1.1 Radar interferometry

The Interferometric Synthetic Aperture Radar (InSAR) method allows the retrieval of surface deformations with centimeter to millimeter level precision. It achieves this by interfering two radar images of the same scene (*Bamler and Hartl*, 1998, *Hanssen*, 2001). The phase component of the resulting interferometric signal is dominated by a topographic phase signal, caused by the difference in position of the satellite platform at the time of acquisition. This signal is however trivial to remove if the position and topography are known. What remains largely reflects surface deformations (*Hanssen*, 2001). One of the main advantages InSAR has over other techniques is that it can have near-global coverage, with very dense spatial sampling, without requiring equipment in the field. This has made InSAR a valuable technique in studying surface deforming natural hazards (e.g. (*Wright et al.*, 2001, *Sigmundsson et al.*, 2010b, *Sigmundsson* et al., 2015, *González et al.*, 2015, *Elliott et al.*, 2016)). Current SAR satellites that provide InSAR capable data include the ESA Sentinel-1 satellite, the DLR TerraSAR-X satellite, the ASI Cosmo-Skymed satellite, the CSA Radarsat satellite and the JAXA ALOS-2 satellite. These satellites allow us to study surface deformation better than ever before, increasing our ability to understand the processes behind the deformations. In this section I will give a basic overview of the InSAR technique, followed by a more in-depth review of several properties and processing techniques relevant for this thesis, before ending with a description of the Sentinel-1 satellite, the successful launch and commissioning of which has paved the way for a new era in InSAR applications.

1.1.1 InSAR overview

As mentioned above, the basic InSAR technique works by interfering two radar images. Before two images can be interfered, they first have to be in the same geometry. Due to small differences in satellite position of the two acquisitions, the two images, usually referred to as the master and the slave image, are slightly shifted with respect to each other. The offset between the master and slave is estimated in a process called co-registration, traditionally done by coherent cross-correlation (*Brown*, 1992). The slave image is resampled to the geometry of the master image, after which the two images can be interfered by multiplying the complex signal of each master image pixel with the complex conjugate of the corresponding pixel in the slave image. The phase of the resulting complex interferogram contains the deformation measurements. It however also contains several nuisance terms. For deformation measurements, one of these nuisance terms was already mentioned above, the signal caused by the difference in position of the platform of the two acquisitions which causes a change in range (*Hanssen*, 2001). This component of the interferometric phase is a function of the difference in position of the satellite at the time of acquisition, and the shape of the target surface (*Bamler and Hartl*, 1998), both of which are approximately known. For convenience, the correction of the effect is done in two steps. The first step corrects the component of the phase resulting from a reference ellipsoid (e.g. WGS84). The resulting phase is usually referred to as the “flat-earth” phase. The flat-earth phase still contains the phase resulting from topography, which is corrected using a Digital Elevation Model (DEM). The resulting interferometric phase contains the deformation signal, plus several additional nuisance terms like atmospheric and ionospheric delays and components due to orbital or DEM inaccuracies. These terms are usually either removed in post-processing, or included in the error budget during modelling.

The radar technique measures range in the radar line of sight (LOS). The interferometric phase measures the difference in this range between the two images. Consequently, the deformation signal present in interferograms only measures the component of the deformation in the LOS of the radar system. Current and past SAR satellites are or were all in near-polar orbits, with the radar antenna looking sideways at a 90 degree angle, as well as under an incidence angle from nadir direction. This means that InSAR measurements are sensitive to vertical movements, as well as movements approximately in an east-westward direction. Standard interferometry is far less sensitive to movements in north-south direction at most latitudes, since the satellite flight path is almost north-south, except at very high latitudes (*Wright et al.*, 2004).

One of the major sources of noise is due to decorrelation. Every resolution element is typically made up of many individual scatterers, and the radar signal scattered back towards the satellite by each resolution element is the coherent sum of the signal reflected by each scatterer. InSAR relies on the scattering properties of each resolution element to stay constant between the two acquisitions, to ensure the coherent summation is consistent between the two acquisitions. If this is not the case, decorrelation noise is introduced to the signal, which can happen for three reasons: 1) The individual scatterers change, 2) A difference in position of the satellite at the times of the two acquisitions or 3) A change in central Doppler frequency between the two acquisitions. All three reasons change the coherent summation of all scatterer contributions within

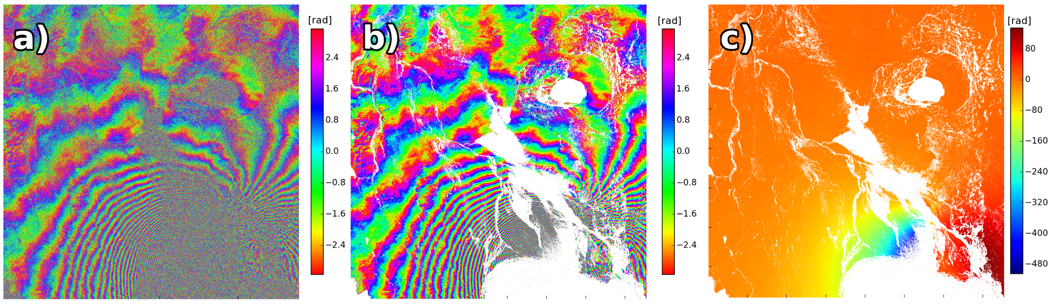

Figure 1.1: Examples of an interferogram during different stages of processing. The interferogram (20140813-20140829) covers pre-eruptive deformation associated with the 2014 Bárðarbunga rifting episode (see (*Sigmundsson* et al., 2015) and Chapter 4). Panel a) shows the full wrapped interferogram. Panel b) shows the same wrapped interferogram with decorrelated points removed. Panel c) shows the unwrapped phase of the points in panel b). SAR data provided by the Italian Space Agency (ASI) under the Supersite initiative.

the resolution element, leading to a random phase difference being introduced into the signal (*Zebker and Villasenor*, 1992). Fig. 1.1 a) shows an example of decorrelation noise mixed with the interferometric signal.

As the phase component of the radar signal is *modulo* 2π, the same holds for the interferometric phase. The phase values are said to be “wrapped”, resulting in interferograms displaying a cyclical pattern of phase values, referred to as fringes (see Fig. 1.1 a) and b)). Ideally, we would like the measurements to form a continuous deformation field. The process of estimating a continuous deformation field from the wrapped interferograms is known as phase unwrapping. Algorithms exist to unwrap the phase, e.g. (*Chen and Zebker*, 2001), but these solutions are non-unique. Therefore, phase-unwrapping remains one of the largest challenges in InSAR processing. An example of an unwrapped interferogram can be seen in Fig. 1.1 c). Another consequence of the phase only being known *modulo* 2π is that the absolute number of phase cycles between the satellite and the target is unknown. The InSAR measurements can therefore not be directly linked to a global reference frame, and thus represent relative measurements. Typically, a reference area is selected in an interferogram, for which deformations are either assumed to be zero, or some other known value. All other measurements in the scene can then be interpreted as movements relative to the reference area.

1.1.2 Coherence

As discussed above, InSAR is an opportunistic technique which relies on the scattering characteristics of resolution elements to stay consistent between acquisitions. Changes in the scattering properties leads to decorrelation noise. It is therefore important to have a measure of quality for each resolution element in the interferogram. The quality is usually given as a number known as coherence magnitude. Coherence is a measure of the amount of complex correlation, and is defined as (*Just and Bamler*, 1994):

$$\gamma_c = \frac{E\left(M \cdot \bar{S}\right)}{\sqrt{E\left(M \cdot \bar{M}\right) \cdot E\left(S \cdot \bar{S}\right)}}, \tag{1.1}$$

where $E()$ is the expectation operator, M is the complex radar signal in the master image, S is the complex radar signal in the resampled slave image and the bar represents the complex conjugate. The coherence magnitude for each point can have a value between 0 (no correlation) and 1 (full correlation), and is usually estimated using an ensemble of points in a two dimensional boxcar window surrounding the point in question (*Touzi et al.*, 1999):

$$\hat{\gamma} = \frac{\left|\frac{1}{N}\sum_{i=1}^{N} M_i \cdot \bar{S}_i\right|}{\sqrt{\frac{1}{N}\left(\sum_{i=1}^{N} M_i \cdot \bar{M}_i \sum_{i=0}^{N} S_i \cdot \bar{S}_i\right)}}, \tag{1.2}$$

where N represents the number of points in the window.

The boxcar method has three main drawbacks. First, it suffers from a resolution problem. Points within the ensemble have different scattering characteristics, and those points with high amplitude (e.g. buildings or natural ridges) dominate the coherence estimation. Neighbouring points use nearly the same mix of points within the ensemble, leading to a smearing out of these features. Second, it tends to overestimate the coherence of a large amount of fully decorrelated points because of the random signal being similar for neighbouring points by chance. As neighbouring points have very similar ensembles, these features also smear out, exacerbating the issue (see Fig. 1.2). Third, as the method essentially measures the variability of phase within the window, any non-constant signal biases the coherence estimation, with high phase gradients leading to low coherence estimates.

1.1.3 Time series analysis

Two of the main problems with single pair interferometry are the relatively low accuracy (cm level) compared to GNSS and leveling, and the decorrelation noise discussed in the previous section. Both of these problems are addressed by time series processing methods. As the name suggests, time series processing takes advantage of a series of interferograms in time, to select the points which remain coherent throughout. Time series techniques can be divided into two broad categories: The first category focuses on pixels in the radar images that have a dominant scatterer, an object which produces a large amplitude signal, dominating the coherent summation of scatterers within the resolution cell. These pixels are known as permanent or persistent scatterers (PS). Interferograms are formed with respect to a single master image, and PS are selected, depending on the method used, on their amplitude and/or phase behaviour throughout

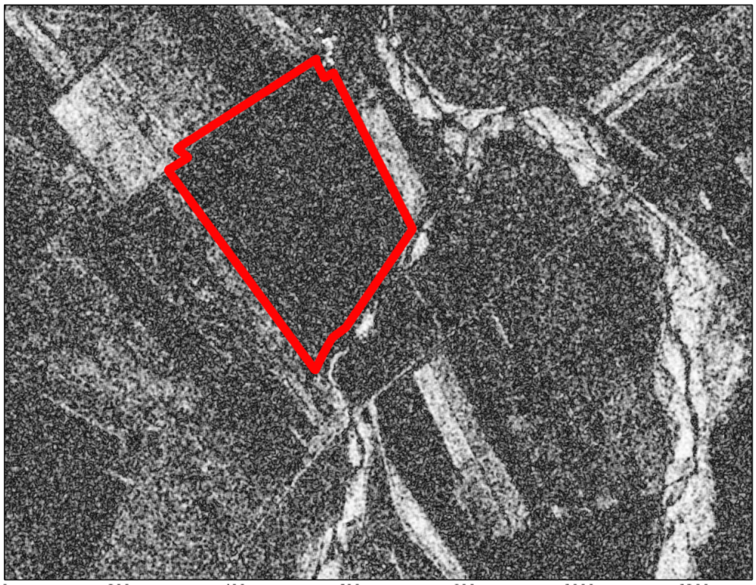

Figure 1.2: Example of a coherence estimate using the boxcar method. White points have coherence close to 1, black point coherence close to 0. High frequency noise is caused by neighbouring points being similar by chance, or strong scatterers dominating the estimation ensemble. This leads to many erroneously high coherence estimates in decorrelated areas, e.g. in the field outlined in red.

the time series. Examples of this category of techniques can be found in *Ferretti et al.* (2001) and *Hooper et al.* (2007). The second category of InSAR time series methods focuses on pixels that decorrelate relatively slowly in time, often referred to as distributed scatterers, as they are typically not dominated by a single strong scatterer. These methods form interferograms from a (redundant) network of images that are close-by in time and space (as in position of the satellite at the acquisition times), selecting points that show good signal-to-noise ratios throughout every interferogram. Examples of this category are given by *Berardino et al.* (2002), *Schmidt and Bürgmann* (2003) and *Hooper* (2008).

A more recent development in timeseries InSAR processing is the SqueeSAR algorithm (*Ferretti et al.*, 2011). This method, and several methods that were developed after it (e.g. *Fornaro et al.* (2015)), aim to combine persistent and distributed scatterer processing in a novel way. They identify neighbouring points with the same or similar scattering mechanism by looking at the amplitude behaviour of points in a time series of interferogram. We refer to these points with similar behaviour as "siblings" in this text. The SqueeSAR method uses any given group of siblings to estimate the sample covariance matrix (*Ferretti et al.*, 2011). For distributed scatterers, which are groups containing a large number of siblings, the covariance matrix is used to estimate the maximum likelihood phase value for the entire ensemble. This maximum likelihood (ML) phase value replaces all the siblings in the ensemble, essentially filtering the interferogram, taking scattering mechanism into account. The filtered interferograms are then processed using a conventional PS algorithm. Especially in rural areas, the algorithm significantly increases the amount of information extracted from the time series compared to PS techniques, without the need to pre-select a network of interferograms with favourable baselines and thus limiting information. However, the need for iterative methods in obtaining the ML phase values comes at the cost of a large increase in processing time.

1.1.4 Azimuth displacements

As mentioned earlier, one of the limitations of InSAR is that deformation measurements are limited to the radar line-of-sight. Due to the orbital properties of SAR satellites, the two viewing geometries available from ascending and descending groundtracks only differ by 15-25 degrees at most latitudes, resulting in conventional InSAR being hardly sensitive to ground displacements in the north-south direction (*Wright et al.*, 2004). This limitation is somewhat overcome by using amplitude offset tracking using correlation methods (*Michel et al.*, 1999), which yield offsets with decimeter level accuracy. *Bechor and Zebker* (2006) proposed a the multiple aperture InSAR method, with somewhat improved precision at the sub-decimeter level. The multiple aperture InSAR method for measuring displacements is the same as the earlier proposed spectral diversity method for coregistering SAR images (*Scheiber and Moreira*, 2000). Spectral diversity splits the azimuth bandwidth of both the master and slave SAR images into two distinct bands, essentially creating a forward and backward looking image for both the master and slave acquisitions. The two forward images are interfered, as are the two backward images, creating a forward looking and a backward looking interferogram. The two interferograms are then interfered with each other, creating a double difference interferogram. As atmospheric, topographic and LOS deformation signals are present in both the forward and backward looking interferograms, taking the double difference removes them (*Scheiber and Moreira*, 2000, *Bechor and Zebker*, 2006). However, as movements in azimuth direction, either from misregistration of deformation, are viewed from a slightly different angle by the forward and backward looking interferograms, they will create a phase offset in the double difference interferogram (*Scheiber and Moreira*, 2000, *Bechor and Zebker*, 2006). The precision of azimuth offsets depends on the azimuth bandwidth gap between the forward and backward looking SAR images, and precisions of several centimeters are possible (*Bechor and Zebker*, 2006).

1.1.5 Sentinel-1

The Sentinel-1A satellite was launched in April 2014, and has been operational since October of that year. Sentinel-1A offers a potential twelve day revisit cycle, which will be improved to six days with the recently-launched second satellite in the constellation, Sentinel-1B. This revisit time combined with the fact that the Sentinel-1s are specialist

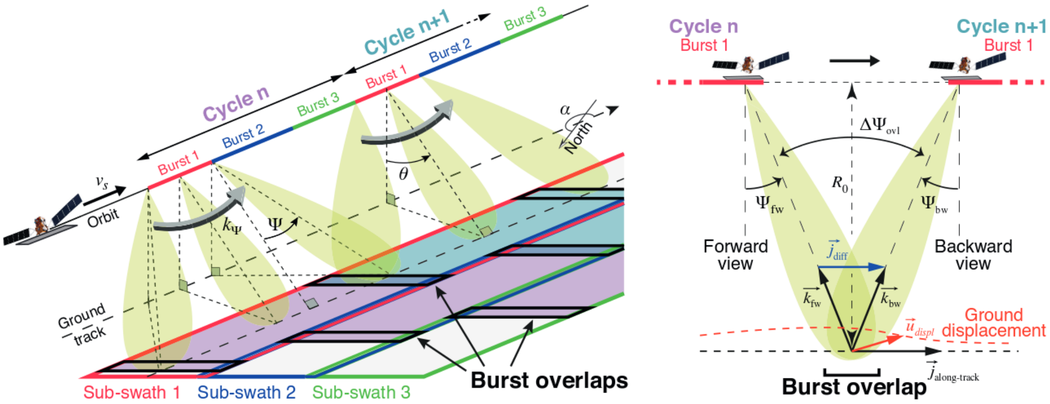

Figure 1.3: Principle of TOPS mode imaging. (left) TOPS-mode uses sweeping of the radar beam over the angle 2Ψ with an angular velocity of k_Ψ to illuminate a burst. When reaching the far end of the burst, the look angle θ is increased to illuminate a burst in the next subswath, and the process is repeated. After completing a burst sweep in all three subswaths, the next bursts in the first subswath is illuminated, starting the next cycle. (right) The bursts from subsequent cycles overlap. Due to the sweeping of the radar beam in azimuth direction, a difference in look angle $\Delta\Psi$ is present, resulting in a difference in Doppler frequency of data in the overlap region for subsequent cycles. This Doppler frequency difference can be used to detect azimuth movement, either apparent (misregistration) or real surface movement. Reproduced with permission from *Grandin et al.* (2016)

SAR satellites (i.e. they carry no other instrumentation on board like the previous ERS or EnviSAT missions) means that Sentinel-1 provides an unprecedented coverage of the Earth in space and time. It is different from many other missions in that it is operational in nature, as opposed to scientific. Finally, and perhaps most importantly, data acquired by the Sentinel system are freely available, opening up a host of opportunities that were previously unfeasible due to cost or lack of data.

Part of the reason why Sentinel-1 is able to achieve these short revisit times is the fact that it uses a wide swath mode, allowing it to capture radar images that cover 250 km in width. Although there have been other missions that have used a wide swath mode, Sentinel-1 is the first satellite that uses the Terrain Observation by Progressive Scan (TOPS) mode (*De Zan and Guarnieri*, 2006). The TOPS mode is unique in that it allows the sensing of multiple strips in range direction, while ensuring that all points within the scene are illuminated by the same amount of radar pulses (*De Zan and Guarnieri*, 2006). TOPS achieves this by sweeping the beam in the flight (azimuth) direction, before switching to the next swath. It is this sweeping action that ensures constant pulse illumination.

The sweeping of the beam in azimuth direction divides the radar image into so-called “bursts”, while the switching between the strips divides the image in swaths. The left side of Fig. 1.3 shows a schematic overview of the satellite viewing geometry in TOPS-mode, including the division of the scene in bursts and swaths. The switching of the beam across subswaths widens the area covered by the radar scene, at the cost of azimuth resolution (*De Zan and Guarnieri*, 2006). The sweeping of the beam in azimuth direction creates a variation in central Doppler frequency across the burst (see right side of Fig. 1.3). In the overlap between subsequent bursts in the same subswath, this creates a large difference between the Doppler frequencies of the signal received. This difference in Doppler frequency is sensitive to movement in azimuth direction, similar to multi-aperture interferometry described in Section 1.1.4. A misregistration between the master and slave image in azimuth direction is equivalent to a constant azimuth movement over the entire scene. Due to the difference in Doppler frequencies in the overlap region, any misregistration would create a phase difference in the interferogram at the burst edge, leading to a discontinuity in the interferogram. This means that by using TOPS-mode, the coregistration accuracy, in azimuth direction, has to be far better than would be the case for other acquisition modes, by up to three orders of magnitude.

Fortunately, the cause of the problem also provides the answer. The difference in Doppler frequencies create a gap in Doppler frequencies, providing exactly what is required to estimate azimuth offsets using spectral diversity. Using the spectral diversity method yields the accuracy in azimuth direction required to make continuous, smooth interferograms (*Prats-Iraola et al.*, 2012) in the absence of deformation or ionospheric signals. Furthermore, this technique can also be used to detect actual deformation in azimuth direction, with greater precision than previously possible due to the large bandwidth gap.

1.2 Volcano source modelling

Geodetic measurements by themselves can be useful to detect volcanic activity. However, to interpret these measurements and better understand the processes occurring beneath the Earth surface, modeling is required. Analytical models exist that describe different source geometries, for which parameters like depth, volume or pressure increase and spatial dimensions can be varied, and predict the resulting surface deformation in three dimensions. A distinction must be made between two types of models. The first type are kinematic models, which relate a deformation at a source to displacement at points away from the source. The second type of models are mechanical models, which relate forces applied at the source to displacements at points away from it. The distinction might seem subtle, but they are important in terms of the type of constraint they place on the model. Kinematic models are in principle free to deform in random ways. Mechanical models have stress constraints placed on them that drive the deformation, making the models physical by default. Another distinction between types of models are between analytical solutions and approximation methods. The first type provides exact solutions, but are linked to specific, simplified geometries. The second type are more flexible in terms of geometry and complexity, but do not provide an exact solution.

In this section I will give a brief overview of different types of models relevant for this thesis. More details on volcano source modelling can be found in e.g. *Segall* (2009). I will start by introducing three commonly used analytical models. In the final part of this section I will introduce an approximation method that can find solutions for arbitrary geometries, the Boundary Element Method (BEM).

1.2.1 Mogi model

One of the most well-known analytical models in volcano deformation is commonly referred to as the Mogi model (*Mogi*, 1958), although the same result was obtained by several other studies (*Sezawa*, 1931, *Anderson*, 1936, *Yamakawa*, 1955). The Mogi model is a point pressure source, and is used to approximate spherical magma chambers. The model geometry is defined in a cylindrical reference frame. The deformations at the surface in radial and vertical directions can be calculated using the following simple relations:

$$u_z = \frac{(1-\nu)pa^3}{\mu}\frac{d}{(\rho^2+d^2)^{3/2}} \tag{1.3}$$

$$u_\rho = \frac{(1-\nu)pa^3}{\mu}\frac{\rho}{(\rho^2+d^2)^{3/2}} \tag{1.4}$$

where u_z and u_ρ represent displacement in vertical and radial directions, respectively, ν represents the Poisson's ratio, μ the shear modulus, p is the internal pressure change, a is the radius of the spherical source, d is the source depth and ρ is the distance projected on the surface between the source and the computation point. In the above relations, the displacements at the surface depend on the pressure change, making the Mogi model a mechanical model. However, the displacements also depend on the source radius, and the two parameters are not independent, i.e. a high pressure change in a small radius source will have the same effect as a small pressure change in a large radius source. In fact, if we substitute the relationship $\Delta V = \pi pa^3/\mu$ in the above relations, we obtain a Mogi model depending on the volume change of the source:

$$u_z = \frac{(1-\nu)\Delta V}{\pi}\frac{d}{(\rho^2+d^2)^{3/2}} \tag{1.5}$$

$$u_\rho = \frac{(1-\nu)\Delta V}{\pi}\frac{\rho}{(\rho^2+d^2)^{3/2}} \tag{1.6}$$

where ΔV gives the volume change within the source. In this representation, the Mogi model is a kinematic model, which is the way in which the Mogi model is usually applied in practise. The Mogi model assumes an isotropic elastic halfspace, infinitesimal strain and that the depth of the source is many times greater than the radius of the source (*Mogi*, 1958). Figure 1.4 gives a typical model prediction for the Mogi model. The simple equations of the Mogi model means that it is fast to compute a realisation,

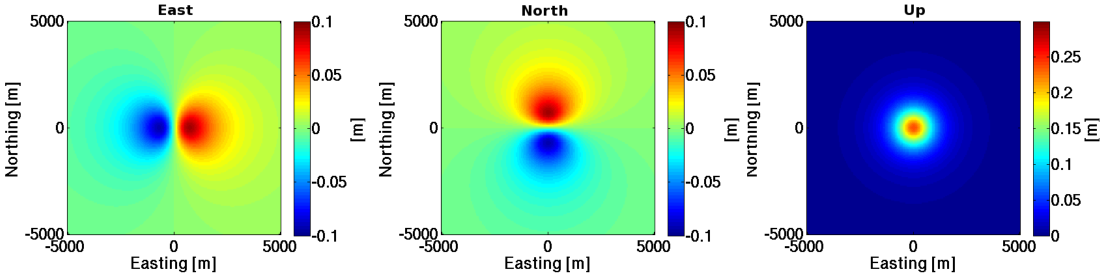

Figure 1.4: Deformation predicted by a Mogi source model in east, north and up direction. The source is located at a depth of 1 km, and the volume increase was set to $1 \cdot 10^6$ m^3.

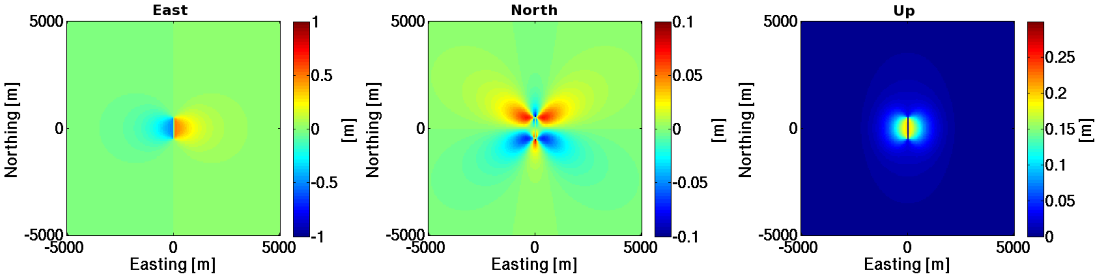

Figure 1.5: Deformation predicted by an Okada model in east, north and up direction for a vertical dike. The top of the dike is located at a depth of 1 km, and has a length and width of 1 km. The opening is set to 1 m.

making it often the first model to be tried when circular deformation patterns are observed.

1.2.2 Dike/Sill

An analytical method to model rectangular faults, dikes or sills was described by *Okada* (1985, 1992). The model assumes an elastic halfspace and infinitesimal strain. The Okada model can compute displacements, strains and tilts resulting from any combination of strike-slip, dip-slip and tensile faulting on rectangular dislocations. The model equations are too extensive to list here, but are easy to implement, and computationally cheap. The Okada model is a kinematic model, i.e. the amount of displacement on the dislocation (slip or opening) is specified in the forward model, not the stresses involved. By summing up the contributions of many Okada dislocations, arbitrary geometries can be modelled, making the model applicable over a wide range of applications. Figure 1.5 shows an Okada model prediction for a vertical dike and Figure 1.6 for a horizontal sill.

1.2.3 Penny-shaped crack

Another widely used model describes a thin circular disk in an elastic half-space (*Fialko et al.*, 2001), which is usually referred to as the penny-shaped crack model. This geometry an be used to represent an intruded sill, which can be a more realistic repre-

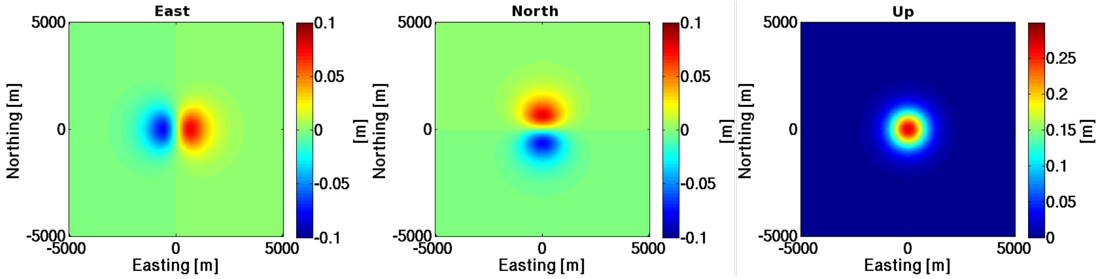

Figure 1.6: Deformation predicted by an Okada model in east, north and up direction for a horizontal sill. The sill is located at a depth of 1 km, and has a length and width of 1 km. The opening is set to 0.8 m.

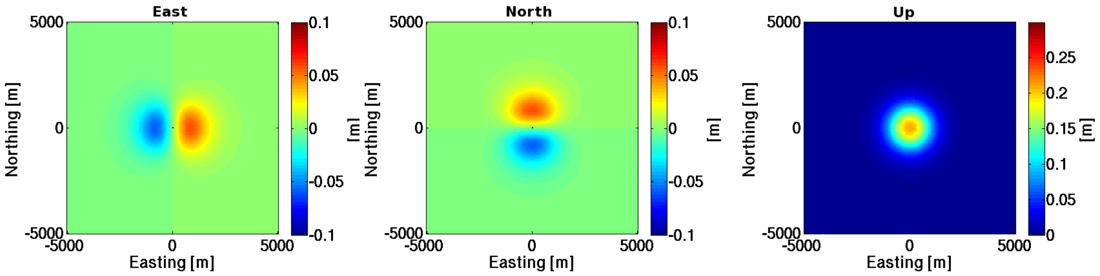

Figure 1.7: Deformation predicted by an penny shaped crack model in east, north and up direction. The sill is located at a depth of 1 km, and has a radius of 1 km. The overpressure is set to 10 MPa.

sentation of the source shape than the Mogi model described in Section 1.2.1. Although the Okada model (see Section 1.2.2) can also be used to model a (rectangular-shaped) sill intrusion, the main advantage of the penny-shaped crack model is that it is a mechanical model. The model yields surface displacements due to a crack with arbitrary radius, hydrostatic overpressure and location. The penny shaped crack model uses numerical approximations to evaluate integrals, making it much slower than the previous two analytical models. Figure 1.7 shows a typical result for the penny-shaped crack model.

1.2.4 Boundary Element Modelling

The analytical models described in the previous three sections can be very useful in quantifying subsurface magma movements from deformation measurements. However, the Mogi and penny-shaped crack models are tied to very specific geometries, making them inflexible. The Okada model can be used to model a wide range of geometries by summing up the contributions of many dislocation patches, but is a kinematic model. The BEM approach can take the flexible Okada model, and turn it into a mechanical model (*Cayol and Cornet*, 1997, *Segall*, 2009). The method requires the source geometry, which can have any arbitrary shape, to be divided into an arbitrary number, k, patches. If we assume the Earth to be an elastic medium, the contributions of the traction on each patch sum up linearly, in other words:

$$\mathbf{T} = \mathbf{G}\mathbf{D}. \tag{1.7}$$

T is the 3k by 1 vector of tractions on each patch, in the three principle directions:

$$\mathbf{T} = \begin{bmatrix} T_{s,1} \\ \vdots \\ T_{s,k} \\ T_{d,1} \\ \vdots \\ T_{d,k} \\ T_{n,1} \\ \vdots \\ T_{n,k} \end{bmatrix}, \tag{1.8}$$

with T_s representing the traction in strike-slip direction, T_d in dip-slip direction and T_n in normal direction. **D** is the vector of displacements on each patch, in the three principle directions and **G** is the mapping function. The forward problem, calculating the tractions from given displacements, is simple to calculate using the Okada model described in Section 1.2.2. The mapping matrix **G** is simply a $3k$ by $3k$ matrix containing the stress response at all patches for unit displacement at each patch, in each principle direction in turn:

$$\mathbf{G} = \begin{bmatrix} T^{u,s,1}_{s,1} & \dots & T^{u,s,k}_{s,1} & T^{u,d,1}_{s,1} & \dots & T^{u,d,k}_{s,1} & T^{u,n,1}_{s,1} & \dots & T^{u,n,k}_{s,1} \\ \vdots & \ddots & \vdots & \vdots & \ddots & \vdots & \vdots & \ddots & \vdots \\ T^{u,s,1}_{s,k} & \dots & T^{u,s,k}_{s,k} & T^{u,d,1}_{s,k} & \dots & T^{u,d,k}_{s,k} & T^{u,n,1}_{s,k} & \dots & T^{u,n,k}_{s,k} \\ T^{u,s,1}_{d,1} & \dots & T^{u,s,k}_{d,1} & T^{u,d,1}_{d,1} & \dots & T^{u,d,k}_{d,1} & T^{u,n,1}_{d,1} & \dots & T^{u,n,k}_{d,1} \\ \vdots & \ddots & \vdots & \vdots & \ddots & \vdots & \vdots & \ddots & \vdots \\ T^{u,s,1}_{d,k} & \dots & T^{u,s,k}_{d,k} & T^{u,d,1}_{d,k} & \dots & T^{u,d,k}_{d,k} & T^{u,n,1}_{d,k} & \dots & T^{u,n,k}_{d,k} \\ T^{u,s,1}_{n,1} & \dots & T^{u,s,k}_{n,1} & T^{u,d,1}_{n,1} & \dots & T^{u,d,k}_{n,1} & T^{u,n,1}_{n,1} & \dots & T^{u,n,k}_{n,1} \\ \vdots & \ddots & \vdots & \vdots & \ddots & \vdots & \vdots & \ddots & \vdots \\ T^{u,s,1}_{n,k} & \dots & T^{u,s,k}_{n,k} & T^{u,d,1}_{n,1} & \ddots & T^{u,d,k}_{n,k} & T^{u,n,1}_{n,1} & \dots & T^{u,n,k}_{n,1} \end{bmatrix} \tag{1.9}$$

where the superscript indicates the unit displacement u of patch 1 to k in slip, dip and normal direction, and the subscript indicates the response to these unit displacements in slip, dip and normal direction at patch 1 to k. In words, for the first column of **G**, the first k entries would represent the traction in strike-slip direction at patch 1 to k for unit displacement in strike-slip direction of the first patch. The second k entries would represent the traction in dip-slip direction at patch 1 to k for unit displacement in strike-slip direction of the first patch. The final k entries would represent the traction in normal direction at patch 1 to k for unit displacement in strike-slip direction of the first patch. Columns k+1 and 2k+1 follow the same pattern, but for unit displacement in dip-slip and normal direction, respectively.

With the mapping function defined, it is easy to solve for the displacements on each patch, given a traction on every patch:

$$\mathbf{D} = \mathbf{G^{-1}T}, \tag{1.10}$$

Arbitrary shaped source geometries could be inverted for by using Okada Green's functions directly. However, as discussed above, the Okada model is a kinematic model. Inverting for displacements directly often results in very rough solutions for the displacements and unrealistic stress on boundaries. By modelling stresses, BEM inherently yields a smooth, physically realistic (in terms of spatial distribution of displacements) displacement pattern (see Figure 1.8 for an example). The fact that it is a mechanical model allows one to study the cause of displacements, not just the effect. Furthermore, other phenomena that influence the stress field can be taken into account as well, making BEM a versatile and powerful tool in volcano modelling.

1.3 Volcanism in Iceland

Iceland is located on the mid-Atlantic ridge (MAR), making it one of the few places in the world where on-land spreading of tectonic plates can be seen (Figure 1.9). The North American and the Eurasian plate move apart at approximately 1.9 cm/yr, all of which is accommodated within Iceland (*Geirsson et al.*, 2006).

Due to the presence of the MAR and a hotspot beneath Iceland, approximately thirty active volcanoes can be found in the country (*Sigmundsson*, 2006). Most of these volcanoes can be found in the volcanic rift zones, see Figure 1.9. The MAR enters Iceland in the south-west tip of the country. Here it moves east-north-east in what is known as the Reykjanes peninsula oblique rift. At Hengill volcano, the spreading zone turns into a more north-south orientation, until it reaches Langjökull icecap. This section is known as the western volcanic zone (WVZ). Within Iceland, the spreading zone jumps approximately 100 km to the east. This jump is accommodated by the South Iceland Seimic Zone (SISZ), a left lateral transform fault, which runs approximately from Hengill volcano to Torfajökull volcano. The SISZ has had recent earthquakes of 6.5 M_w in 2000 and 6.3 M_w in 2008 (*Decriem et al.*, 2010). At Torfajökull volcano, the Eastern Volcanic Zone (EVZ) commences, which ends underneath Vatnajökull icecap, the largest icecap in Europe with a mean diameter of approximately 100 km (Fig. 1.9). North of Vatnajökull, the spreading zone continues into the Northern Volcanic Zone, which terminates into the Tjörnes fracture zone at the north coast, at which point the

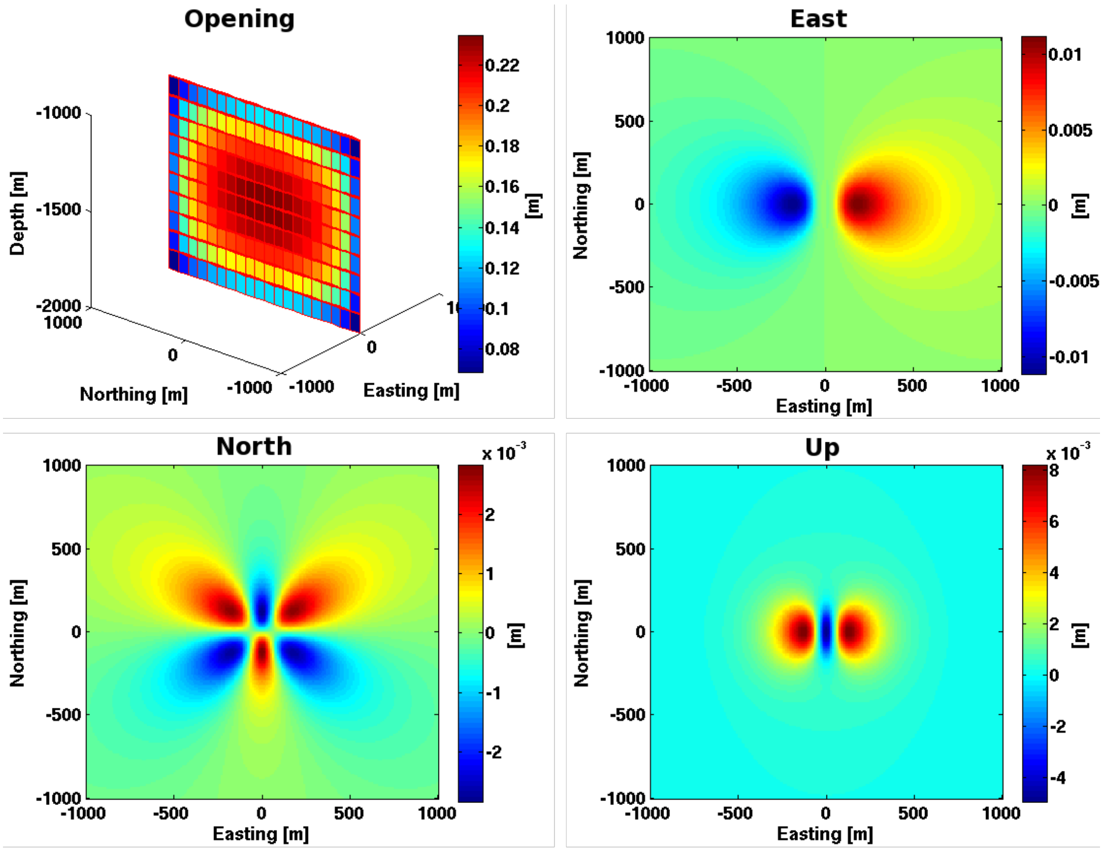

Figure 1.8: Example of a BEM result representing a vertical dike, showing the opening of each of the twenty patches, and predicted deformation in east, north and up direction. The dike has a length of two kilometers, a width of one kilometer. The top of the dike is located at a depth of one kilometer, and the overpressure in the dike is set to 10 MPa.

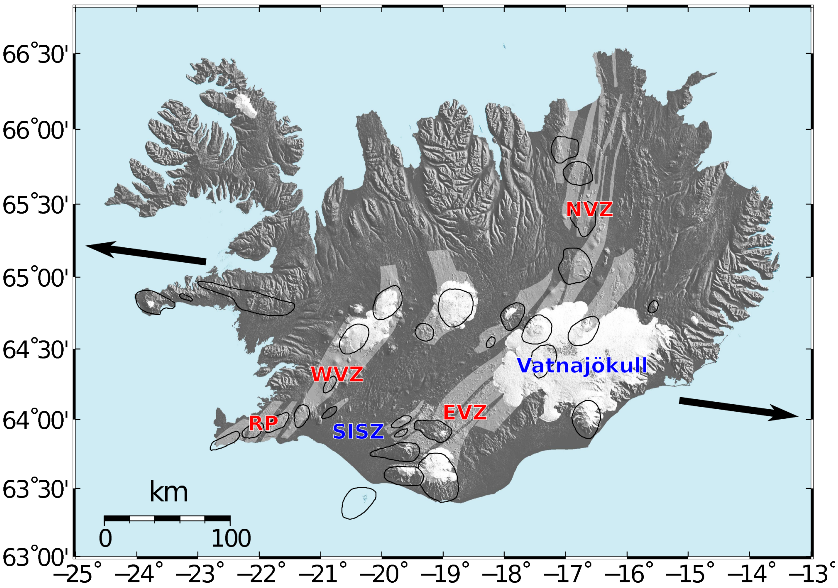

Figure 1.9: Map showing Iceland and main volcanic regions in red. The MAR enters Iceland at the tip of the Reykjanes peninsula (RP). Further west, the oblique RP volcanic zone turns into the western volcanic zone (WVZ). The WVZ connects to the eastern volcanic zone (EVZ) through the south Iceland seismic zone (SISZ). Beneath the Vatnajökull icecap, the EVZ turns into the northern volcanic zone (NVZ). The outlines show the central volcanoes of volcanic systems in Iceland, and the light grey areas show the fissure swarms associated with volcanic systems. The white regions are icecaps, and the background is a shaded relief map based on the ASTER GDEM..

MAR jumps back towards the west.

Three volcanic systems in Iceland feature in this thesis, Katla, Eyjafjallajökull and Bárðarbunga. In the following sections I will give a brief overview of these three systems.

1.3.1 Katla

Katla volcano is located in south Iceland, see Figure 1.10, close to where the SISZ meets the EVZ. It has erupted at least 20 times since the ninth century (*Larsen*, 2000). An icecap, Mýrdalsjökull, covers the higher part of the volcano, making eruptions from Katla's caldera explosive and often accompanied by jökulhlaups, glacier outburst floods. The last confirmed eruption of Katla occurred in 1918, and resulted in a vast jökulhlaup from one of the outlet glaciers on the east flank of the volcano (*Tómasson*, 1996). Since then, three more jökulhlaups (in 1955 (*Rist*, 1967), 1999 (*Sigurdsson et al.*, 2000) and 2011) drained from the caldera, which could have been due to eruptions that did not break the ice, but may also have been caused by inflow of geothermal water. Continuous GNSS measurements started after 1999, when three GNSS stations were installed on the south side of Katla. Movements seen at these stations have been interpreted as increased pressure in the magma chamber (*Sturkell et al.*, 2006, 2009), but the poor spatial density and small magnitude of these measurements have since casted doubt on

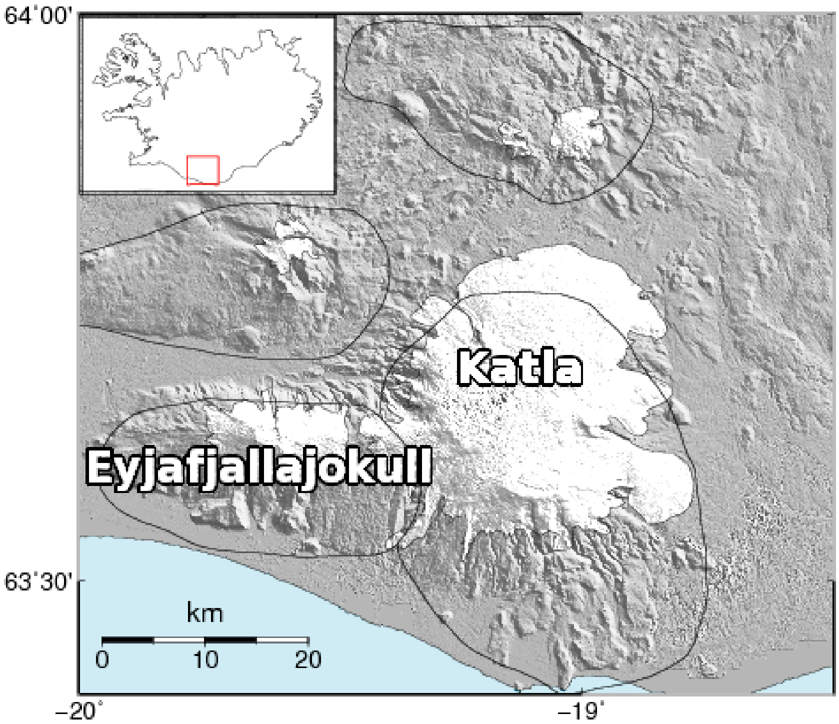

Figure 1.10: Map showing the Katla and Eyjafjallajökull volcanic systems. Two further volcanic systems are visible to the north, Tindfjallajökull and Torfajökull.

this interpretation (see Chapter 3).

1.3.2 Eyjafjallajökull

Eyjafjallajökull volcano is most well known for causing a long disruption of air traffic in much of Europe during its 2010 eruption (*Sigmundsson et al.*, 2010a). It is located in the south of Iceland, directly neighbouring Katla volcano (Figure 1.10). Before the 2010 eruption, Eyjafjallajökull had only erupted three times since settlement of Iceland in the ninth century. All three of these eruptions were followed shortly after by an eruption of Katla. Around 920 and in 1612, both volcanoes erupted (*Óskarsson*, 2009, *Larsen et al.*, 1999, *Larsen*, 2000), and Katla erupted in 1823, shortly after the 1821-23 Eyjafjallaökull eruption sequence (*Larsen*, 2000, *Sturkell et al.*, 2009). No eruption of Katla has followed its latest eruption in 2010. In 1994 and 1999, deformations were measured on the south flank of Eyjafjallajökull (*Pedersen and Sigmundsson*, 2004, *Hooper et al.*, 2009). Both these signals were interpreted as pressure increase in sill shaped sources, both at a depth of approximately 5.6 km, although in different locations. The 2010 eruption at Eyjafjallajökull consisted of two events. On the 20th of March, 2010, an effusive fissure eruption started on the flank between Eyjafjallajökull and Katla. This event lasted until the 12th of April. After a two day pause, an explosive caldera eruption commenced on the 14th of April, which continued erupting lava and ash continuously until the 22nd of May, 2010 (*Sigmundsson et al.*, 2010a). The 2010 eruption was the first eruption in

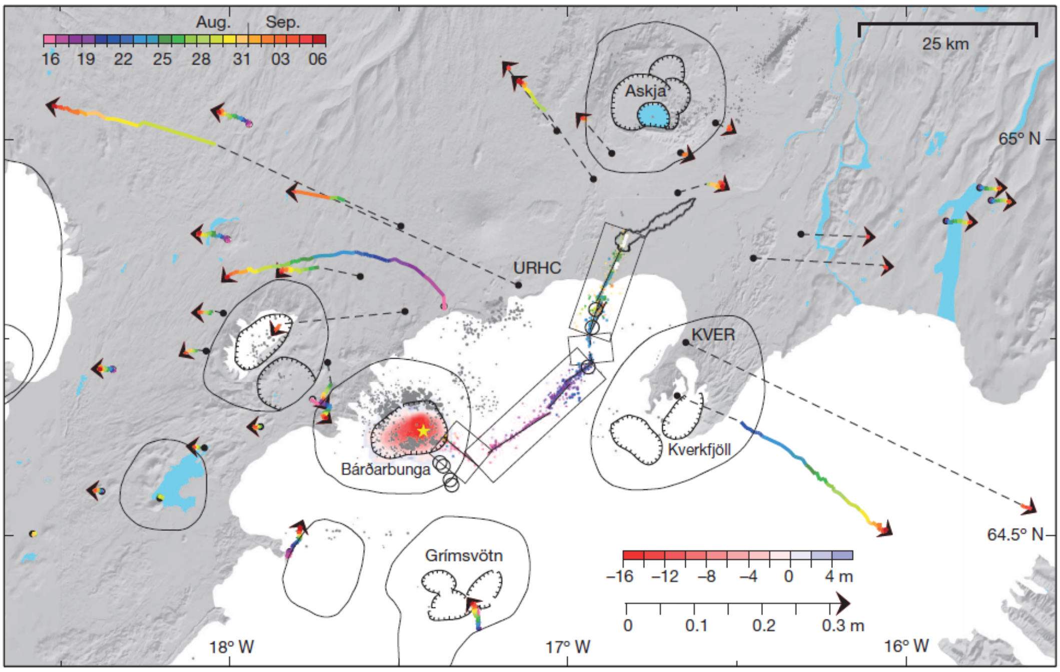

Figure 1.11: Map showing the Bardabunga volcanic system and surrounding area, showing the central volcanoes (oval outlines) and calderas (hatched lines) in the area. Overlain on the map are the GPS displacements and seismicity during the early stages of the 2014/2015 Holuhraun eruption. The subsidence measured in the caldera is also shown. Figure reproduces with permission from *Sigmundsson* et al. (2015)

Iceland to be covered by a dense timeseries of interferograms, providing great insight into the evolution of the eruption (see Chapter 2).

1.3.3 Bárðarbunga

Bárðarbunga volcano is a subglacial volcano which lies beneath the north-west part of the Vatnajökull icecap (Figure 1.11). Prior to the 2014 eruption, it had 23 confirmed eruptions since settlement of the island (*Thordarson and Larsen*, 2007), three of which produced over 1 km^3 of lava. On the 16th of August, 2014, an intense seismic swarm beneath the Bárðarbunga caldera marked the onset of the 2014 eruptive event. In the course of 13 days, seismicity migrated away from caldera, first radially out towards the east-southeast, before turning towards the north-northwest. GNSS stations showed rapid movements up and away from the seismicity, indicating significant intrusion of magma into a dike. After travelling some 47 km, the magma finally erupted at the northern tip of the dike in a small event, starting on the 29th of August, and lasting only 4 hours (*Sigmundsson* et al., 2015). On the 30th of August, the same fissure saw a second eruption, which lasted until February 2015. 1.5 km^3 of lava was erupted during the event, covering an area of 85 km^2. At the same time as the fissure eruption, the caldera underwent a collapse event as well, collapsing more than 80 m in total.

1.4 Aims and objectives

As discussed in Section 1.1.5, the successful operation of Sentinel-1A means that we have entered an exciting era of opportunity for radar interferometry and its applications. In recent years, processing techniques have been focused on complex timeseries analysis of InSAR data. The regular acquisitions of Sentinel-1, coupled with the data being freely available, means that we can start to process all data in a systematic way over selected volcanic regions, or even globally. Time series analysis techniques are generally slow and require analysis of the entire dataset as a whole, making them too cumbersome for systematic processing of newly acquired data. We therefore need to rethink our processing strategies. The result of this will be unprecedented monitoring of Earth surface movements.

The increase in data means that we will be able to measure ever smaller signals. It will become even more vital to accurately pinpoint the source of these deformations, to determine whether or not they are magmatic in nature. Furthermore, we need to be able to model any signals we detect in a timely fashion, for scientific reasons, but more importantly for early response on the ground.

The aim of my thesis is to develop a processing methodology that allows InSAR data to be processed in near-real time to enhance our volcano monitoring capabilities, and to further our modelling capabilities to take full advantage of this data stream. To achieve this, I have defined the following objectives:

- Develop a method to rapidly and accurately estimate coherence for newly processed interferograms, to obtain high-quality deformation measurements over volcanic areas in near-real time.
- Explore different sources of deformation around volcanoes that might mimic magmatic movements, and find ways to correct for them
- Utilize InSAR to constrain advanced models to make inferences about stress changes
- Explore how the unique characteristics of the Sentinel satellite system can help us study and monitor volcanoes and other surface deforming processes better.

1.5 Thesis Roadmap

The remainder of this thesis is organised as follows:

- Chapter 2 describes the RapidSAR method, a method to process InSAR data for volcano monitoring and other near-real time applications.
- Chapter 3 describes a combined InSAR and GNSS study covering the Katla volcano between 2001 to 2010.

- Chapter 4 describes a study that uses InSAR and GNSS measurement to constrain a BEM model of the 2014 Holuhraun eruption of the Bárðarbunga volcano.
- Chapter 5 describes a study into the potential of Sentinel-1 and RapidSAR for deformation applications.
- Chapter 6 links the findings of this thesis to the objectives defined above, and provides an outlook for the future.

References

Anderson, E. (1936), The dynamics of the formation of cone-sheets, ring-dykes, and caldron subsidence, *Proceedings of the Royal Society of Edinburgh*, *56*, 128–157. 1.2.1

Bamler, R., and P. Hartl (1998), Synthetic Aperture Radar interferometry, *Inverse Problems*, *14*, 1–54. 1.1, 1.1.1

Bechor, N., and H. Zebker (2006), Measuring two-dimentional movements using a single InSAR pair, *Geophys Res Lett*, *33*, L16,311, doi:10.1029/2006GL026883. 1.1.4

Berardino, P., G. Fornaro, R. Lanari, and E. Sansosti (2002), A new algorithm for surface deformation monitoring based on small baseline differential SAR interferograms, *IEEE Transactions on Geoscience and Remote Sensing*, *40*(11), 2375, doi:10.1109/TGRS.2002.803792. 1.1.3

Brown, L. (1992), A survey of image registration techniques, *ACM Computing Surveys*, *24*, 325–376. 1.1.1

Cayol, V., and F. Cornet (1997), 3D Mixed Boundary Elements for elastostatic deformation field analysis, *Int. J. Rock Mech. Min. Sci.*, *34*(2), 275–287. 1.2.4

Chen, C., and H. Zebker (2001), Two-dimensional phase unwrapping with use of statistical models for cost functions in nonlinear optimization, *J. Opt. Soc. Am. A*, *18*(2), 338–351, doi:10.1364/JOSAA.18.000338. 1.1.1

De Zan, F., and A. Guarnieri (2006), TOPSAR: Terrain observation by progressive scans, *Ieee Transactions On Geoscience And Remote Sensing*, *44*(9), 2352–2360, doi:10.1109/TGRS.2006.873853. 1.1.5, 1.1.5

Decriem, J., T. Árnadóttir, A. Hooper, H. Geirsson, F. Sigmundsson, M. Keiding, B. G. Ófeigsson, S. Hreinsdóttir, P. Einarsson, P. LaFemina, and R. A. Bennett (2010), The 2008 May 29 earthquake doublet in SW Iceland, *Geophysical Journal International*, doi:10.1111/j.1365-246X.2010.04565.x. 1.3

Elliott, J., R. Jolivet, P. González, J.-P. Avouac, J. Hollingsworth, M. Searle, and V. Stevens (2016), Himalayan megathrust geometry and relation to topography revealed by the Gorkha earthquake, *Nature Geosc*, *9*, 174–180, doi:10.1038/NGEO2623. 1.1

Ferretti, A., C. Prati, and F. Rocca (2001), Permanent Scatterers in SAR Interferometry, *IEEE Transactions on geoscience and remote sensing*, *39*(1), 8–20, doi:0196{--}2892/01. 1.1.3

Ferretti, A., A. Fumagalli, F. Novali, C. Prati, F. Rocca, and A. Rucci (2011), A New Algorithm for Processing Interferometric Data-Stacks: SqueeSAR, *IEEE Transactions on Geoscience and Remote Sensing*, *49*(9), 3460, doi:10.1109/TGRS.2011.2124465. 1.1.3

Fialko, Y., Y. Khazan, and M. Simons (2001), Deformation due to a pressurized horizontal circular crack in an elastic half-space, with applications to volcano geodesy, *Geophys. J. Int.*, *146*, 181–190. 1.2.3

Fornaro, G., S. Verde, and D. Reale (2015), CAESAR: An approach based on covariance matrix decompositon to improve multibaseline-multitemporal interferometric SAR processing, *IEEE Trans. Geosc. Rem. Sens.*, *53*(4), 2050–2065, doi:10.1109/TGRS.2014.2352853. 1.1.3

Geirsson, H., T. Arnadottir, C. Volksen, W. Jiang, E. Sturkell, T. Villemin, P. Einarsson, F. Sigmundsson, and R. Stefansson (2006), Current plate movements across the mid-atlantic ridge determined from 5 years of continuous gps measurements in iceland, *J. Geophys. Res. Solid Earth*, *111*(B9), B09,407, doi:10.1029/2005JB003717. 1.3

González, P., M. Bagnardi, A. Hooper, Y. Larsen, P. Marinkovic, S. Samsonov, and T. Wright (2015), The 2014-2015 eruption of Fogo volcano: Geodetic modeling of Sentinel-1 TOPS interferometry, *Geophys Res Lett*, *42*, 9239–9246, doi:10.1002/2015GL066003. 1.1

Grandin, R., E. Klein, M. Métois, and C. Vigny (2016), Three-dimensional displacement field of the 2015 M_w 8.3 Illapel earthquake (Chile) from across- and along-track Sentinel-1 TOPS interferometry, *Geophys Res Lett*, *43*, doi:10.1002/2016GL067954. 1.3

Hanssen, R. (2001), Radar interferometry: Data interpretation and error analysis, Ph.D. thesis, Delft University of Technology. 1.1, 1.1.1

Hooper, A. (2008), A multi-temporal InSAR method incorporating both persistent scatterer and small baseline approaches, *Geophys Res Lett*, *35*(16), doi:10.1029/2008GL034654. 1.1.3

Hooper, A., P. Segall, and H. Zebker (2007), Persistent scatterer interferometric synthetic aperture radar for crustal deformation analysis, with application to Volcán Alcedo, Galápagos, *Journal of Geophysical Research*, *112*(B7), doi:10.1029/2006JB004763. 1.1.3

Hooper, A., R. Pedersen, and F. Sigmundsson (2009), Constraints on Magma intrusion at Eyjafjallajökull and Katla Volcanoes in iceland, from time series sar interferometry, *The VOLUME Project, Volcanoes: Understanding subsurface mass movement*, pp. 13–24. 1.3.2

Just, D., and R. Bamler (1994), Phase statistics of interferograms with applications to synthetic aperture radar, *Appl. Opt.*, *33*(20), 4361–4368. 1.1.2

Larsen, G. (2000), Holocene eruptions within the Katla volcanic system, south Iceland: Characteristics and environmental impact, *Jökull*, *49*, 1–28. 1.3.1, 1.3.2

Larsen, G., A. Dugmore, and A. Newton (1999), Geochemistry of historical-age silicic tephras in Iceland, *The Holoscene*, *9*(4), 463–471, doi:10.1191/095968399669624108. 1.3.2

Michel, R., J.-P. Avouac, and J. Taboury (1999), Measuringe ground displacements from SAR amplitude images: application to the Landers earthquake, *Geophys Res Lett*, *26*(7), 875–878. 1.1.4

Mogi, K. (1958), Relations between eruptions of various volcanoes and the deformations of the ground surfaces around them., *Bulletin of the Earthquake Research*, *36*, 99–134. 1.2.1, 1.2.1

Okada, Y. (1985), Surface deformation due to shear and tensile faults in a half-space, *Bulletin of the Seismological Society of America*, *75*(4), 1135–1154. 1.2.2

Okada, Y. (1992), Internal deformation due to shear and tensile faults in a half-space, *Bull. Seism. Soc. Am.*, *82*(2), 1018–1040. 1.2.2

Óskarsson, B. (2009), The Skerin ridge on Eyjafjallajökull, south Iceland: Morphology and magma-ice interaction in an ice-confined silicic fissure eruption, Master's thesis, Faculty of Earth Sciences, University of Iceland, Reyjavík. 1.3.2

Pedersen, R., and F. Sigmundsson (2004), InSAR based sill model links spatially offset areas of deformation and seismicity for the 1994 unrest episode at Eyjafjallajökull volcano, Iceland, *Geophys. Res. Lett.*, *31*, doi:10.1029/2004GL020368. 1.3.2

Prats-Iraola, P., R. Scheiber, L. Marotti, S. Wollstadt, and A. Reigber (2012), TOPS interferometry with TerraSAR-X, *IEEE Trans Geosc Rem Sens*, *50*(8), 3179–3188, doi:10.1109/TGRS.2011.2178247. 1.1.5

Rist, S. (1967), Jökulhlaups from the ice cover of Mýrdalsjökull on June 25, 1955 and January 20, 1956., *Jökull*, *17*, 243–248. 1.3.1

Scheiber, R., and A. Moreira (2000), Coregistration of interferometric SAR images using Spectral Diversity, *IEEE Trans. Geosci. Remote Sens.*, *38*(5), 2179 – 2191, doi:10.1109/36.868876. 1.1.4

Schmidt, A., T. Thordarson, L. Oman, A. Robock, and S. Self (2012), Climatic impact of the long-lasting 1783 Laki eruption: Inapplicability of mass-independent sulfur isotopic composition measurements, *J. Geophys. Res. Atmospheres*, *117*, D23,116, doi:10.1029/2012JD018414. 1

Schmidt, D. A., and R. Bürgmann (2003), Time-dependent land uplift and subsidence in the Santa Clara valley, California, from a large interferometric synthetic aperture radar data set, *Journal of Geophysical Research*, *108*(B9), doi:10.1029/2002JB002267. 1.1.3

Segall, P. (2009), *Earthquake and Volcano Deformation*, Princeton University Press, Princeton. 1.2, 1.2.4

Sezawa, K. (1931), The plastico-elastic deformation of a semi-infinite solid body due to an internal force, *Bulletin of Earthquake research Institute University of Tokyo*, *9*, 398–406. 1.2.1

Sigmundsson, F. (2006), *Iceland Geodynamics*, Springer Praxis, doi:10.1007/3-540-37666-6. 1.3

Sigmundsson, F., S. Hreinsdóttir, A. Hooper, T. Árnadóttir, R. Pedersen, M. Roberts, N. Óskarsson, A. Auriac, J. Decriem, P. Einarsson, H. Geirsson, M. Hensch, B. Ófeigsson, E. Sturkell, H. Sveinbjörnsson, and K. Feigl (2010a), Intrusion triggering of the 2010 Eyjafjallajökull explosive eruption, *Nature*, *468*(7322), 426, doi:10.1038/nature09558. 1, 1.3.2

Sigmundsson, F., V. Pinel, B. Lund, F. Albino, C. Pagli, H. Geirsson, and E. Sturkell (2010b), Climate effects on volcanism: influence on magmatic systems of loading and unloading from ice mass variations, with examples from Iceland, *Philosophical Transactions Of The Royal Society A-Mathematical Physical And Engineering Sciences*, *368*(1919), 2519–2534, doi:10.1098/rsta.2010.0042. 1.1

Sigmundsson *et al.*, F. (2015), Segmented lateral dyke growth in a rifting event at Bárdarbunga volcanic system, Iceland, *Nature*, *517*, 191–195, doi:10.1038/nature14111. 1.1, 1.1, 1.11, 1.3.3

Sigurdsson, O., S. Zóphóníasson, and E. Ísleifsson (2000), Jökulhlaupúr Sólheimajökli 18. júlí 1999 (The jökulhlaup from Sólheimajökull July 18, 1999, in Icelandic with English summary), *Jökull*, *49*, 75–80. 1.3.1

Sturkell, E., P. Einarsson, F. Sigmundsson, H. Geirsson, H. Ólafsson, R. Pedersen, E. De Zeeuw-Van Dalfsen, A. Linde, S. Sacks, and R. Stefansson (2006), Volcano geodesy and magma dynamics in Iceland, *J Volcanol Geoth Res*, *150*(1-3), 14, doi:10.1016/j.jvolgeores.2005.07.010. 1.3.1

Sturkell, E., P. Einarsson, F. Sigmundsson, A. Hooper, B. Ófeigsson, H. Geirsson, and H. Ólafsson (2009), Katla and Eyjafjallajökull Volcanoes, *Developments in Quaternary Science*, *13*, 5–21. 1.3.1, 1.3.2

Thordarson, T., and G. Larsen (2007), Volcanism in iceland in historical time: Volcano types, eruption styles and eruptive history, *J GEODYN*, *41* (1), 118–152, doi:10.1016/j.jog.2006.09.005. 1.3.3

Tómasson, H. (1996), The jökulhlaup from Katla in 1918, *Annals of Glaciology*, *22*, 249–254. 1.3.1

Touzi, R., A. Lopes, J. Bruniquel, and P. Vachon (1999), Coherence estimation for SAR imagery, *IEEE Trans Geosc Rem Sens*, *37* (1), 135–149. 1.1.2

Wright, T., E. Fielding, and B. Parsons (2001), Triggered slip: observations of the 17 August Izmit (Turkey) earthquake using radar interferometry, *Geophys. Res. Lett.*, *28* (6), 1079–1082. 1.1

Wright, T. J., B. E. Parsons, and Z. Lu (2004), Towards mapping surface deformation in three dimensions using InSAR, *Geophys. Res. Let.*, *31* (L01607), doi:10.1029/2003GL018827. 1.1.1, 1.1.4

Yamakawa, N. (1955), On the strain produced in a semi-infinite elastic solid by an interior source of stress, *Zisin (Journal of the Seismological Society of Japan)*, *8*, 84–98. 1.2.1

Zebker, H., and J. Villasenor (1992), Decorrelation in interferometric radar echoes, *IEEE Trans. Geosci. Remote Sens.*, *30* (5), 950–959. 1.1.1

Chapter 2

InSAR processing for volcano monitoring and other near-real time applications

Karsten Spaans[1] and Andrew Hooper[1]

[1] *COMET, School of Earth and Environment, University of Leeds, United Kingdom*

Abstract

Radar interferometry (InSAR) is routinely used to measure surface deformation prior to, during, and after volcanic events, although not in a monitoring capacity. The improved data availability of some current satellite missions presents us with the opportunity to do just that. We present here a fast and flexible algorithm to estimate coherence and select points on an interferogram-by-interferogram basis, which overcomes limitations of the conventional boxcar ensemble method in areas of marginal coherence. Time series methods, which offer an alternative way to select coherent points, are typically slow and do not allow for insertion of new data without reprocessing the entire dataset. Our new algorithm calculates the coherence for each point based on an ensemble of points with similar amplitude behaviour throughout the dataset. The points that behave similarly are selected prior to new images being acquired, on the assumption that the behaviour of these nearby points does not change rapidly through time. The resulting coherence estimate is superior in resolution and noise level to the boxcar method. In contrast to most other time series methods, we select a different set of coherent points for each interferogram, avoiding the selection compromise inherent to other time series methods. The relative simplicity of this strategy compared to other time series techniques means we can process new images in about one hour for a typical set up.

2.1 Introduction

InSAR uses radar signal interferometry to obtain high resolution surface deformation measurements with mm to cm level accuracy, covering areas of hundreds to thousands of square kilometers per interferogram (*Bamler and Hartl*, 1998, *Hanssen*, 2001). Since the first demonstrations of the technique using satellites in the 1980s (e.g. *Gabriel et al.* (1989), *Li and Goldstein* (1990)), Interferometric Synthetic Aperture Radar (InSAR) has evolved into one of the main geodetic technique for monitoring surface deformation. Its dense spatial sampling compliments other techniques like GPS and levelling, where the requirement of equipment and manpower in the field limits spatial sampling.

The basic InSAR technique interferes two SAR images to obtain an interferogram, which gives the difference in phase between the two images. Although it contains several nuisance terms, the phase difference largely reflects the surface deformation in the radar line of sight (LOS) during the period between the two acquisition dates. To form the interferograms, the images have to be in the same geometry. This is achieved by coregistering the slave image to the master, and resampling it (*Hanssen*, 2001). Each pixel of the master is then multiplied by the complex conjugate of the corresponding pixel in the slave image to obtain the interferogram. Due to the difference in position of the satellite at the times of acquisition, a phase component is introduced. As this geometric component is a function of the known baseline (the difference in position between the satellites) and the topographic height, a digital elevation model (DEM) can be used to remove this phase component from the interferometric phase (*Bamler and Hartl*, 1998).

One of the main drawbacks of InSAR is that it relies on the scattering properties of the surface remaining consistent. The signal scattered back towards the satellite by every resolution element is the result of the coherent summation of many individual scatterers. If the scattering properties of these individual scatterers changes, or if the viewing geometry between acquisitions changes, the coherent summation changes as well. This introduces noise into the signal, known as decorrelation (*Zebker and Villasenor*, 1992).

Coherence is a measure of the amount of correlation, and has magnitude between 0 (no correlation) and 1 (full correlation). The coherence of each point in a single interferogram can be estimated from the phase and amplitude statistics of an ensemble of surrounding pixels ((*Touzi et al.*, 1999). The standard approach is to use a two-dimensional boxcar to define the ensemble of pixels. The boxcar method has three main drawbacks. First, it suffers from a resolution problem. Points within the ensemble have different scattering characteristics, and those points with high amplitude (e.g. buildings or natural ridges) dominate the coherence estimation. Neighbouring points use nearly the same mix of points within the ensemble, leading to a smearing out of these features. Second, it tends to overestimate the coherence of a large amount of fully decorrelated

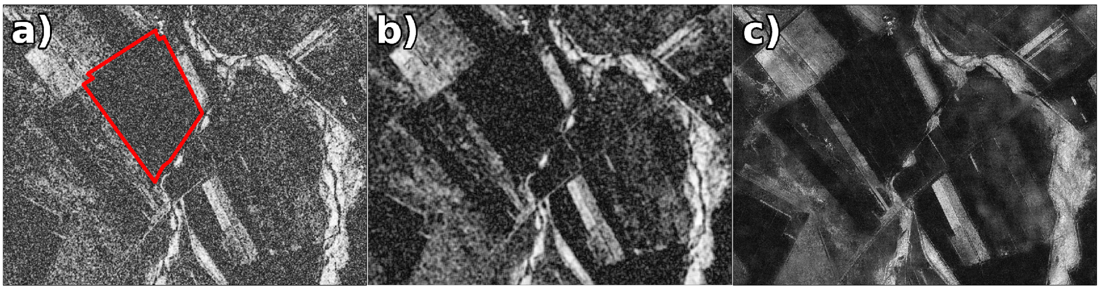

Figure 2.1: Comparison between three different full resolution coherence estimates of the same interferogram (20090618-20090629): a) A 5x5 window boxcar, b) 11x11 window boxcar and c) sibling based (25 to 100 siblings per point, 41x41 search window). The boxcar coherence estimates finds many false high coherence points, such as in the field outlined in red.

points because of the random signal being similar for neighbouring points by chance. As neighbouring points have very similar ensembles, these features also smear out, exacerbating the issue (Fig. 2.1a & b). Third, as the method essentially measures the variability of phase within the window, any non-constant signal biases the coherence estimation, with high phase gradients leading to low coherence

Time series analysis techniques were developed partly as a way to deal with the problem of decorrelation. Two broad categories have been developed: the persistent scatterer (PS) and small baselines (SB) methods. The PS techniques focus on pixels which are dominated by a single strong scatterer, which are less sensitive to decorrelation (*Ferretti et al.*, 2001, *Hooper et al.*, 2007). The SB methods focus on forming interferometric pairs with small perpendicular and temporal (i.e. separation in time of the two images) baselines (*Berardino et al.*, 2002, *Hooper*, 2008). They are therefore better able to extract pixels containing many scatterers, known as distributed scatterers, that might decorrelate in longer baseline combinations. Both types of method select a set of points that are deemed coherent throughout all the interferograms used in the time series. By selecting the same set of points in every interferogram, the time domain can be used to assist in unwrapping the phase (*Hooper*, 2009). Both the PS and SB methods suffer from long processing times when run at full resolution, due to their complex analysis methods. Also, the fact that they select the same set of points in each interferogram leads to an averaging effect. Coherent points in high coherence interferograms may not be selected because the same points are decorrelated in too many of the low coherence interferograms in the dataset. Vice versa, decorrelated points may be selected because of good coherence in the majority of the interferograms (*Hooper et al.*, 2011a). This lowers the overall signal-to-noise ratio in the results significantly, and inevitably leads to a loss of information. This selection compromise was partly addressed by identifying “semi-PS”, “temporary” PS or “partial” PS points (*Basilico et al.*, 2004, *Hooper et al.*, 2011a), with success heavily dependent on the area (*Ferretti et al.*, 2011).

A different type of time series approach known as SqueeSAR (*Ferretti et al.*, 2011) takes advantage of both PS and distributed scatterer pixels to maximize the amount of information extracted from the interferograms. To achieve this, pixels within a neighbourhood that behave in a similar way are identified. In the SqueeSAR method, these pixels are referred to as Statistically Homogeneous Pixels (SHPs). In this text, we will refer to them as siblings, representing their relationship to each other in terms of scattering mechanism. The SqueeSAR method identifies siblings by applying the two-sample Kolmogorov-Smirnov test (*Stephens*, 1970) on the amplitude vectors (through time) of the current pixel and all neighbours (in turn) contained in a window around it, assuming a level of significance. After identifying the siblings for a given pixel, the method is able to estimate the sample covariance matrix (*Ferretti et al.*, 2011). For distributed scatterers, which are identified as having a number of siblings greater than a certain threshold, the covariance matrix is used to invert for the maximum likelihood (ML) phase value of each cluster of siblings in each of the original interferogram. This estimation process also yields a "goodness of fit" measure, akin to a coherence estimate. For a sibling cluster of distributed scatterer pixels, with an estimated coherence above a certain threshold, a single point with the estimated ML phase value replaces the original points, essentially filtering the original interferogram, taking into account different scattering mechanisms. The resulting filtered interferograms are then processed using a conventional PS algorithm, identifying points which stay coherent throughout the timeseries. The ML phase estimation is non-linear, and therefore requires iterative methods, greatly increasing processing time. In rural areas, the method can, however, significantly increase the amount of information extracted. Similar methods have since appeared, like the CAESAR approach (*Fornaro et al.*, 2015), or the NL-InSAR method (*Deledalle et al.*, 2011), which uses non-local ensembles estimated using single interferograms. The idea of SHPs or siblings has been around for much longer, first appearing as part of the sigma filter as a means of despeckling SAR images (*Lee*, 1983). Many approaches have been proposed to identify siblings, for example in *Nicolas et al.* (2001) using a region growing approach, in *Parizzi and Brcic* (2011) using different statistical tests and in *Vasile et al.* (2006) exploiting polarimetry information.

Surface deformations in and around volcanoes are an example where InSAR measurements have proven valuable (*Amelung et al.*, 2000, *Sigmundsson et al.*, 2010a). InSAR typically has a superior spatial measurement density compared to GPS, making it very useful in constraining the source parameters of surface deformation due to magma movements. However, InSAR data has been sparse in time, and to analyse the data often takes days to weeks to complete. Current SAR satellite missions combine a much shorter repeat time with increased data acquisition capabilities, to yield a greatly improved measurement frequency over most areas compared to previous SAR missions. If all potential acquisitions are realised, an average of ~ 2 images a day is now possible. This high measurement frequency potentially allows us to use InSAR as a near-real time monitoring tool, as is the case for ground-based techniques such as GNSS. But to achieve this, a rethink of our processing strategies is required, shifting away from slow time series techniques towards more flexible, faster processing. This is also facilitated by the shorter repeat time and higher data acquisition volume, which yields far superior overall coherence of the interferograms, reducing the need for complex time series techniques.

Here we present a new InSAR processing algorithm, aimed at fast ingestion of new images, while extracting the maximum amount of information. The algorithm, which we refer to as Rapid Time Series InSAR (RapidSAR), uses sibling information not for pre-processing prior to time series processing like the SqueeSAR method, but to quickly estimate the coherence for each pixel in newly formed interferograms. This avoids many of the problems of boxcar coherence estimation, while retaining much of its speed and flexibility. Our method yields an individual coherence estimate for each interferogram, in contrast to most other timeseries methods. This allows us to avoid the selection compromise of PS and SB methods, and maximise the amount of information extracted. We demonstrate the effectiveness of RapidSAR on datasets covering the Eyjafjallajökull and Bárðarbunga volcanoes, Iceland.

2.2 Processing strategy

To allow the fast processing of new images required for effective volcano monitoring, we have split our processing strategy in two. We start from a set of full resolution interferograms co-registered to a common master, and use this initial dataset to identify for each pixel a set of siblings. This information is stored for use when a new image comes in. A more detailed overview of how siblings are selected can be found in Section 2.2.1.

The second part of the processing strategy occurs when new images are acquired. Upon arrival of a new SAR image, we form a number of interferometric combinations using this image. We then use the stored sibling information to estimate the coherence for the new interferograms. This coherence estimate is completely independent for every interferogram, allowing for great flexibility in parallel processing. Although we assume the sibling information stays valid for several months, we re-estimate the siblings based on the most recent dataset after a certain amount of new images have been acquired, to ensure the sibling information stays up to date. Section 2.2.2 describes how we estimate coherence, and in what way we use this coherence to select coherent points in each interferogram.

2.2.1 Sibling identification

From the initial set of single master interferograms, we can form all possible interferometric combinations. We use this full set of interferograms to estimate a set of siblings for every pixel. For each pixel, we first calculate the mean amplitude over all interferometric combinations:

$$A_{mean,j} = 1/N \sum_{i=1}^{N} A_{i,j}, \tag{2.1}$$

where A is the interferometric amplitude, j represents an arbitrary pixel, and N is the number of interferograms. We then compare the mean amplitude of the pixel to the mean amplitude of each pixel in a surrounding window. Points with a mean amplitude within a percentage threshold of the current pixel are accepted as siblings. Both the window size and the mean amplitude percentage threshold are set by the user, with typical values ranging from 20 to 40 pixels for the window size, and 5-15% for the threshold.

We also consider the mean amplitude difference between the master and slave over all interferometric combinations. For each pixel, we calculate the mean amplitude difference as:

$$\Delta A_{mean,j} = 1/N \sum_{i=1}^{N} (A^M_{i,j} - A^S_{i,j}), \tag{2.2}$$

where $\Delta A_{mean,j}$ is the mean amplitude difference for pixel j, $A^M_{i,j}$ represents the master amplitude of interferogram i for pixel j, and $A^S_{i,j}$ the slave amplitude. For each pixel, we ensure that the selected siblings are also within a percentage threshold of the mean amplitude difference, dropping those for which this is not the case. This helps to ensure that points belong to similar scattering surface types. Typical values for the amplitude difference threshold are 10-30%. Contrary to many other techniques that use siblings, we do not enforce connectedness of siblings, as our application does not require it, and a wide spread of points can actually improve coherence estimation reliability in many cases.

Also contrary to many other techniques, we do not use statistical hypothesis testing on the amplitude vectors of pairs of pixels to select our siblings, opting instead to use the mean amplitude and the mean amplitude difference. We made this choice for several reasons. Firstly, calculating the mean and the mean amplitude difference is less complex than performing the hypothesis testing, therefore taking less time. Equally critical is that during sibling identification, only the mean amplitude and mean amplitude difference have to be kept in memory, as opposed to the full amplitude stack for all combinations, vastly reducing RAM memory and disk read requirements. Finally, the hypothesis tests tend to result in a binary result, either the hypothesis is true, or false. We require a minimum number of siblings in the ensemble to obtain a reasonably unbiased estimate for the coherence (see Section 2.2.2), and thus enforce a minimum number of siblings (typically between 10 and 30). If a pixel does not have sufficient siblings within the threshold, we can add the best sibling candidates outside of the threshold. The same is true if we impose a maximum on the amount of siblings, where we can reject the worst siblings that fall within the threshold.

2.2.2 Coherence estimation and point selection

When a new image is acquired and co-registered with respect to the common master, we already have for every pixel a pre-identified ensemble of sibling pixels. Similar to the "boxcar" method described above, we can now use this sibling ensemble to estimate the coherence:

$$\hat{\gamma} = \frac{\left|\frac{1}{n}\sum_{i=1}^{n} M_i \cdot \bar{S}_i\right|}{\sqrt{\frac{1}{n}\left(\sum_{i=1}^{n} M_i \cdot \bar{M}_i \sum_{i=1}^{n} S_i \cdot \bar{S}_i\right)}}, \tag{2.3}$$

where n represents the number of points in the ensemble, M represents the master image signal for an arbitrary point, and S represents the slave image signal. The overline indicates the complex conjugate. As siblings are points with similar scattering characteristics, this method avoids or largely mitigates the problems the boxcar method has; high coherence targets do not smear out, as they are not part of the sibling ensemble of nearby points with lower coherence, and the chance of erroneously high coherence estimates is reduced, as larger ensembles can be used.

We can use the estimated coherence to select points from the full resolution interferograms directly, and in some cases this might be preferable. However, if high resolution is not required, it is preferable to select points from multilooked versions of the interferograms. Using the sibling based ensemble to estimate the coherence reduces the spatial correlation between coherence estimates, but it does not completely remove the issues with erroneously high coherence estimates in incoherent areas. However, as these erroneously high estimates no longer smear out, multilooking reduces them to low values, even for small multilook factors.

To select points in the multilooked image, we need to obtain a measure of the quality of each multilooked point. Averaging the coherence is not appropriate, e.g. the coherence of a multilooked point consisting of 100 points with coherence 0.6 is significantly higher than the mean of 0.6. In stead, we use the Cramer-Roa relationship to calculate a variance for each point based on its coherence (*Hanssen*, 2001):

$$\sigma_{CR}^2 = \frac{1 - |\gamma|^2}{2|\gamma^2|} \tag{2.4}$$

This allows us to weight the interferometric signal by the inverse of the variance before multilooking, as well as calculate a variance for the resulting multilooked point by propagating the uncertainty, which we can then use to select points.

The multilooking is especially effective in creating contrast between incoherent areas, and areas with low coherence. For incoherent areas, the occasional, chancy low variance (high coherence) estimate is averaged with the high variance estimates surrounding it, resulting in an overall high variance. For low coherence areas, the coherent, low variance

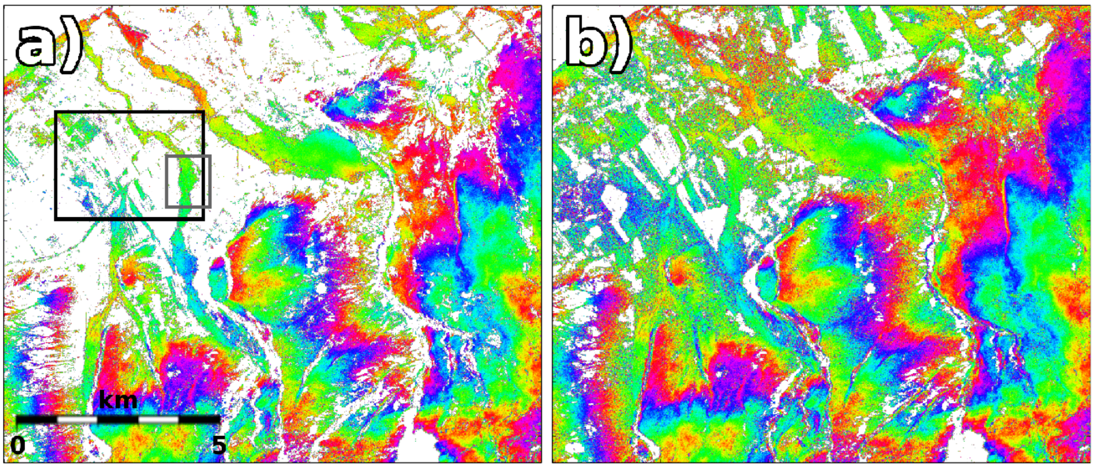

Figure 2.2: Comparison between points selected in a) full resolution, and b) after multilooking. The variance threshold was set, independently for each interferogram, based on the 99 percentile variance in the ocean (top left corner). The interferogram shown (20090618-20090629) covers the full test area. The area shown in Figs. 2.1 and 2.4 is indicated by the black box, and the grey box indicates the area shown in Fig. 2.3.

points within a multilook window lower the overall variance within it. This effect is enough to differentiate between incoherent and low coherence areas (Fig. 2.2). As hinted at above, this averaging works for the sibling based coherence, since neighbouring points do not necessarily use a similar set of points for the coherence estimate. Averaging of the coherence would not work with the boxcar method, as the ensembles used to calculate the coherence for neighbouring points share 80–90% of their pixels, thus yielding highly spatially correlated coherence estimates.

After selecting the points with sufficient coherence, we filter them using a Goldstein filter (*Goldstein and Werner*, 1998). To allow unwrapping, we use region growing to fill empty points in the grid, similar to the method used in StaMPS (*Hooper et al.*, 2007). The high coherence interferograms allow us to use two-dimensional, spatial unwrapping with high success rates. We use the public domain software SNAPHU (*Chen and Zebker*, 2001), which uses a minimum cost flow approach to solve for the phase ambiguities. The algorithm described above allows us to estimate the coherence for every interferogram individually, providing us with much greater flexibility in terms of parallel processing. We implemented the processing strategy to take full advantage of parallel processing, greatly improving processing efficiency and time.

2.2.3 Optional processing steps

Besides being able to take advantage of parallel processing, another advantage of the ability to process images individually is the flexibility in applying extensions dealing with specific challenges present in individual images. One of the potential pitfalls of using Eq. 2.3 is that it assumes no systematic variability in the phase of all the points within the ensemble used to calculate the coherence. However, in the case of high deformation rates, or high frequency nuisance signals, this is clearly not the case, and results in an underestimation of the coherence for these kind of areas. Our method uses points distributed over a larger area than the boxcar method, exacerbating the problem. For images with high frequency systematic phase, we estimate the spatially correlated phase component of the interferogram by filtering, and removing this phase component from the interferometric phase. We then use the residual, “flattened” phase to estimate the coherence. The filtering is done either using multilooking, or using a combined low-pass adaptive filtering (*Hooper*, 2008). Although removing the spatially correlated phase from interferograms eliminates the underestimation of coherence in areas of high (coherent) phase variability, it comes at the cost of increased processing time, and an overestimation of the coherence in incoherent areas (see Section 2.3.4). We therefore choose to make the filtering of the phase optional, allowing it to be run on specific images only.

Another optional processing step deals with variability in the siblings with time. An example of this can be seen in Fig. 2.3 a) and b), where an incoherent river can be seen on the right side of the scene in the wrapped phase, but does not show up in the sibling based coherence estimate. The river is a glacial outlet river, that tends to shift due to deposit and flow rate changes. This means that siblings in the otherwise very coherent riverbed will not belong to the same type of scatterer for certain images. In the case of the river, a point in the river will have a few siblings within the incoherent river, but also many siblings on the coherent riverbed. This will result in a high coherence estimate, even though the point itself is clearly incoherent. The random phase within these incoherent areas may cause unwrapping errors, which makes it important to solve this issue. We deal with it by (optionally) evaluating the validity of the sibling information. We commence by estimating the boxcar coherence for the interferogram in question using a small window (typically 5x5 pixels). We then compare the boxcar coherence value for every point to all its siblings, and reject the one third of siblings with the largest difference in coherence compared to the current point. We only use the remaining siblings to estimate the coherence for the point in question. This naturally comes at the cost of additional processing time, and potentially the requirement of raising the number of siblings per point to be estimated in the first place.

2.3 Eyjafjallajökull case study

Around the time of the 2010 Eyjafjallajökull eruption (*Sigmundsson et al.*, 2010a), a large set of TerraSAR-X SAR images were obtained covering the volcano. This dataset represents one of the first demonstrations of the possibilities offered by the high acquisition rates of current satellites. The high data acquisition frequency, and the resulting high coherence form a good example of the expected data quality in the years to come.

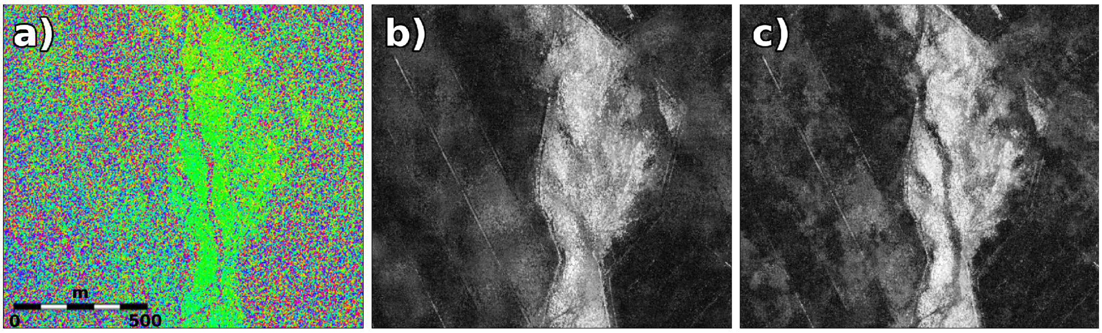

Figure 2.3: Demonstration of the effect of temporarily changing siblings, and the optional sibling rejection proposed to resolve it. a) The wrapped interferometric phase of interferogram 20090618-20090629 b) The estimated sibling based coherence without sibling rejection c) The estimated sibling based coherence, using the same siblings as in image b), but with a third of the siblings rejected. The area covered is a zoom of the river bed visible in the bottom right side of Fig. 2.1.

2.3.1 Coherence estimate and multilooking

A comparison between the boxcar and the sibling coherence estimates for a region covering the south flank and coast of Eyjafjallajökull (5000 by 5000 pixels) is given in Fig. 2.1. The advantages of the sibling coherence estimate over the boxcar method are clearly visible. As described in Section 2.1, the boxcar method tends to smear out coherence, leading to smaller roads becoming invisible in the coherence estimate, and high coherence buildings and wider roads influencing the coherence of the surrounding pixels. This effect increases as the window size increases, as coherence gets calculated over more points. The sibling coherence estimate does not suffer from this smearing problem, as is evident from the sharper looking coherence image.

The sibling coherence estimate also does not suffer from the high frequency noise that appears in the boxcar coherence estimate, present in areas of lower overall coherence. This speckle-like noise is caused either by neighbouring, noisy pixels having similar phase by chance, or by one pixel in the ensemble having a high amplitude compared to the remaining pixels and dominating the coherence estimation. It is therefore more prevalent when a smaller window is used, as the coherence is calculated using fewer points, increasing the chance of a biased coherence estimate due to either of the two aforementioned reasons. However, even the very large 11x11 window is not sufficient to overcome this problem. The sibling coherence estimate, on the other hand, appears visually to perform much better (Fig. 2.1). To evaluate quantitatively whether our new approach is actually estimating coherence more reliably, we use phase variance of points with estimated coherence above a certain threshold, as a proxy. For each of the three coherence estimates shown in Fig. 2.1, we select all points with a coherence over 0.5. For each point, we calculate the variance of the phase values of selected points in a 21 by 21 window surrounding the point. To ensure a reasonable variance estimate,

Table 2.1: Estimated mean phase variance as a proxy for the quality of the three coherence estimates shown in Fig. 2.1, as well as a boxcar coherence estimate with a 17 by 17 window.

Method	Mean phase variance [rad^2]
Boxcar 5x5	1.725
Boxcar 11x11	1.517
Boxcar 17x17	1.550
RapidSAR	1.308

we only take into account points with at least 10 selected points in the search window. We also calculated the phase variance for a 17 by 17 window boxcar estimate. Table 2.1 shows the mean phase variance for the four coherence estimates. The lower mean phase variance demonstrates that the RapidSAR coherence estimate is superior to the three boxcar estimates.

One of the main reasons why the sibling coherence estimate suffers less from the two problems described becomes apparent when looking at the number of siblings selected for each pixel (Fig. 2.4). It shows that objects with stable scattering properties, especially those surrounded by areas of lower overall coherence, tend to have fewer siblings. These pixels use only the few pixels that contain the same or similar objects (e.g. buildings, roads, cliff faces), not allowing points with different scattering mechanism surrounding these objects to influence the coherence and smear it out. Vice versa, good scatterers do not raise the coherence of surrounding points as well. Furthermore, in fields and other low coherence areas, pixels tend to have a high number of siblings, often the maximum number allowed. This, combined with the fact that neighbouring points can have very different siblings, drastically reduces the noise in the coherence estimate seen in the boxcar coherence.

The coherence estimate obtained using the sibling information is converted to a variance using Eq. 2.4, and subsequently used to weight the pixels during multilooking. The benefit of weighted multilooking compared to normal multilooking is most apparent in low coherence areas. Figure 2.5 shows a comparison of the effect of normal and weighted multilooking on an interferogram affected by snow cover. Especially after filtering, it becomes clear that the amount of signal retrieved is much higher for weighted multilooking, greatly aiding in the unwrapping of these interferograms.

2.3.2 Point selection and unwrapping

Although we estimate the coherence of every point at full resolution, we typically select points on a (slightly) multilooked version of the interferogram, as described in Section 2.2.2. The reason for this becomes clear when looking at Fig. 2.2. The selection method after multilooking is indeed better able to distinguish between low coherence fields and incoherent areas like the ocean (top left corner).

To evaluate the performance of our coherence estimation and point selection routine,

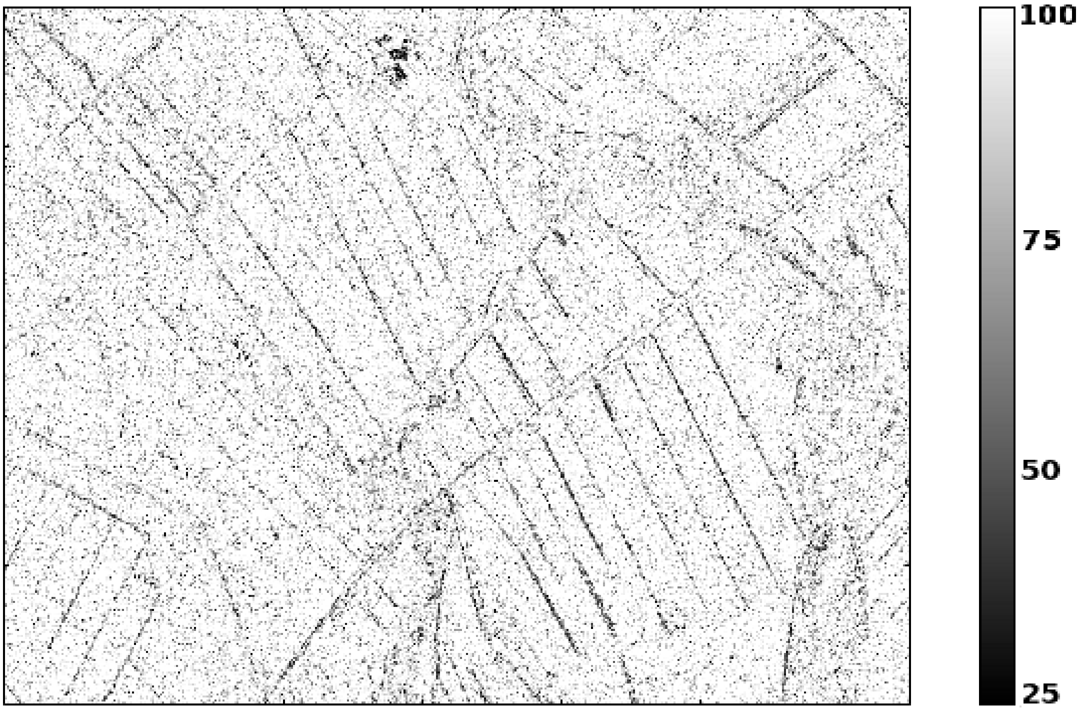

Figure 2.4: Overview of the number of siblings for every pixel. A minimum of 25 siblings per pixel was imposed to ensure a reasonably unbiased estimate for the coherence, and a maximum of 100 for efficiency. The area shown covers the same area as Fig. 2.1.

we compare in Fig. 2.6 points selected using the RapidSAR method (middle column) to an SB time series method (right column) for three different interferometric combinations. For reference, we also show the full, non-multilooked wrapped phase values. For the RapidSAR coherence estimate, each pixel has between 25 and 100 siblings selected, using all possible combinations of 17 images between July 2009 and March 2010. A search window of 40 pixels was used to find siblings, and the amplitude percentage threshold was set to 10%. The small baseline processing was achieved using the small baseline module in StaMPS (*Hooper*, 2008), which uses phase stability through time to estimate a temporal coherence measure. A selection threshold of 2% random points was set, and only interferograms with high expected coherence based on the temporal and perpendicular baselines were used in the network (*Hooper*, 2008).

The three combinations shown are chosen for their different levels of coherence, and their different decorrelation mechanisms. The top row shows a high coherence, small baseline combination, as is typically expected for current short repeat cycle satellites like TerraSAR-X, Cosmo-SkyMed and Sentinel 1. The RapidSAR method clearly selects more points compared to the SB method. The main reason for this is that the SB method selects a single set of points for all interferograms, only selecting points that stay consistently coherent. This leads to a significant loss in information that is extracted from the interferograms. The reason why the SB method selects fewer points in the

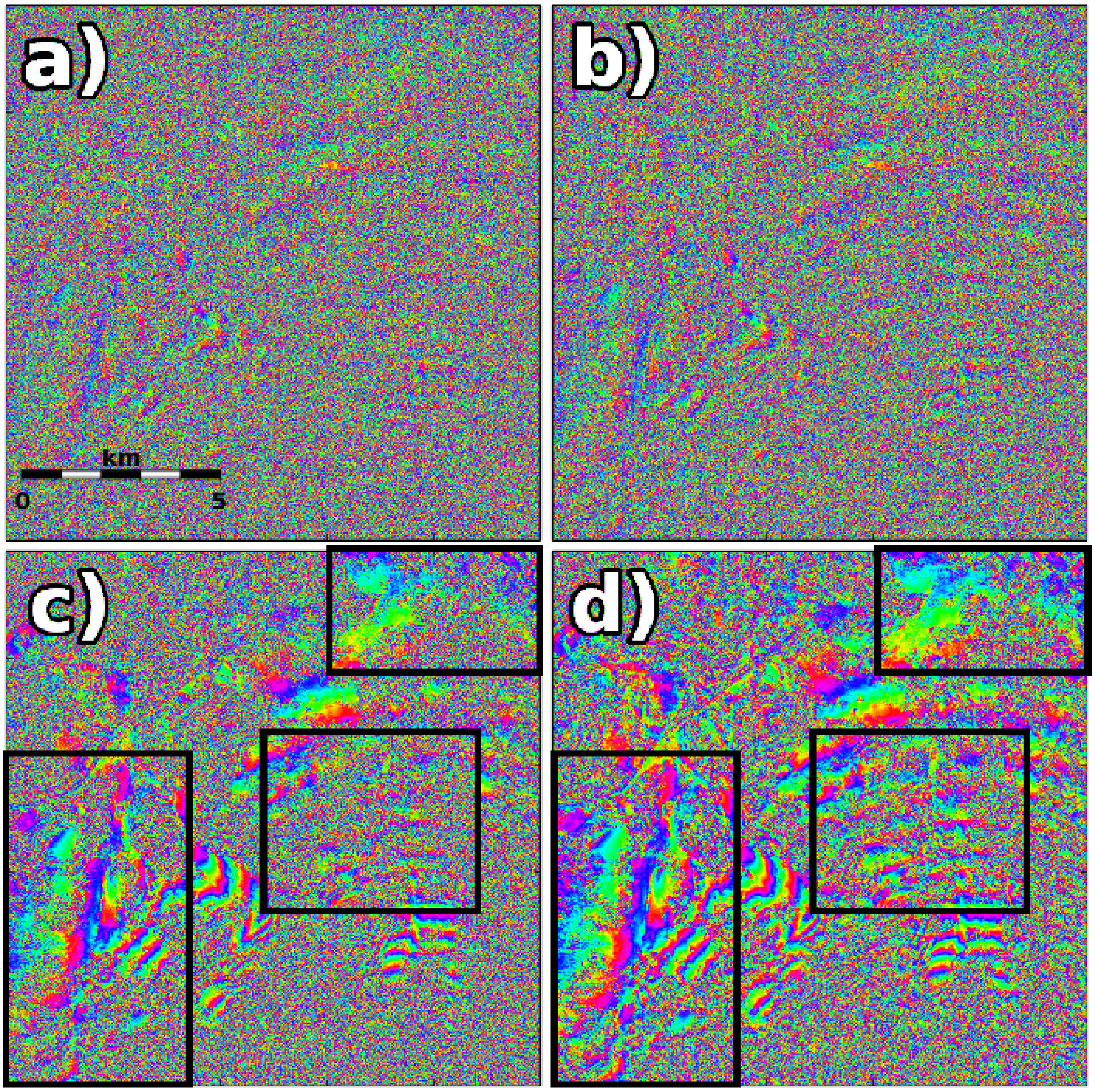

Figure 2.5: Comparison between normal and weighted multilooking for a very low coherence interferogram due to snow cover. The interferogram (20100204-20100331) is different from that shown in previous figures, but covers the same area as shown in Fig. 2.1 and is part of the same dataset used to identify siblings. Panel a) and b) show the standard and weighted multilooked phase, respectively. A multilooking window of 5x5 was used. Panels c) and d) show the filtered phase of panels a) and b), respectively. Although the difference between panels a) and b) are subtle, the difference between panels c) and d) clearly shows the value of using weighted multilooking on low coherence images. The black boxes highlight some areas of improvement.

Table 2.2: Processing time to calculate the coherence of 10 interferometric combination of a 5000 by 5000 TerraSAR-X scene, for varying number of processing cores. Approximately 8 Gb of RAM memory was used during all processing runs.

Number of CPUs	Processing time [min]
2	84.6
4	58.4
8	45.9
16	36.5

top left half of the scene become apparent when looking at the longer temporal baseline combination shown in the middle row of Fig. 2.6. The top left area of the scene consists mainly of agricultural fields, which decorrelate rapidly over time. Due to combinations like this one, with images separated in time by three months, the SB method selects fewer points in all interferogram for this area. The RapidSAR method selects few points in the area for the long temporal baseline combinations only, without affecting other combinations.

The bottom row of Fig. 2.6 shows another problem caused by the limitation of selecting one set of points. Inherently, this selection becomes a trade-off between retaining signal in high-quality interferograms and reducing noise in lower quality interferograms (*Hooper et al.*, 2011b). The scene in the bottom row is a winter acquisition, heavily decorrelated due to snow cover on the higher altitude area in the bottom right half of the scene. As there are few winter acquisitions in the time series, the small baseline method selects many points in the affected area, the majority of which contain no signal. Our method selects few points in the area, most of which are on rocky outcrops. Fig. 2.6 clearly shows the advantage of individual point selection for each interferogram, and demonstrates the effectiveness of the RapidSAR method for revisit times typical in current satellites.

The processing time necessary to process the scene in Fig. 2.6 depends heavily on the computational facilities used. One of the most critical variables for performance in the amount of processor cores. Table 2.2 gives a representative example of processing times of the coherence estimate for the same set of 5000 by 5000 pixel interferograms. A clear diminishing return can be seen on the amount of processing cores used. Partly this is due to overhead for the parallel computations, but mostly this is caused by the certain operations not allowing parallelisation. The processing times given here are meant as an indication of expected processing times, and could be improved in several ways (e.g. increased internal memory or optimized implementation).

The high density of coherent selected points allows for effective filtering and unwrapping of the phase. Fig. 2.7 shows the filtered and unwrapped phase of the points selected using our method for the high quality, short baseline acquisition of Fig. 2.6. The smooth, filtered phase is unwrapped effectively, even given the complex nature of the wrapped phase pattern and the many discontinuities. Fig. 2.8 shows an incremental

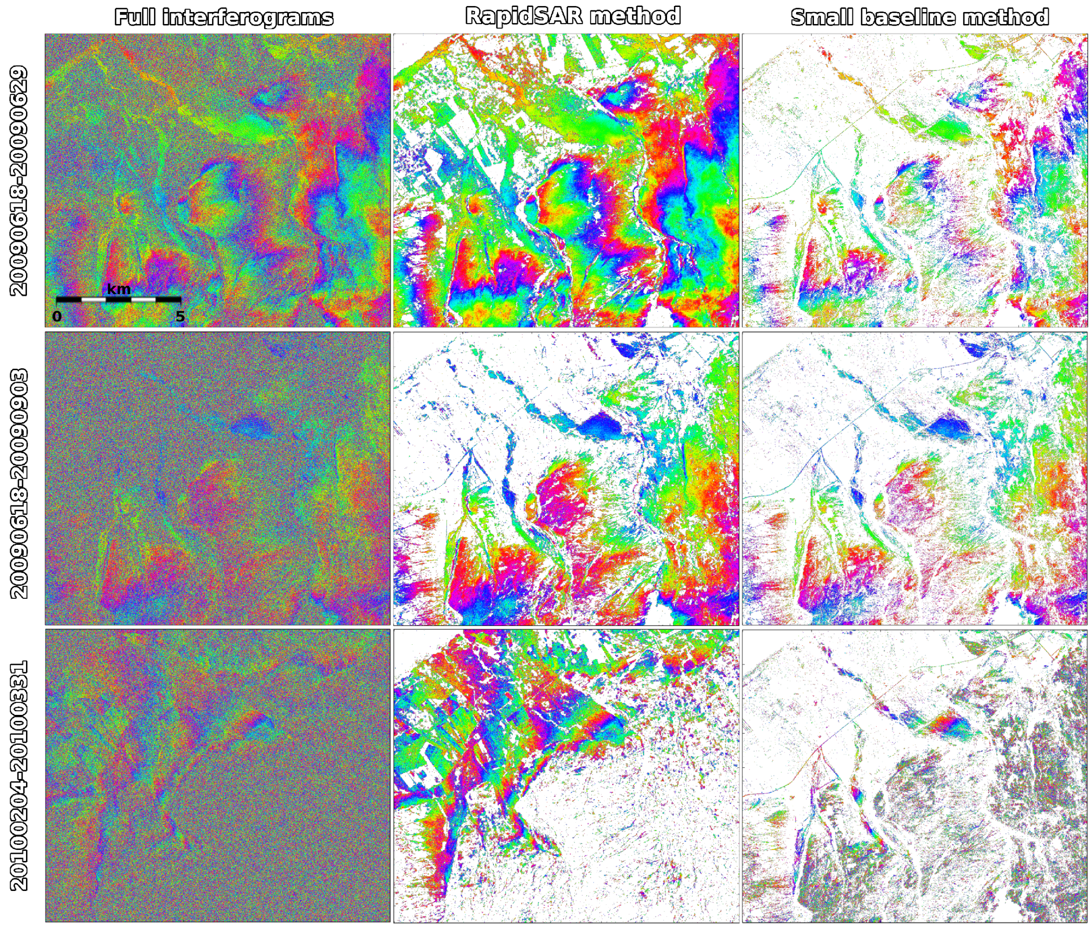

Figure 2.6: Comparison of selected points using the RapidSAR method (middle column) and small baseline processing (right column). Both selections are plotted in the same resolution. For comparison, the full, non-multilooked interferograms are shown in the left column. Three different interferometric combinations are shown: A short temporal baseline, highly coherent summer acquisition (20090618-20090629, top row), a combination with a longer, 3-month baseline (20090618-20090903, middle row) and a short temporal baseline, winter acquisition (20100204-20100331, bottom row). Area shown is the same as in Fig. 2.2

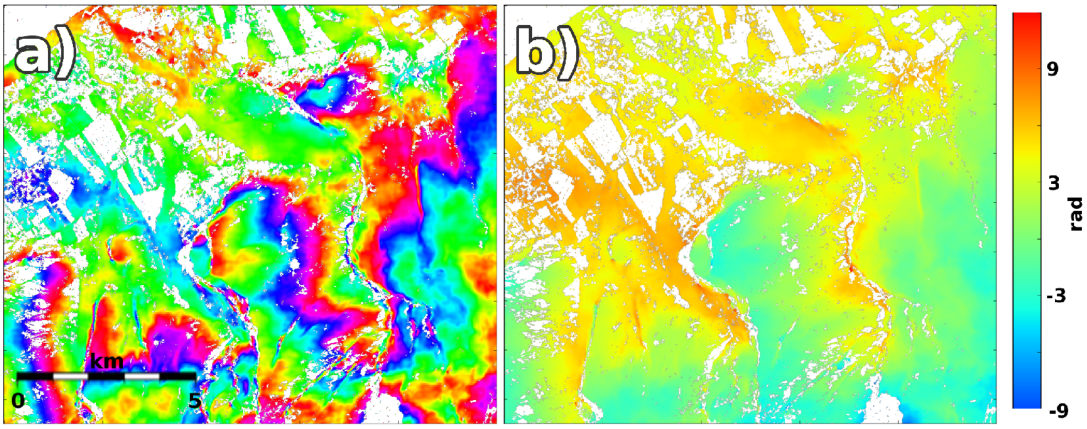

Figure 2.7: Demonstration of the phase unwrapping for interferogram 20090618-20090629 (same as top row of Fig. 2.6). a) Filtered phase values b) Unwrapped phase values.

timeseries processed using the RapidSAR method.

2.3.3 Optional sibling rejection

As described in Section 2.2.3, our method is less effective where sibling relationships temporarily change. This problem mostly occurs when a thin band of points decorrelate with respect to their surrounding siblings, such as along a river with highly varying water levels. Fig. 2.3 c) shows the result of the optional processing step designed to deal with this issue. We rejected one third of the siblings for every point, based on the 5x5 boxcar coherence estimate for every point. For temporarily decorrelated points in the river, this resulted in many of the siblings that were in the coherent river bed being rejected, greatly reducing the coherence estimated for those points. The coherence estimate in the low coherence fields also changes slightly. It is difficult to evaluate if this slight change in the fields is an improvement. However, due to the nature in which we select points, after multilooking, this difference largely disappears.

2.3.4 Optional phase flattening

Fig. 2.9 shows an interferogram (19500 by 19000 pixels) covering the initial weeks of 2014-2015 Bárðarbunga-Holuhraun eruption (*Sigmundsson* et al., 2015). In the week leading up to and the weeks after the eruption, relative deformation of over 2 meters was measured over less than 20 km (*Sigmundsson* et al., 2015). Such high deformation gradients lead to a high variability in the interferometric phase, as is evident in the interferogram shown in Fig. 2.9. As discussed before, the coherence estimation using Eq. 2.3 is essentially a measure of the phase variability of the points in the ensemble. Thus, a high systematic phase gradient will lead to an erroneously low coherence estimate. Panels b) and d) in Fig. 2.9 show the effectiveness of removing the spatially correlated phase from the interferogram before estimating coherence. This makes it clear that in

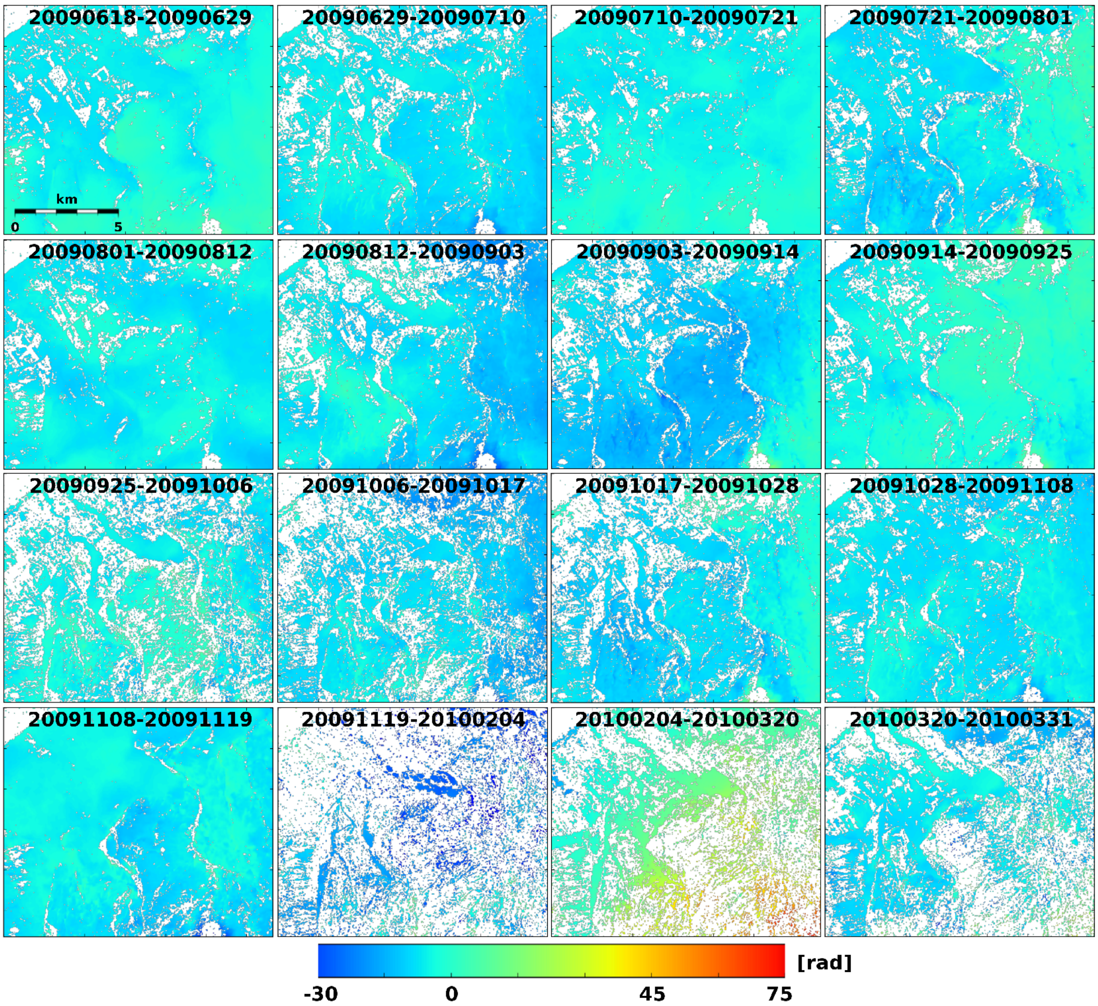

Figure 2.8: Incremental timeseries of unwrapped phase values of selected points for all interferograms for the same scene as covered by Fig. 2.2. Unwrapped phase values are referenced to an area on the coast (top left corner). The Eyjafjallajökull volcano is to the bottom right of the scene. Deformation associated with the first eruptive episode of the 2010 Eyjafjallajökull eruption, which commenced on the 20th of March, 2010 (*Sigmundsson et al.*, 2010b), is clearly visible in the interval 2 February 2010 and 20 March 2010, even though it is one of the lowest coherence pairs in the time series.

interferograms with high fringe rates, it is essential to remove the spatially correlated phase before estimating coherence. However, filtering the phase also removes part of the phase variability in completely decorrelated areas, slightly raising the coherence there. This results in the need for a lower variance threshold, leading to a loss of signal.

2.4 Conclusions and outlook

We present RapidSAR, a new algorithm that is able to handle the high volumes of data that current generation SAR satellites produce, and produce high signal-to-noise ratio deformation maps in a timely fashion. RapidSAR is developed for volcano monitoring, where timely processing of the data is key. Besides the relatively fast processing time, the individual coherence estimate and subsequent point selection allows us to avoid the selection compromise inherent in most other time series methods. The efficiency of the algorithm in extracting coherent points from high coherence datasets also makes it suitable for other surface deformation applications. The algorithm will be used operationally to monitor volcanic systems in Iceland as part of the FutureVolc project. With the successful operation of Sentinel 1A since late 2014, a freely available, nearly constant stream of SAR data has become available. Sentinel 1A acquisitions cover large areas, albeit at a lower resolution compared to TerraSAR-X and Cosmo-SkyMED. This means that Sentinel 1A data contains fewer points per unit area. Combined with the natural data partitioning resulting from the TOPS mode bursts (*De Zan and Guarnieri*, 2006), our method is fully scalable to handle Sentinel 1A data.

RapidSAR is well suited to relatively short baseline time series, as obtained over most volcanic systems by current satellite systems. There may however be some situations where methods like the PS and small baseline techniques may perform better, and the techniques should therefore be seen as complimentary. Especially for steady, small scale signals, PS and Small Baseline may perform better due to the way in which they select points. In this case, the fact that they select the same points in every image will also aid in unwrapping and estimating nuisance signals, even though it might lead to a loss of information. The loss of information is mitigated by using methods like SqueeSAR or CAESAR, but these techniques require even more processing power, making them less suited to routine, automated processing of data over numerous areas of interest.

The focus of the RapidSAR methodology is on near-real time monitoring, where the main importance lies in what has happened in the period between the latest two acquisitions. It is here where our method really outperforms other timeseries methods, which excel at extracting long term steady state deformations, but tend to struggle with sudden changes in deformation rates and/or patterns. This fact, combined with the point selection compromise in other timeseries methods, makes RapidSAR well suited to monitoring volcanoes and other deforming processes. Although not currently a focus of the method, the increase in information extracted from the dataset should

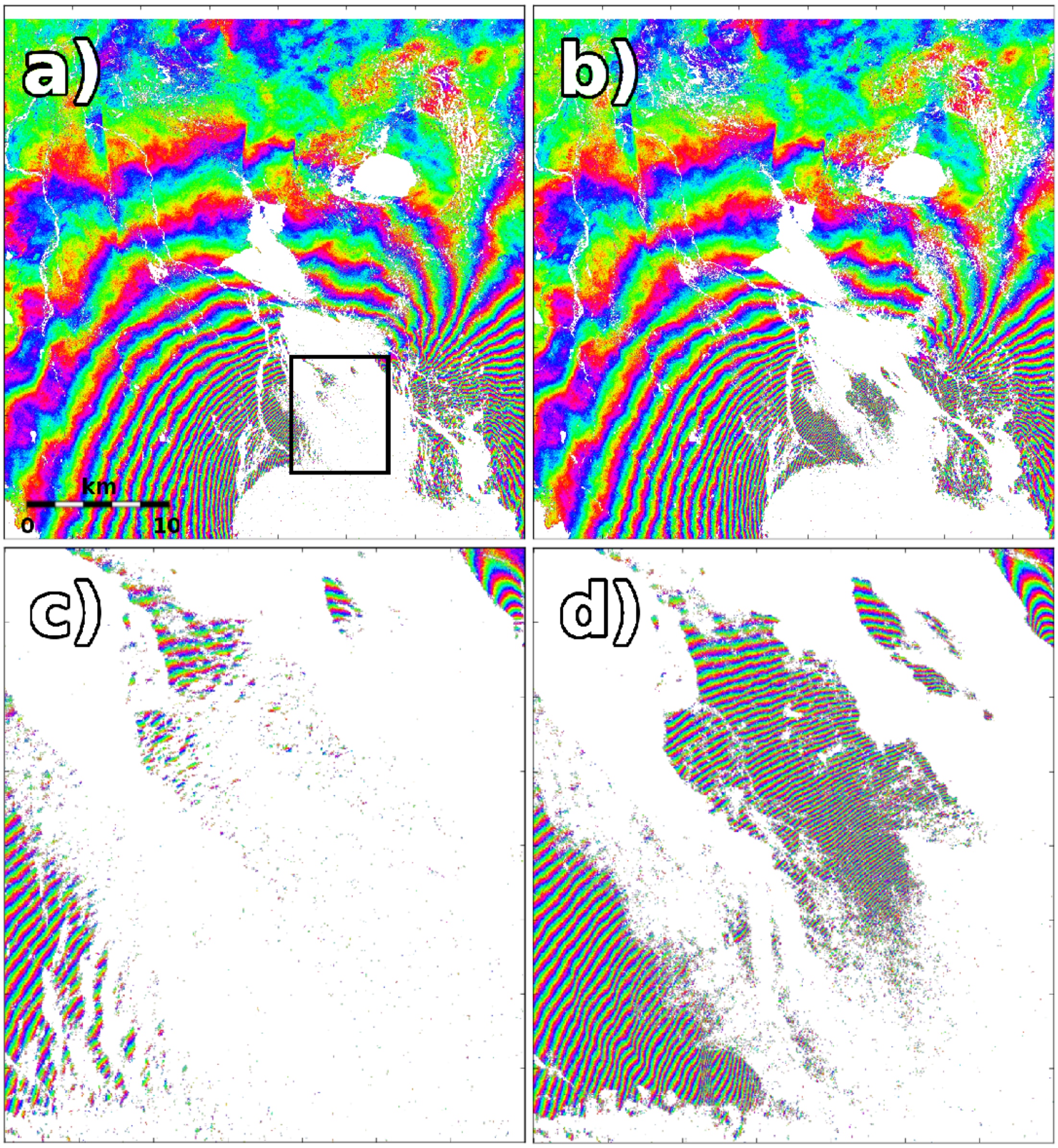

Figure 2.9: The effect of optionally removing the spatially correlated phase from interferograms before estimating coherence. The interferogram covers the 2014 Bárðarbunga-Holuhraun eruption and was generated using data obtained by the Cosmo-SkyMed satellite constellation. Panel a) shows the points selected using coherence estimated with the original phase. Panel b) shows points selected using coherence estimated after removing the filtered phase. Panels c) and d) show a closer look at the fast deforming areas of panels a) and b), respectively, as outlined by the black box in panel a).

also profit longer term time series generation. The variable set of points selected in each interferogram will make time series generation more complex, however, and will need to be addressed in the future.

Further improvements to our method are certainly possible. There are other ways in which siblings could be identified, especially with an eye to the current Sentinel-1 mission, which captures dual-polarisation data in its standard operation mode. Using polarimetric information could prove very useful in identifying siblings, and also in rejecting siblings on an image by image basis (Section 2.2.3). Polarimetry can further be used to find the optimal combination of polarimetric channels, which will yield interferograms with higher coherence (e.g. (*Navarro-Sanchez and Lopez-Sanchez*, 2012)). Furthermore, although the overall good coherence of the short temporal baseline interferograms of current missions greatly aids the phase unwrapping, a more advanced unwrapping algorithm could incorporate the sparse information in the time domain would improve reliability.

Acknowledgements

KS is funded through the FutureVolc project, which received funding through the European Union's Seventh Programme for research, technological development and demonstration under grant agreement No 308377. COSMO-SkyMed data were provided by the Italian Space Agency (ASI) and TerraSAR-X data by the German Space Agency (DLR) through the Icelandic Volcanoes Supersite project supported by the Committee on Earth Observing Satellites (CEOS). Information on how to access the data for this paper can be obtained by contacting the corresponding author at eekhs@leeds.ac.uk.

References

Amelung, F., S. Jónsson, H. Zebker, and P. Segall (2000), Widespread uplift and "trapdoor" faulting on Galápagos volcanoes observed with radar interferometry, *Nature*, *407*, 993–996, doi:10.1038/35039604. 2.1

Bamler, R., and P. Hartl (1998), Synthetic Aperture Radar interferometry, *Inverse Problems*, *14*, 1–54. 2.1

Basilico, M., A. Ferretti, F. Novali, C. Prati, and F. Rocca (2004), Advances in permanent scatterers analysis: Semi and temporary PS, *Proc. Eur. Conf. Synthetic Apertude Radar*, pp. 349–350. 2.1

Berardino, P., G. Fornaro, R. Lanari, and E. Sansosti (2002), A new algorithm for surface deformation monitoring based on small baseline differential SAR interferograms, *IEEE Transactions on Geoscience and Remote Sensing*, *40*(11), 2375, doi:10.1109/TGRS.2002.803792. 2.1

Chen, C., and H. Zebker (2001), Two-dimensional phase unwrapping with use of statistical models for cost functions in nonlinear optimization, *J. Opt. Soc. Am. A*, *18*(2), 338–351, doi:10.1364/JOSAA.18.000338. 2.2.2

De Zan, F., and A. Guarnieri (2006), TOPSAR: Terrain observation by progressive scans, *Ieee Transactions On Geoscience And Remote Sensing*, *44*(9), 2352–2360, doi:10.1109/TGRS.2006.873853. 2.4

Deledalle, C., L. Denis, and F. Tupin (2011), NL-InSAR: Non-local interferogram estimation, *IEEE Trans. Geosc. Rem. Sens.*, *49*(4), 1441–1452, doi:10.1109/TGRS.2010.2076376. 2.1

Ferretti, A., C. Prati, and F. Rocca (2001), Permanent Scatterers in SAR Interferometry, *IEEE Transactions on geoscience and remote sensing*, *39*(1), 8–20, doi:0196{--}2892/01. 2.1

Ferretti, A., A. Fumagalli, F. Novali, C. Prati, F. Rocca, and A. Rucci (2011), A New Algorithm for Processing Interferometric Data-Stacks: SqueeSAR, *IEEE Transactions on Geoscience and Remote Sensing*, *49*(9), 3460, doi:10.1109/TGRS.2011.2124465. 2.1

Fornaro, G., S. Verde, and D. Reale (2015), CAESAR: An approach based on covariance matrix decompositon to improve multibaseline-multitemporal interferometric SAR processing, *IEEE Trans. Geosc. Rem. Sens.*, *53*(4), 2050–2065, doi:10.1109/TGRS.2014.2352853. 2.1

Gabriel, A., R. Goldstein, and H. Zebker (1989), Mapping small elevation changes over large areas: Digital radar interferometry, *J GEOPHYS RES*, *94*(B7), 9183–9191. 2.1

Goldstein, R., and C. Werner (1998), Radar interferogram filtering for geophysical applications, *Geophysical research letters*, *25*(21), 4035–4038. 2.2.2

Hanssen, R. (2001), Radar interferometry: Data interpretation and error analysis, Ph.D. thesis, Delft University of Technology. 2.1, 2.2.2

Hooper, A. (2008), A multi-temporal InSAR method incorporating both persistent scatterer and small baseline approaches, *Geophys Res Lett*, *35*(16), doi:10.1029/2008GL034654. 2.1, 2.2.3, 2.3.2

Hooper, A. (2009), A statistical-cost approach to unwrapping the phase of InSAR time series, *Proceedings FRINGE Workshop*. 2.1

Hooper, A., P. Segall, and H. Zebker (2007), Persistent scatterer interferometric synthetic aperture radar for crustal deformation analysis, with application to Volcán Alcedo, Galápagos, *Journal of Geophysical Research*, *112*(B7), doi:10.1029/2006JB004763. 2.1, 2.2.2

Hooper, A., B. Ófeigsson, F. Sigmundsson, B. Lund, P. Einarsson, H. Geirsson, and E. Sturkell (2011a), Increased capture of magma in the crust promoted by ice-cap retreat in Iceland, *Nature Geoscience*, *4*, 783–786, doi:10.1038/ngeo1269. 2.1

Hooper, A., D. Bekaert, K. Spaans, and M. Arıkan (2011b), Recent advances in SAR interferometry time series analysis for measuring crustal deformation, *Tectonophysics*, *514-517*, 1–13, doi:10.1016/j.tecto.2011.10.013. 2.3.2

Lee, J. (1983), Digital noise smoothing and the sigma filter, *Comput. Vis. Graph. Image Process.*, *21*, 255–269. 2.1

Li, F., and R. Goldstein (1990), Studies of multibaseline spaceborne interferometric synthetic aperture radars, *IEEE Trans Geosci Remote Sensing*, *28*(1), 88–97. 2.1

Navarro-Sanchez, V., and J. Lopez-Sanchez (2012), Improvement of persistent-scatterer interferometry performance by means of a polarimetric optimization, *IEEE Geosc Rem Sens*, *9*(4), 609–613, doi:10.1109/LGRS.2011.2176715. 2.4

Nicolas, J., F. Tupin, and H. Maitre (2001), Smoothing speckled sar images using maximum homogeneous region filters: An improved approach, *Proc. IEEE Int. Geosc. Remote Sens. Symp.*, *3*, 1503–1505. 2.1

Parizzi, A., and R. Brcic (2011), Adaptive InSAR stack multilooking exploiting amplitude statistics: A comparisson between different techniques and practical results, *IEEE Geosc. Remote Sens. Lett.*, *8*(3), 441–445, doi:10.1109/LGRS.2010.2083631. 2.1

Sigmundsson, F., S. Hreinsdóttir, A. Hooper, T. Árnadóttir, R. Pedersen, M. Roberts, N. Óskarsson, A. Auriac, J. Decriem, P. Einarsson, H. Geirsson, M. Hensch, B. Ófeigsson, E. Sturkell, H. Sveinbjörnsson, and K. Feigl (2010a), Intrusion triggering of the 2010 Eyjafjallajökull explosive eruption, *Nature*, *468*(7322), 426, doi:10.1038/nature09558. 2.1, 2.3

Sigmundsson, F., V. Pinel, B. Lund, F. Albino, C. Pagli, H. Geirsson, and E. Sturkell (2010b), Climate effects on volcanism: influence on magmatic systems of loading and unloading from ice mass variations, with examples from Iceland, *Philosophical Transactions Of The Royal Society A-Mathematical Physical And Engineering Sciences*, *368*(1919), 2519–2534, doi:10.1098/rsta.2010.0042. 2.8

Sigmundsson *et al.*, F. (2015), Segmented lateral dyke growth in a rifting event at Bárdarbunga volcanic system, Iceland, *Nature*, *517*, 191–195, doi:10.1038/nature14111. 2.3.4

Stephens, M. (1970), Use of the Kolmogorov-Smirnov, Cramér-Von Mises and related statistics without extensive tables, *J. R. Stat. Soc. Ser. B (Methodological)*, *32*(1), 115–122. 2.1

Touzi, R., A. Lopes, J. Bruniquel, and P. Vachon (1999), Coherence estimation for SAR imagery, *IEEE Trans Geosc Rem Sens*, *37*(1), 135–149. 2.1

Vasile, G., E. Trouvé, J.-S. Lee, and V. Buzoloiu (2006), Intensity-driven adaptive-neighborhood technique for polarimetric and interferometric SAR parameters estimation, *IEEE Trans. Geosc. Remote Sens.*, *44*(6), 1609–1620, doi:10.1109/TGRS.2005.864142. 2.1

Zebker, H., and J. Villasenor (1992), Decorrelation in interferometric radar echoes, *IEEE Trans. Geosci. Remote Sens.*, *30*(5), 950–959. 2.1

Chapter 3

Crustal movements due to Iceland's shrinking ice caps mimic magma inflow signal at Katla volcano

Karsten Spaans[1], Sigrún Hreinsdóttir[2,3], Andrew Hooper[1] and Benedikt Gunnar Ófeigsson[4]
1 COMET, School of Earth and Environment, University of Leeds, Leeds, United Kingdom
2 Nordic Volcanological Institute, Institute of Earth Science, University of Iceland, Reykjavík, Iceland
3 now at: GNS Science, Lower Hutt, New Zealand
4 Icelandic Meteological Office, Reykjavík, Iceland

Abstract

Many volcanic systems around the world are located beneath, or in close proximity to, ice caps. Mass change of these ice caps causes surface movements, which are typically neglected when interpreting surface deformation measurements around these volcanoes. These movements can however be significant, and may closely resemble movements due to magma accumulation. Here we show such an example, from Katla volcano, Iceland. Horizontal movements observed by GPS on the flank of Katla have led to the inference of significant inflow of magma into a chamber beneath the caldera, starting in 2000, and continuing over several years. We use satellite radar interferometry and GPS data to show that between 2001 and 2010, the horizontal movements seen on the flank can be explained by the response to the long term shrinking of ice caps, and that erratic movements seen at stations within the caldera are also not likely to signify magma inflow. It is important that interpretations of geodetic measurements at volcanoes in glaciated areas consider the effect of ice mass change, and previous studies should be

carefully reevaluated.

3.1 Introduction

Katla volcano in Iceland has had several periods of increased activity (*Tryggvason*, 1973) after its large eruption in 1918, the 21st since settlement of Iceland in the ninth century AD (*Larsen*, 2000). Interaction between magma and the overlying ice cap causes Katla eruptions to be explosive, with jökulhlaups (glacial outburst floods) flowing from beneath the glacier. A vast jökulhlaup from an outlet glacier on the east side of the icecap accompanied the 1918 eruption, with the water reaching heights of up to 25 m *Tómasson* (1996). Since 1918, Katla has shown several periods of increased activity. Three major jökulhlaups took place (in 1955(*Rist*, 1967), 1999(*Sigurdsson et al.*, 2000) and 2011), which were possibly the result of small eruptions that did not break through the ice cap, but may also be linked to geothermal activity.

Abutting Katla to the west is Eyjafjallajökull volcano, which caused disruption of air traffic in north-west Europe during a summit eruption between April and May 2010 (*Sigmundsson et al.*, 2010). Eyjafjallajökull had three documented historic eruptions prior to 2010. Interestingly, all three eruptions were followed by an eruption of Katla within two years (*Larsen*, 2000, *Larsen et al.*, 1999, *Sturkell et al.*, 2009). The possible connection between eruptions of the two volcanoes, combined with the high seismic activity, the historic eruption frequency of Katla and lack of recent eruptions, has led to Katla being considered as a likely volcano to erupt in the coming years (*Sturkell et al.*, 2009).

Three continuous GPS stations were installed in south Iceland in 1999 and 2000, in response to the 1999 jökulhlaup and episodes of seismic unrest at Katla, as well as two intrusions beneath Eyjafjallajökull in 1994 and 1999 (*Pedersen and Sigmundsson*, 2004, *Hooper et al.*, 2009). From 2000, two of these stations (SOHO and HVOL), located on the southern flank of Katla's central volcano, showed horizontal movement outward from the volcano (*Sturkell et al.*, 2006). A nearby station (THEY), located on Eyjafjallajökull's southern flank, did not show these horizontal movements. Together with movements observed at two benchmarks on nunataks protruding through the ice cap and seismicity beneath Katla, the horizontal movements at the SOHO and HVOL were interpreted as being due to increased pressure in a magma chamber (*Sturkell et al.*, 2008), located beneath the caldera at a depth of around 1.5 km b.s.l. (*Gudmundsson et al.*, 1994).

Another possible explanation for the movements of the two flank GPS stations is deformation resulting from ice unloading. More than 10% of Iceland is covered in ice (*Björnsson*, 1978), and the majority of these ice caps have been losing mass since approximately 1890 (*Björnsson et al.*, 2013), causing a widespread uplift signal due to Glacial Isostatic Adjustment (GIA)(*Árnadottir et al.*, 2009, *Schmidt et al.*, 2012, *Auriac* *et al.*, 2013). Besides the uplift signal, GIA also results in a horizontal movement away from the unloading source. The possibility of GIA causing the horizontal motions at SOHO and HVOL has been previously investigated based on modelling of ice mass loss over Katla alone. This study reached the conclusion that ice mass loss at Katla could not generate sufficient horizontal motion to explain the movements seen at the GPS stations (*Pinel et al.*, 2007).

Here we use a combination of satellite radar interferometry and GPS measurements to investigate the outward movement of the southern flank observed from 2000 (*Sturkell et al.*, 2009, 2008). The combined InSAR and GPS dataset provides a much improved spatial sampling density, revealing spatial patterns in the deformation field. These spatial patterns are key to pinpointing the source of any deformation.

3.2 Results

We used a set of 22 ESA Envisat images acquired along track 87, to form 21 interferograms covering the period between July 2003 and August 2009, and estimated an average velocity during this time period using the StaMPS software (*Hooper*, 2008, *Hooper et al.*, 2011). We developed an extension to StaMPS that aims to minimise the detrimental effects that low coherence images have on the number and quality of selected points (*Hooper et al.*, 2011). A short overview of the StaMPS extension can be found in the Methods section. The resulting timeseries of unwrapped interferograms is shown in Figure 3.1. From the timeseries, we generated a velocity map by estimating a constant rate for each selected point (Fig. 3.2).

Furthermore, we analyzed all available campaign and continuous GPS data from south Iceland between 2001 and 2010 (*Sturkell et al.*, 2009, 2008, *Árnadottir et al.*, 2009, *Geirsson et al.*, 2010, 2012) to estimate a velocity field for the region (Fig. 3.2, Methods). One of the main features present in the horizontal GPS velocity field is the dominant westward movement in the north-west of the scene (Fig. 3.2a)). This area is located in the South Iceland Seismic Zone, a transform zone between the Reykjanes Peninsula in the west of Iceland, and the Eastern Volcanic Zone commencing north of Katla. The area is moving mostly with the North American tectonic plate (*Geirsson et al.*, 2012), explaining the westward movements with respect to the Eurasian plate.

Both the vertical GPS and the InSAR velocity fields show an uplift signal of increasing magnitude towards the north-east of the scene (Fig. 3.2), likely due to ice unloading of Vatnajökull glacier. We used the results of a finite element model (*Schmidt et al.*, 2012) to remove the contribution of the GIA to the InSAR and GPS signal (Fig. 3.2, 3.3). The model assumes an ice model, and constrains a vertically variable rheology using vertical GPS velocities between 1993 and 2004. The best earth model has 2 layers, a 35 km thick elastic layer, overlying a visco-elastic layer with viscosity of 10^{19} Pa s (*Schmidt et al.*, 2012).

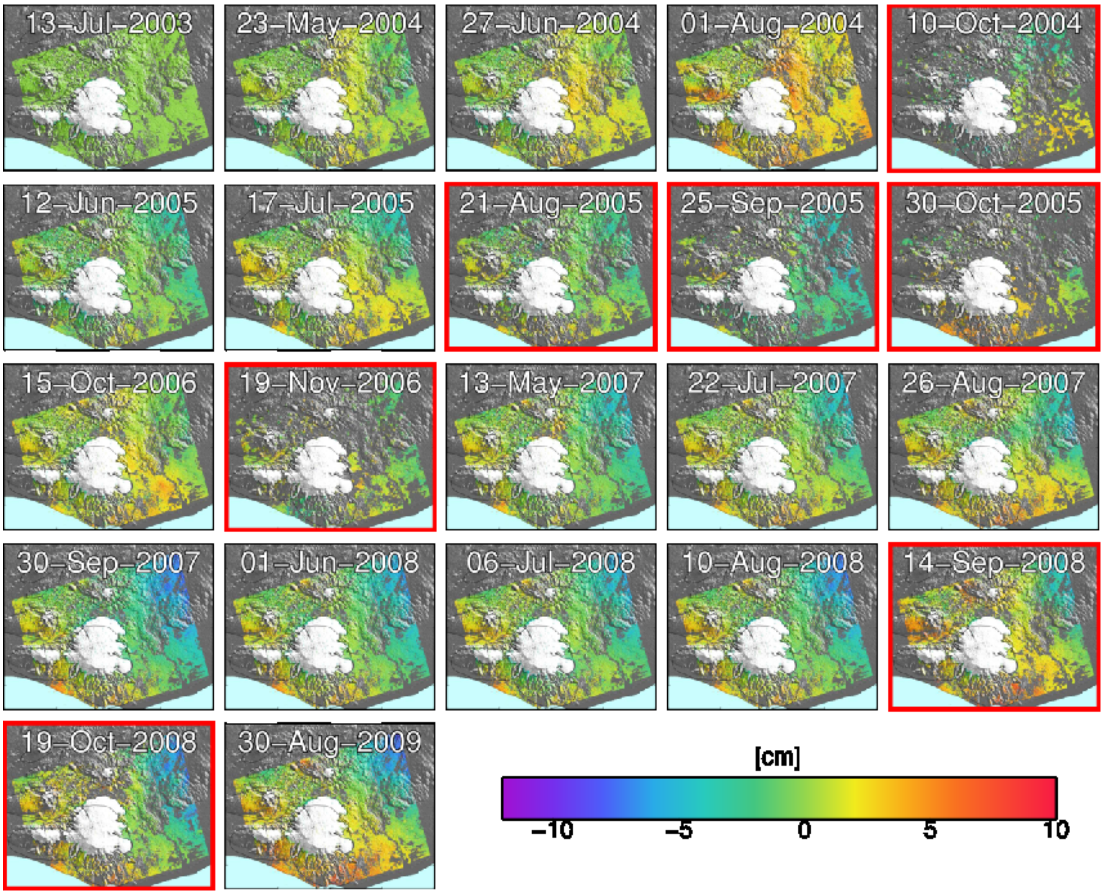

Figure 3.1: Time series of unwrapped interferograms. Each image shows the cumulative phase change with respect to the first image (July 13, 2003). The images surrounded by a red box are those identified as having lower overall coherence, due to snow or long baselines. These images are processed using the extension to StaMPS described in *Hooper et al.* (2011), and therefore only contain a subset of the points selected in the regular images. Negative phase differences indicates line of sight shortening (i.e. movement towards the satellite). The maps were created using the public domain Generic Mapping Tools software package.

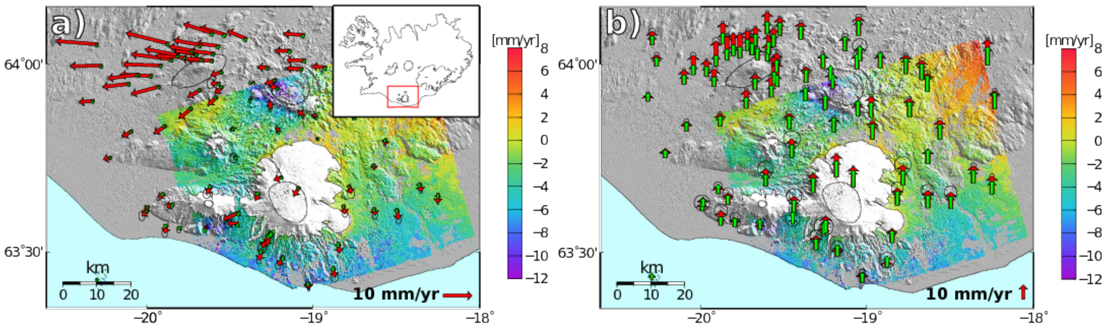

Figure 3.2: a) Horizontal and b) vertical GPS (red) and GIA model predictions (green) velocity field, plotted on the InSAR velocity. GPS velocities are relative to the ITRF08 Eurasian fixed reference frame. Positive InSAR velocities indicate movement towards the satellite. The error ellipses on the GPS give the 95 % confidence region. The inset in panel a) shows the outlines of Iceland, and the red box shows the outlines of panels a) and b). The map, including the inset, was created using the public domain Generic Mapping Tools software package.

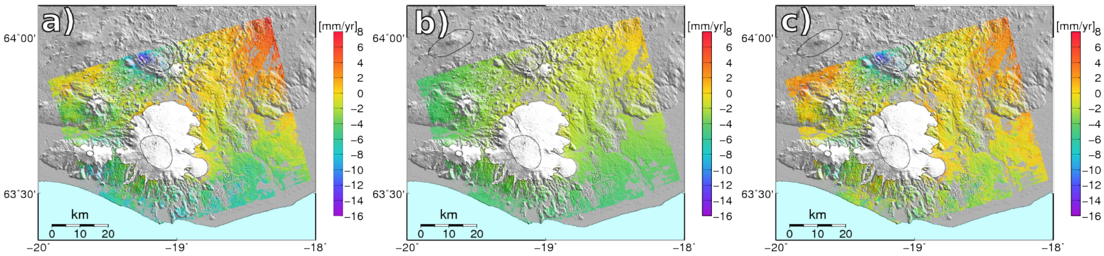

Figure 3.3: Average InSAR velocities for the period 2003-2009. a) InSAR velocities corrected for the oscillator frequency drift (See methods). b) GIA model velocities projected on the radar LOS. c) InSAR velocities corrected for local oscillator drift and GIA. The map was created using the public domain Generic Mapping Tools software package.

The GIA model underpredicts the measured velocities, especially in the horizontal components (Fig. 3.2, 3.3). The model was constrained using data in the decade before the deformation measurements used in this study. Mass balance measurements of the ice caps in Iceland have shown that after 1997, the ice caps started to lose ice at an increased rate (*Björnsson et al.*, 2013). This would have lead to an increase in GIA uplift in the years to follow (*Compton et al.*, 2015). More importantly, it has been observed in previous studies that the GIA models underpredict the magnitude of the horizontal velocity in general (*Árnadottir et al.*, 2009, *Auriac et al.*, 2013). Specifically, residual horizontal GPS velocities throughout Iceland between 1993 and 2004 are often more than twice the magnitude of the actual modelled GIA signal (*Árnadottir et al.*, 2009), consistently throughout Iceland. We therefore attribute the large residuals in the horizontal velocities around Katla to the systematic underprediction of these FEM models in the horizontal, possibly aggravated by the increased melting in recent years.

After correction for the GIA, we find no signals in the InSAR and GPS velocity fields that would indicate significant magma movements beneath the volcano. A close-up view of Katla (Fig. 3.4) shows that around the edges of some of the outlet glaciers there are increased movements in the InSAR residual velocities. As these increased movements follow the edge of individual outlet glaciers closely, they are likely due to increased melting of low altitude parts of the outlet glaciers, something not captured in the GIA model (*Schmidt et al.*, 2012). Fig. 3.4 also shows the horizontal GPS and GIA model velocities. The displacement rates at the campaign stations on the ice cap, as well as those at the continuous stations SOHO and HVOL on the south flank, agree in terms of direction with the GIA model. This suggests that the horizontal movements are most likely due to ice mass loss at the Mýrdalsjökull icecap partially covering Katla and the large Vatnajökull icecap to the east.

One of the reasons that the horizontal movements at SOHO and HVOL stations were attributed to pressure increase in the magma chamber of Katla was that a third continuous station, THEY, did not show this south-southwest ward movement. However, the inclusion of additional campaign GPS stations and the InSAR results (Fig.

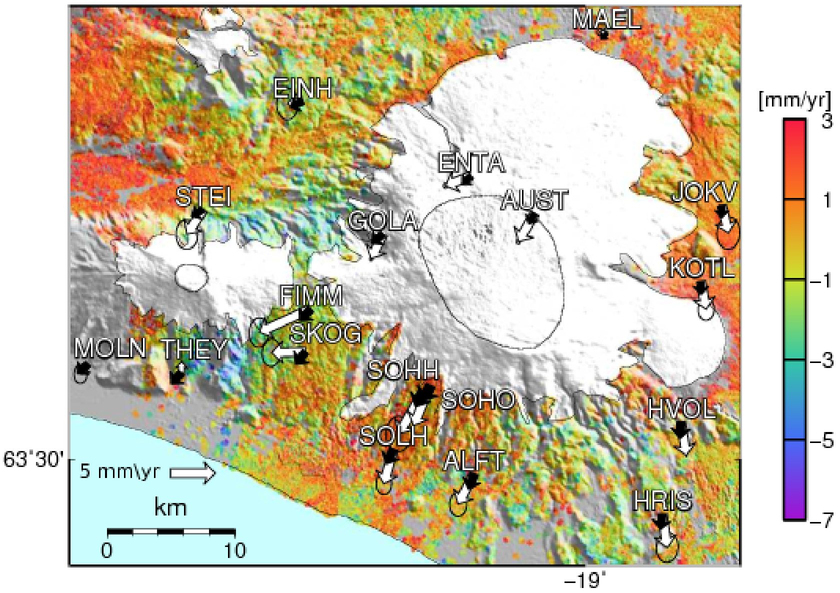

Figure 3.4: Close-up view of the Mýrdalsjökull area showing the velocity estimates of the InSAR results after the removal of the GIA model, between 2003 and 2009. Positive velocities indicate movement towards the satellite. Overlain on the InSAR velocities are the GPS velocity vectors between 2001 and 2010 in white, and the model velocity vectors in black. GPS error ellipses shows the 95 % confidence region. The map was created using the public domain Generic Mapping Tools software package.

3.4) clearly shows that in fact it was THEY, and other stations on the south flank of Eyjafjallajökull, that behaved differently to the regional trend. The horizontal GPS, vertical GPS and the InSAR velocities alike show a region of subsidence and horizontal movement towards a point on the south flank of Eyjafjallajökull. The position of this signal matches that of deformation resulting from two intrusions beneath Eyjafjallajökull in 1994 and 1999(*Pedersen and Sigmundsson*, 2004, *Hooper et al.*, 2009), suggesting cooling of the intruded lava as being the cause of this contraction signal.

To evaluate if the signal can be explained by a contraction of a sill, we have modelled it as a penny shaped crack (*Fialko et al.*, 2001). We fixed the radius and the position of the sill to closely resemble modelling results for the intrusion in 1999 (*Hooper et al.*, 2009), and varied the excess pressure (see Methods). The best fitting model is shown in Fig. 3.5. The InSAR velocities are fit remarkably well by the model, indicating that the source of the contraction is the same as, or closely related to, the 1999 intrusion. The fit to the horizontal GPS vectors is not as good. The GPS vectors are however far more sensitive to the residual GIA signal discussed above, and presumably contaminated by it.

3.3 Discussion

Pinel et al. (2007) applied an analytical model of long term ice unloading to evaluate the

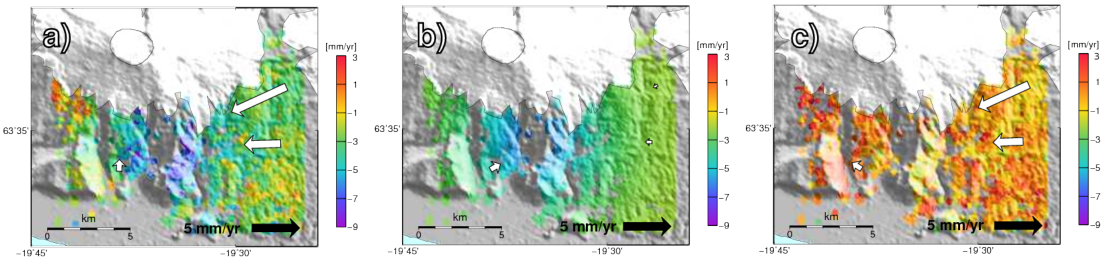

Figure 3.5: Model of the contracting signal on the south flank of Eyjafjallajökull. Panel a) shows the resampled InSAR velocity, overlain by the gps vectors in white, panel b) shows the model results projected on the radar line-of-sight, as well the horizontal model predictions in white, and panel c) shows the residual velocity after removing the model from the InSAR velocity, overlain by the residual gps vectors. The maps were created using the public domain Generic Mapping Tools software package.

effect of thinning of the Mýrdalsjökull icecap and concluded that it could not explain the observed horizontal movements at the GPS stations around Katla volcano. The influence of the ice mass loss of the larger Vatnajökull icecap was, however, neglected, while more recent visco-elastic finite element models including all ice caps show that there is in fact a significant influence from Vatnajökull in south Iceland (Fig. 3.2) (*Árnadottir et al.*, 2009, *Schmidt et al.*, 2012).

Observations of erratic behaviour at GPS sites on the caldera rim cast doubt on whether there was significant deformation resulting from pressure increase in the Katla magma chamber in the period 2000-2004. Since they became continuous in 2010, large annual variations have been observed (Fig. 3.6). Superimposed on the long term ice unloading signal, both periodic signals, due to primarily seasonal snow loading, and individual excursions can be seen. These large variations in displacement throughout the year are on the same order of magnitude as the inferred velocity changes, which means that it is difficult to identify the cause of the displacements observed in the campaign GPS measurements between 2000 and 2004, which were in the order of 2-3 cm(*Sturkell et al.*, 2008). The high frequency with which the current displacements at AUST vary means that estimated deformation rates were highly affected by the timing of the campaign measurements. Therefore, the earlier hypothesis of increased pressure in the magma chamber likely represents an over-interpretation of limited measurements in both time and space, and other processes like snow and ice unloading or water pressure variations at the base of the icecap are at least as likely to be the cause of the observed movements around Katla.

It is important to note that our results do not rule out the possibility of magma accumulation beneath Katla during the period 2001-2009. We have shown that horizontal motions at stations outside of the icecap, previously attributed to magma accumulation, are more likely to be caused by ice unloading. If there was any pressure increase in the magma chamber, significant deformation did not reach outside of the icecap, thus representing far less volume than previously inferred (*Sturkell et al.*, 2008). It is possible

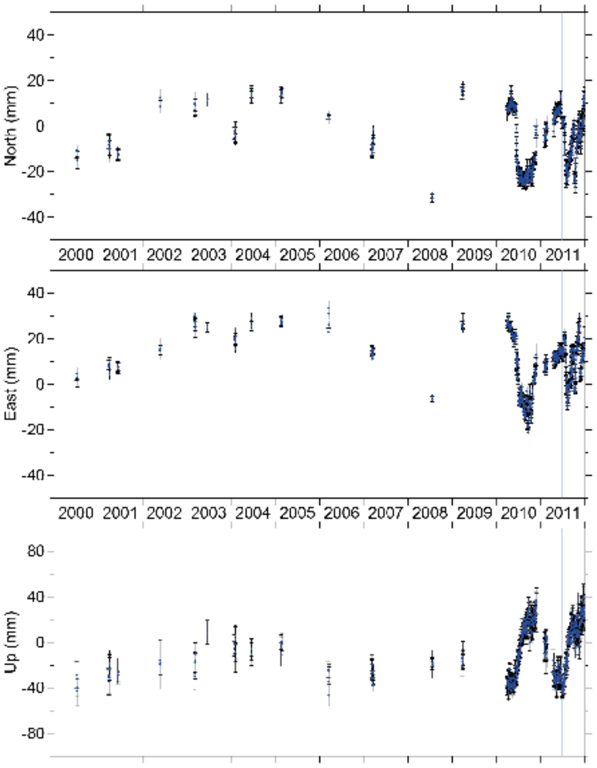

Figure 3.6: GPS time series for the Austmannsbunga station, located on the edge of the Katla caldera. The red vertical lines indicate the onset of the two eruptive events of Eyjafjallajökull in 2010, and the blue vertical line indicates the jökulhlaup at Katla in 2011. Linear trends have been removed from the time series.

that small deformations could have been obscured by the GIA signal and short term loading effects.

The contraction signal present in the InSAR velocities on the south flank of Eyjafjallajökull are fit well by a contracting penny shaped sill. The systematic horizontal discrepancy between observations and GIA models is still present in the residual horizontal GPS vectors. This explains in part the mismatch between the horizontal GPS and the model. It demonstrates the importance of evaluating the effects of long-term ice unloading when interpreting volcano deformation around ice covered volcanoes. However, the direction of the residuals do deviate from the direction predicted by the GIA model (Fig. 3.4). This could possibly be explained by a difference in geometry from the penny shaped crack model used, caused perhaps by rapid initial cooling of the edges leading to prolonged cooling of a more spheroidally shaped magma body. We cannot, however, rule out the possibility of other processes affecting the GPS observations on Eyjafjallajökull's southern flank.

Our results show that there is no significant deformation related to inflow of magma between 2001 and 2010, and therefore Katla might not be as primed to erupt as previously thought. However, as the current century long repose period is almost twice the average repose time of the volcano, and seismic activity has been high (*Tryggvason*, 1973, *Sturkell et al.*, 2008), the threat of a Katla eruption cannot be disregarded. Our results show that horizontal deformation due to GIA in Iceland is much larger than previously thought, and that this can lead to erroneous interpretations of data. It is vital to take the effect of GIA into account when interpreting future GPS data in Iceland and other glaciated areas around the world.

3.4 Methods

To form the interferograms, we used scripts from the ROI_PAC(*Rosen et al.*, 2004) and DORIS(*Kampes*, 1999) software packages. Topographic phase was removed using a 25 m posted digital elevation model from the Icelandic Geo-Survey. We used the StaMPS method to do the timeseries analysis (*Hooper*, 2008), with the extension described in (*Hooper et al.*, 2011) to minimize the loss of PS points due to low coherence images, e.g. due to snow cover.

The extension to StaMPS selects a sufficient number of interferograms of high coherence (usually summer acquisitions with low to average perpendicular baselines) to perform a reliable StaMPS PS analysis. Performing the standard StaMPS PS analysis on these high coherence interferograms results in a set of PS points. For the remaining, low coherence interferograms, each PS point is then analysed on an interferogram by interferogram basis, retaining the PS point in that interferogram only if it remains sufficiently coherent. This results in a subset of the original PS points for each low coherence interferogram. Although this yields a different set of PS points for each low coherence interferogram, all PS points are present in the higher coherence interferograms. This allows the 3D unwrapping algorithm used in StaMPS to be used with only minor adaptation.

It has long been known that Envisat images suffer from a systematic ramp (*Ketelaar*, 2009), which has recently been shown to be caused by a drift in the local oscillator frequency of the satellite (*Marinkovic and Larsen*, 2013). The linear ramp caused by this drift is removed using the following approximation, derived from an empirical study (*Marinkovic and Larsen*, 2013):

$$R = c/2 \cdot (T^{P}_{slant} - T^{Near}_{slant}) \cdot 3.87 \cdot 10^{-7}, \tag{3.1}$$

where R is the apparent ramp in m yr^{-1}, c is the speed of light, T_{slant} indicates the two way slant travel time, the superscript P indicates the current pixel and the superscript $Near$ indicates the near-range pixel.

For the GPS processing, we analysed all available campaign and continuous GPS data from south Iceland between 2001 and 2010 to estimate a velocity field for the region. We excluded all data from May 2009 within 10 km of Skógaheidi on the southeast flank of Eyjafjallajökull, due to intrusive activity leading up to the 2010 Eyjafjallajökull eruptions (*Sigmundsson et al.*, 2010). The GPS data were analyzed using the GAMIT/GLOBK version 10.4 (see T.A. Herring, R.W. King, and S.C. McClusky.*GAMIT reference manual*, **v10.4**, Massachusetts Institute of Technology, October 2010), using available International GNSS Service (IGS) 2008 absolute elevation and azimuth dependent phase center corrections for receiver antennas and ocean-loading model FES2004. We used IGS orbit and Earth orientation parameters as a-priori constraints and estimated adjustments to them during the analysis as well as estimating daily coordinates for the GPS sites. We analyzed the data with a set of 150 selected global reference stations and used GLOBK to estimate the velocity field in a fixed ITRF08-Eurasia reference frame (*Altamimi et al.*, 2011).

We modelled the contraction signal south of Eyjafjallajökull as a penny shaped crack (*Fialko et al.*, 2001). We fixed the center of the crack to -19.58 longitude and 63.58 latitude, at a depth of 5.7 km and a radius of 2.5 km. We varied the excess pressure drop between $1 \cdot 10^4$ and $5 \cdot 10^5$ Pa. We evaluated the best fitting model compared to the residual InSAR velocities based on the residual sum of squares, weighted by the inverse of the covariance matrix. The best fit model had an excess pressure drop of $3.2 \cdot 10^5$ Pa.

Acknowledgements

We thank P. Schmidt and B. Lund for providing their glacial isostatic adjustment model results. Envisat data were provided by the European Space Agency. Some figures were prepared using the public domain GMT software. The continuous GPS network in Ice-

land is maintained by the Icelandic Meteorological Office in collaboration with the University of Iceland. Campaign GPS data has been collected by the University of Iceland and Penn State University. GPS station AUST is operated as part of the European Commissions's Seventh Framework Programme Grant No. 308377 (Project FUTUREVOLC) and the Icelandic Research Fund No 110242011 (Project Volcano Anatomy).

References

Altamimi, Z., X. Collilieux, and L. Métivier (2011), ITRF2008: an improved solution of the internation terrestrial reference frame, *J. Geod.*, *85*, 457–473, doi:10.1007/s00190-011-0444-4. 3.4

Árnadottir, T., B. Lund, W. Jiang, H. Geirsson, H. Björnsson, P. Einarsson, and T. Sigurdsson (2009), Glacial rebound and plate spreading: results from the first countrywide GPS observations in Iceland, *Geophys. J. Int.*, *177*(2), 691–716, doi:10.1111/j.1365-246X.2008.04059.x. 3.1, 3.2, 3.2, 3.3

Auriac, A., K. Spaans, F. Sigmundsson, A. Hooper, P. Schmidt, and B. Lund (2013), Iceland rising: Solid Earth response to ice retreat inferred from satellite radar interferometry and visocelastic modeling, *J. Geophys. Res. Solid Earth*, *118*, 1331–1344, doi:10.1002/jgrb.50082. 3.1, 3.2

Björnsson, H. (1978), The surface area of glaciers in Iceland, *Jökull*, *28*. 3.1

Björnsson, H., F. Pálsson, S. Gudmundsson, E. Magnússon, G. Adalgeirsdóttir, T. Jóhannesson, E. Berthier, O. Sigurdsson, and T. Thorsteinsson (2013), Contribution of Icelandic ice caps to sea level rise: Trends and variability since the Little Ice Age, *Geophys. Res. Let.*, *40*, 1–5, doi:10.1002/grl.50278. 3.1, 3.2

Compton, K., R. Bennett, and S. Hreinsdóttir (2015), Climate driven vertical acceleration of Icelandic crust measured by CGPS geodesy, *Geophys J Int*, *42*, online. 3.2

Fialko, Y., Y. Khazan, and M. Simons (2001), Deformation due to a pressurized horizontal circular crack in an elastic half-space, with applications to volcano geodesy, *Geophys. J. Int.*, *146*, 181–190. 3.2, 3.4

Geirsson, H., T. Árnadóttir, S. Hreinsdóttir, J. Decriem, P. Lafemina, S. Jonsson, R. Bennett, S. Metzger, A. Holland, E. Sturkell, T. Villemin, C. Volksen, F. Sigmundsson, P. Einarsson, M. Roberts, and H. Sveinbjornson (2010), Overview of results from continuous GPS observations in Iceland from 1995 to 2010, *Jökull*, *60*, 3–22. 3.2

Geirsson, H., P. LaFemina, T. Árnadóttir, E. Sturkell, F. Sigmundsson, M. Travis, P. Schmidt, B. Lund, S. Hreinsdóttir, and R. Bennett (2012), Volcano deformation at active plate boundaries: Deep magma accumulation at Hekla volcano and plate boundary deformation in south Iceland, *J. Geophys. Res.*, *117*(No. B11), B11,409. 3.2

Gudmundsson, O., B. Brandsdóttir, W. Menke, and G. Sigvaldason (1994), The crustal magma chamber of the Katla volcano in South Iceland revealed by 2-d seismic undershooting, *Geoph J Int*, *119*, 277–296, doi:10.1111/j.1365-246X.1994.tb00928.x. 3.1

Hooper, A. (2008), A multi-temporal InSAR method incorporating both persistent scatterer and small baseline approaches, *Geophys Res Lett*, *35*(16), doi:10.1029/2008GL034654. 3.2, 3.4

Hooper, A., R. Pedersen, and F. Sigmundsson (2009), Constraints on Magma intrusion at Eyjafjallajökull and Katla Volcanoes in iceland, from time series sar interferometry, *The VOLUME Project, Volcanoes: Understanding subsurface mass movement*, pp. 13–24. 3.1, 3.2

Hooper, A., D. Bekaert, K. Spaans, and M. Arıkan (2011), Recent advances in SAR interferometry time series analysis for measuring crustal deformation, *Tectonophysics*, *514-517*, 1–13, doi:10.1016/j.tecto.2011.10.013. 3.2, 3.1, 3.4

Kampes, B. (1999), *Delft Object-oriented Radar Interferometric Software: User's manual and technical documentation*, v4.02 ed. 3.4

Ketelaar, V. (2009), Satellite radar interferometry: Subsidence monitoring techniques, Ph.D. thesis, Delft University of Technology, The Netherlands, doi:10.1007/978-1-4020-9428-6. 3.4

Larsen, G. (2000), Holocene eruptions within the Katla volcanic system, south Iceland: Characteristics and environmental impact, *Jökull*, *49*, 1–28. 3.1

Larsen, G., A. Dugmore, and A. Newton (1999), Geochemistry of historical-age silicic tephras in Iceland, *The Holoscene*, *9*(4), 463–471, doi:10.1191/095968399669624108. 3.1

Marinkovic, P., and Y. Larsen (2013), Consequences of long-term ASAR local oscillator frequency decay - an empirical study of 10 years of data, *Living Planet Symposium*. 3.4

Pedersen, R., and F. Sigmundsson (2004), InSAR based sill model links spatially offset areas of deformation and seismicity for the 1994 unrest episode at Eyjafjallajökull volcano, Iceland, *Geophys. Res. Lett.*, *31*, doi:10.1029/2004GL020368. 3.1, 3.2

Pinel, V., F. Sigmundsson, E. Sturkell, H. Geirsson, P. Einarsson, M. T. Gudmundsson, and T. Högnadóttir (2007), Discriminating volcano deformation due to magma movements and variable surface loads: application to Katla subglacial volcano, Iceland, *Geophys J Int*, *169*(1), 325, doi:10.1111/j.1365-246X.2006.03267.x. 3.1, 3.3

Rist, S. (1967), Jökulhlaups from the ice cover of Mýrdalsjökull on June 25, 1955 and January 20, 1956., *Jökull*, *17*, 243–248. 3.1

Rosen, P., S. Henley, G. Peltzer, and M. Simons (2004), Updated repeat orbit interferometry package released, *EOS Trans Am Geophys Union*, *85*(5), 47, doi:10.1029/2004EO050004. 3.4

Schmidt, P., B. Lund, T. Árnardóttir, and H. Schmeling (2012), Glacial isostatic adjustment constrains dehydration stiffening beneath Iceland, *Earth Planet Sc Lett*, *359-360*, 152–161, doi:10.1016/j.epsl.2012.10.015. 3.1, 3.2, 3.2, 3.3

Sigmundsson, F., S. Hreinsdóttir, A. Hooper, T. Árnadóttir, R. Pedersen, M. Roberts, N. Óskarsson, A. Auriac, J. Decriem, P. Einarsson, H. Geirsson, M. Hensch, B. Ófeigsson, E. Sturkell, H. Sveinbjörnsson, and K. Feigl (2010), Intrusion triggering of the 2010 Eyjafjallajökull explosive eruption, *Nature*, *468*(7322), 426, doi:10.1038/nature09558. 3.1, 3.4

Sigurdsson, O., S. Zóphóníasson, and E. Ísleifsson (2000), Jökulhlaupúr Sólheimajökli 18. júlí 1999 (The jökulhlaup from Sólheimajökull July 18, 1999, in Icelandic with English summary), *Jökull*, *49*, 75–80. 3.1

Sturkell, E., P. Einarsson, F. Sigmundsson, H. Geirsson, H. Ólafsson, R. Pedersen, E. De Zeeuw-Van Dalfsen, A. Linde, S. Sacks, and R. Stefansson (2006), Volcano geodesy and magma dynamics in Iceland, *J Volcanol Geoth Res*, *150*(1-3), 14, doi:10.1016/j.jvolgeores.2005.07.010. 3.1

Sturkell, E., P. Einarsson, M. Roberts, H. Geirsson, M. Gudmundsson, F. Sigmundsson, V. Pinel, G. Gudmundsson, H. Olafsson, and R. Stefansson (2008), Seismic and geodetic insights into magma accumulation at Katla subglacial volcano, Iceland: 1999 to 2005, *J Geophys Res-Sol Ea*, *113*(B3), B03,212, doi:10.1029/2006JB004851. 3.1, 3.2, 3.3, 3.3

Sturkell, E., P. Einarsson, F. Sigmundsson, A. Hooper, B. Ófeigsson, H. Geirsson, and H. Ólafsson (2009), Katla and Eyjafjallajökull Volcanoes, *Developments in Quaternary Science*, *13*, 5–21. 3.1, 3.2

Tómasson, H. (1996), The jökulhlaup from Katla in 1918, *Annals of Glaciology*, *22*, 249–254. 3.1

Tryggvason, E. (1973), Seismicity, earthquake swarms, and plate boundaries in the Iceland region, *Bulletin of the Seismological Society of America*, *63*(4), 1327–1348. 3.1, 3.3

Chapter 4

Constraints on the crustal stress field from the 2014 Bárðarbunga rifting event

Karsten Spaans[1] and Andrew Hooper[1]

[1] *COMET, School of Earth and Environment, University of Leeds, United Kingdom*

Abstract

The two week long rifting event at Bárðarbunga Volcano in 2014 led to the Holuhraun eruption, which produced 1.5 km^3 of lava and was the largest in the country in over 200 years. Predicting when and where an intrusion will lead to eruption requires detailed knowledge of the underlying stress field. Previous studies have explained the dike propagation path with a model that includes a deviatioric stress field set up by a uniform amount of plate spreading about a straight rift axis. Here, we test this hypothesis by modelling the tractions acting on the dike walls, constrained by data from GNSS and InSAR. Our results show that the majority of the opening and shearing in the final dike segment is due to plate spreading, as expected, but that the same model of plate spreading cannot explain the movement of the dike walls further south. This result implies that either the rift axis is not straight in this region, or that most of the deviatoric stress has been released beneath the ice cap. The latter option suggests that intrusions associated with the volcano, and the nearby Grímsvötn volcano, most of which could have been undetected due to the subglacial nature of the systems, might have released most of the stress in the area resulting from plate spreading, while the stress on the less volcanically active part of the rift further north has been mostly released during the 2014 episode. Modelling of the 2014 Bárðarbunga rifting event therefore not only provided insights into what happened in the present, but also allowed us a glimpse into

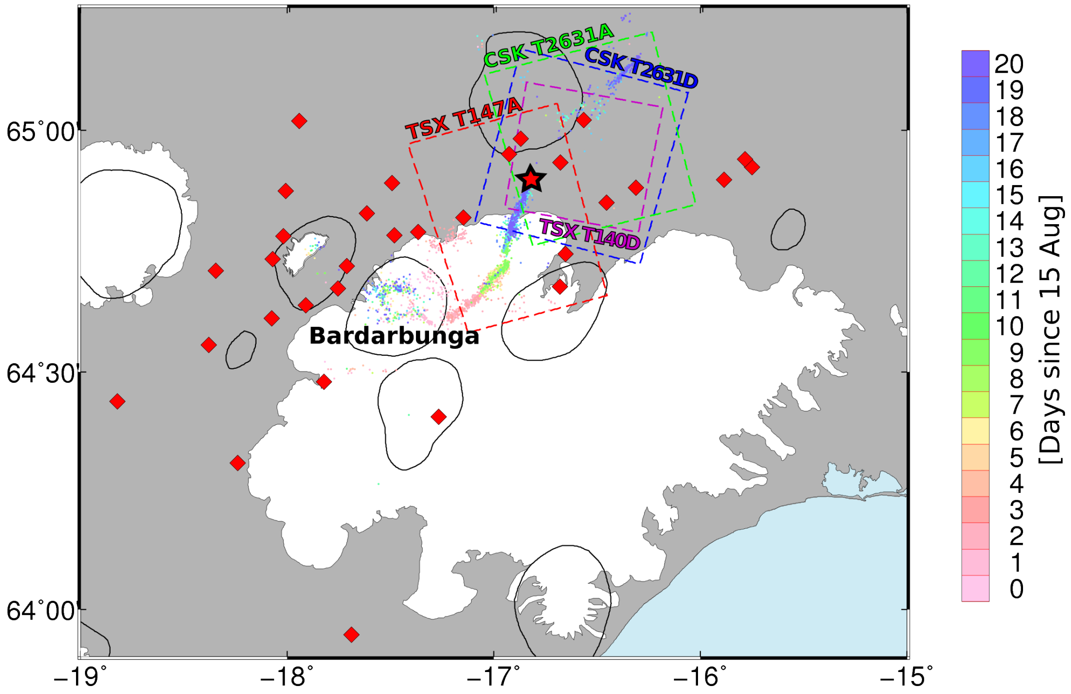

Figure 4.1: Map of the Vatnajökull area. Red diamonds indicate the location of GNSS stations used in this study. The dashed boxes give the outline of the InSAR scenes. The white areas are ice caps, and the circular outlines give the location of central volcanoes in the area. The red star gives the location of the main fissure. The coloured dots shows the locations of relocated earthquakes in the period Aug 15 to Sep 4, 2015, as published in *Sigmundsson* et al. (2015). The colour of each dot represents the day of the earthquake.

the volcanic system's past.

4.1 Introduction

The subglacial Bárðarbunga Volcano in Iceland lies beneath the Vatnajökull ice cap (4.1). The associated volcanic system consists of a central volcano, a caldera and a fissure swarm, which extends to the south-southwest and north-northeast for a total length of 170 km. Bárðarbunga has had 23 confirmed eruptions since the settlement of Iceland 1,100 years ago (*Thordarson and Larsen*, 2007). It also produced the largest Holocene lava flow in the world by both volume and area, the Þjórsá lava field, which was erupted around 8600 years BP (*Hjartarson*, 2003).

The 2014 Holuhraun rifting episode began with a seismic swarm on August 16th (*Sigmundsson* et al., 2015). Seismic activity and GNSS observations showed a dike moving initially radially away from the caldera towards the east-southeast, and then turning towards the north-northeast (*Sigmundsson* et al., 2015), see seismicity in Fig. 4.1. Dike progress continued for 20 km until the 19th of August, after which propagation stopped for 80 hours. On the 23rd of August, the dike briefly turned left to propagate in a north-northwesterly direction. The final change of direction left the dike to propagate in a north-northeasterly direction, in which it continued until the 27th of August, with the tip of the dike located approximately 10 km north of the Vatnajökull ice cap. The diking event was accompanied by significant subsidence of the caldera of tens of meters in the first few weeks after the onset of the eruption, showing subsidence rates exceeding 50 cm per day (*Riel et al.*, 2015, *Gudmundsson et al.*, 2016).

The first of two eruptive events commenced on the 29th of August, a minor event lasting only 4 hours. On the 30th of August, a second event started from the same fissure, which continued to erupt for several months, until February 2015. The eruptive fissure is located in the older Holuhraun lava field, which is thought to have been emplaced sometime between 1794 and 1864 (*Hartley and Thordarson*, 2013). From this fissure, a lava field developed that covered 85 km^2 by the end of the 2014/2015 eruption, and contains approximately 1.5 km^3 of lava, making it the largest eruption in Iceland in over 200 years (*Schmidt et al.*, 2015).

Here we use stress driven boundary element modelling to constrain GNSS and InSAR measurements of the dike propagation and the early stages of the eruptive event. We model several time steps, starting the day before the onset of the event on the 16th of August, 2014 until the 4th of September, when the dike had finished its migration northwards and the fissure eruption had been ongoing for several days. Our modelling reveals the nature of the deviatoric stress field due to plate spreading and the evolution of overpressure in the dike through time, as well as the spatial distribution of opening and shearing across the dike.

4.2 Deformation observations

The deformation associated with the dike propagation was observed using a network of continuous and campaign GNSS stations (*Sigmundsson* et al., 2015) and four Interferometric Synthetic Aperture Radar (InSAR) scenes. We used the GNSS data presented in *Sigmundsson* et al. (2015), which comprises 31 GNSS stations processed using the GAMIT/GLOBK software (*Herring et al.*, 2010), version 10.4.

The InSAR data comprises of two Cosmo-SkyMed images, namely descending track 2631 (13 Aug 2014 – 29 Aug 2014) and ascending track 2631 (30 Jul 2014 – 1 Sep 2014), and two TerraSAR-X scenes, descending track 140 (13 Aug 2014 – 4 Sep 2014) and ascending track 147 (26 Jul 2012 – 4 Sep 2014). The descending Cosmo-SkyMed track and the ascending TerraSAR-X track were also used to constrain the models presented in *Sigmundsson* et al. (2015), but the other two tracks were not. All interferograms were coregistered and interfered using the Doris software package (*Kampes*, 1999). For Cosmo-SkyMed descending track 2631, a large time series of interferograms was available, allowing us to estimate the coherence using the RapidSAR method (*Spaans and Hooper*, 2016). For the other three interferograms, we used the boxcar method (*Just and Bamler*, 1994) with a window size of 11 by 11 to estimate the coherence. We estimated and removed the spatially correlated part of the phase from all four interferograms prior to coherence estimation to avoid the high frequency deformation fringes biasing the estimation (*Spaans and Hooper*, 2016). The spatially correlated phase estimation was achieved using multilook filtering. The wrapped phase values of points with sufficient coherence were unwrapped using the Snaphu software (*Chen and Zebker*, 2001). To reduce the amount of data for modelling, we applied adaptive quadtree resampling to downsample the unwrapped interferograms (*Decriem et al.*, 2010). The left column in Fig. 4.2 shows the unwrapped, downsampled interferograms.

The interferograms each cover slightly different periods. The master date of all interferograms is before the onset of the event on the 16th of August and we assume there is no significant relative deformation in the area between the master date of each interferogram and the onset of the unrest. The slave dates of the interferograms range from the 29th of August to the 4th of September, and a similar assumption can not be made here, as significant deformation associated with dike emplacement continued until the 4th of September (*Sigmundsson* et al., 2015). To address this, we define five overlapping time intervals, where each subsequent time period is between 3 and 5 days longer than the previous one. The time periods all start on the 15th of August, and they end on the 19th of August, 24th of August, 29th of August, 1st of September and 4th of September, respectively. The black arrows in Fig. 4.3 show the available GNSS deformation vectors in the vicinity of the eruptive site for each of the five intervals. A handful of GNSS stations that are shown in Fig. 4.1 fall outside of the area covered in Fig. 4.3. These stations are however included to constrain the modelling described below, and all show no significant movements. The slave dates of the interferograms coincide with three of the time intervals. Thus we can constrain models of the deformation in the first two intervals by GNSS measurements alone, and the last three periods by a combination of GNSS and InSAR measurements.

4.3 Boundary element modeling

We used a boundary-element approach to model the InSAR and GPS observations. Our model is based on the method described in *Hooper et al.* (2011). We initially assume four dike segments, as defined in the modeling of *Sigmundsson* et al. (2015). We further assume that the four dike segments are at a depth of constant mean pressure, i.e. the mean pressure does not vary along the dike. Initially, we solve for a deviatoric stress resulting from plate spreading, and for the magma overpressure in the dike for each of the five time intervals. Magma overpressure is the difference between the magma pressure and the mean pressure, as opposed to the excess pressure acting on the dike walls, i.e. magma pressure does no include the deviatoric stress (*Segall*, 2009). The

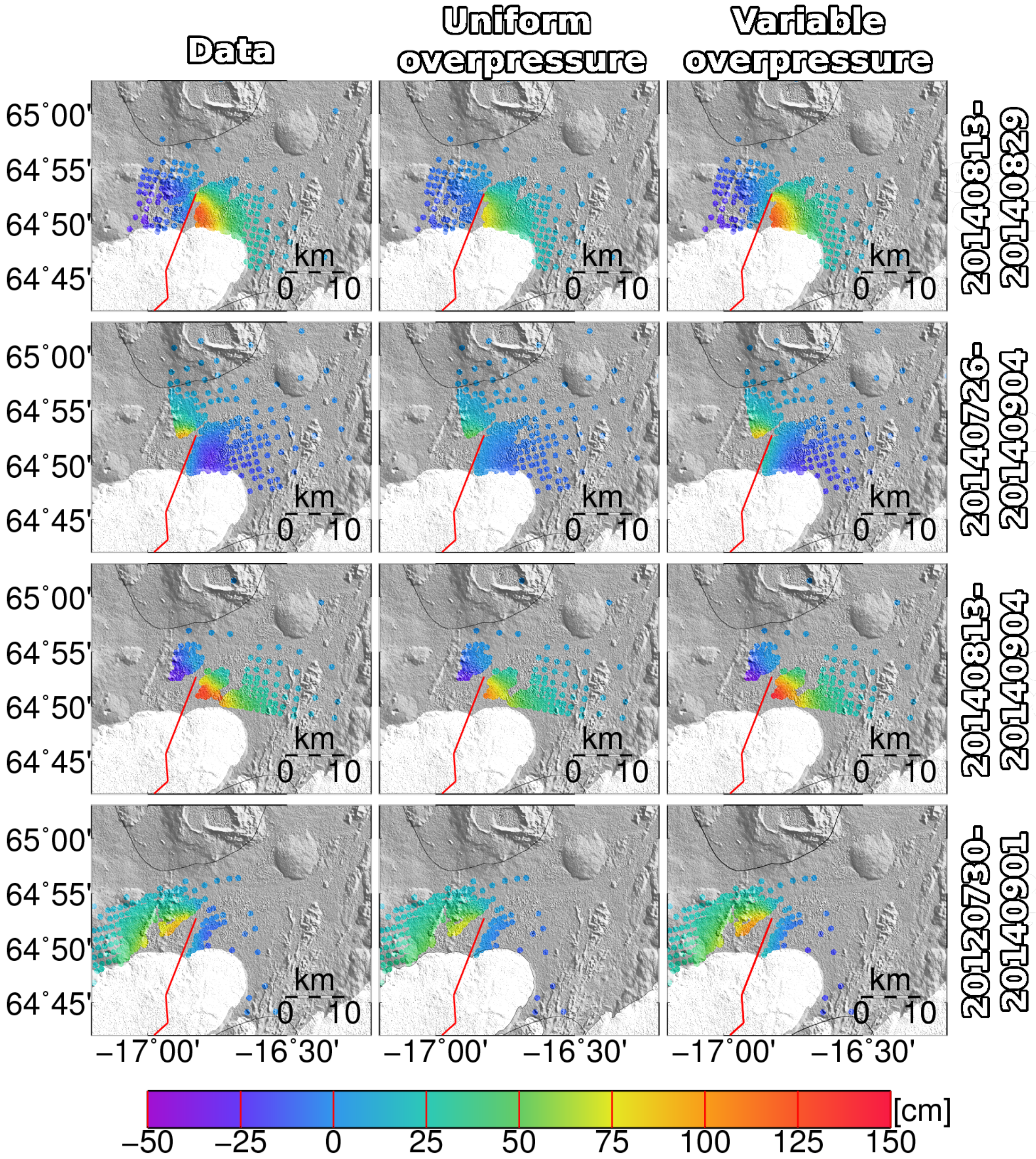

Figure 4.2: Interferograms covering the eruption. The left column shows the unwrapped phase values of the four interferograms 20140813-20140829 (first row), 20140730-20140901 (second row), 20140813-20140904 (third row) and 20120726-20140904 (fourth row). The second column shows the uniform overpressure model prediction converted to the radar LOS, and the third column shows the variable overpressure (i.e. increased overpressure in the final dike segment) model predictions converted to the radar LOS. Positive displacements are displacements towards the satellite. White area in the background is area covered by the ice cap. The red trace shows the path of the dike in the model.

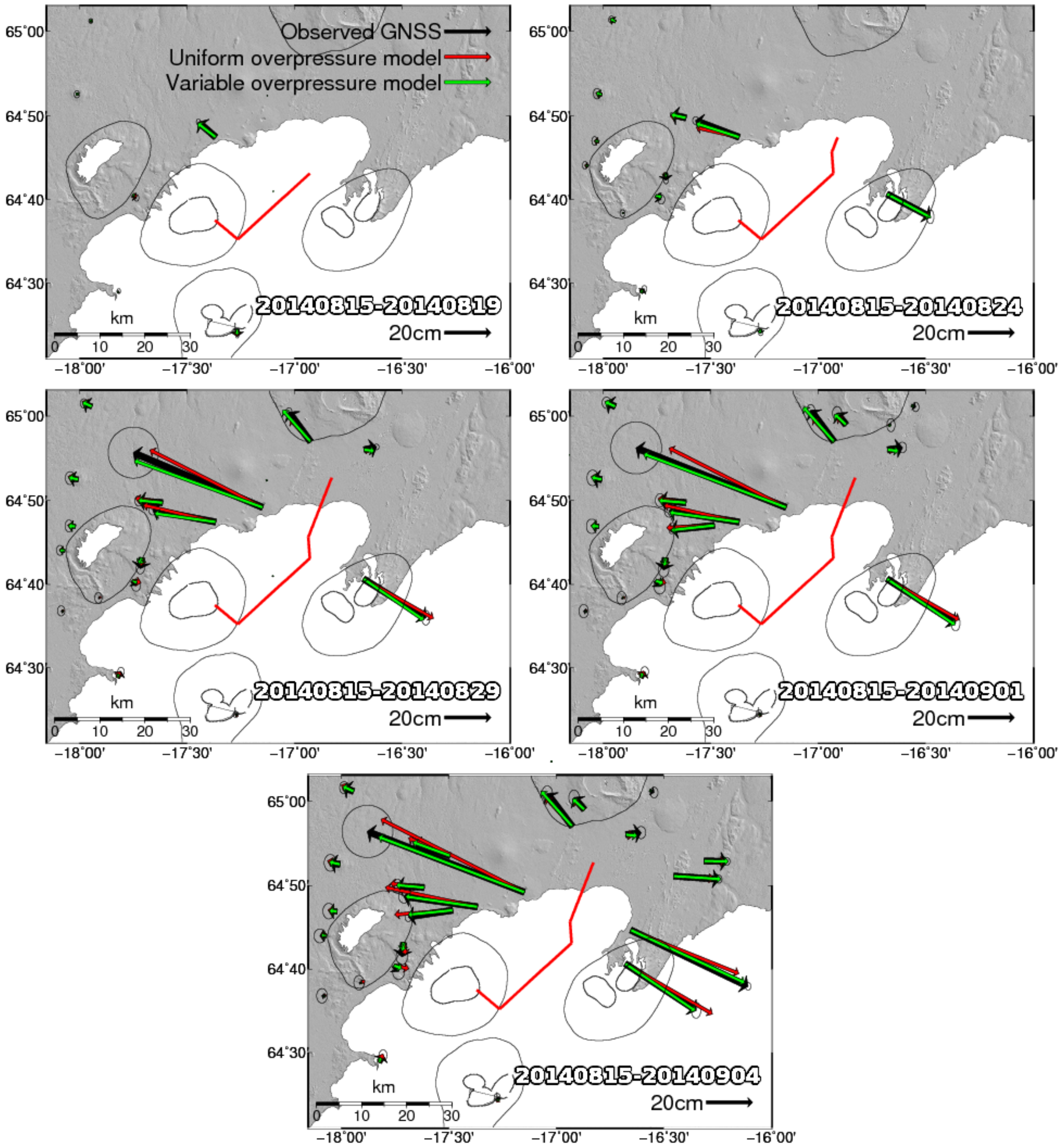

Figure 4.3: GNSS measured displacement vectors (black arrows) during the periods 15/08-19/08 (top left), 15/08-24/08 (top right), 15/08-29/08 (middle left), 15/08-01/09 (middle right) and 15/08-04/09 (bottom), as published in (*Sigmundsson* et al., 2015). The circles indicate the 95% confidence region. Also displayed are the MAP model predictions for the uniform overpressure (red arrows) and the variable overpressure models (green arrows). The red trace shows the path of the dike used in the modelling.

excess pressure can be written as:

$$p_e = p_m - \sigma_n, \tag{4.1}$$

where p_e is the excess pressure acting on the dike walls, p_m is the magma pressure, and σ_n is the stress acting in the normal direction to the dike walls. The magma overpressure can be written as:

$$p_o = p_m - p_{mean}, \tag{4.2}$$

where p_o is the magma overpressure and p_{mean} is the mean pressure in the rock.

We use Okada fault patches (*Okada*, 1992) to calculate the stress mapping functions, which assumes a flat earth geometry, homogeneous elastic half space and infinitesimal strain. We account for the caldera subsidence by including a contracting Mogi source (*Mogi*, 1958) at fixed location and depth based on that resolved in *Sigmundsson* et al. (2015), and solving for the volume change, the depth of the dike, and depth extent of the dike. Note, we are not attempting to determine the stresses acting on the magma chamber with this approach, but are instead accounting for the contribution of the magma chamber to the deformation. Thus, we do not consider the interaction of stress between the magma chamber and dike, although we recognise there will be a small influence on dike opening from the magma chamber depressurisation that we ignore.

The deviatoric stress due to plate spreading is dependent on the distance from the central rift axis. The central axis of plate spreading has been found to go through the center of the Askja caldera (*Sturkell and Sigmundsson*, 2000), just north of the fissure location, and strikes at an angle of approximately 15 degrees (*Heimisson et al.*, 2015). This would place the northern most segments of the dike closest to the rift, increasing the influence of the plate spreading on the stress field. We use the arctangent model proposed by *Heimisson et al.* (2015) to model the displacement due to plate spreading:

$$u(d) = \frac{U}{\pi} \arctan\left(\frac{d}{D}\right), \tag{4.3}$$

where $u(d)$ is the displacement due to plate spreading as a function of distance from the rift, U is the far field plate separation and D is parameter related to the locking depth. We use a value of 6500 m for D, as was found for the same area by (*Heimisson et al.*, 2015). We take the derivative of Eq. 4.3 with respect to d to obtain the strain as a function of distance from the rift, and assume a value of 75 GPa for the Young's modulus, as was found in *Auriac et al.* (2014), to calculate the resulting stress using Hooke's law. We solve for the far field separation parameter U in our modeling.

We assumed the measurement errors for both the GPS and the InSAR were drawn for a multivariate Gaussian distribution. For the InSAR measurements, we assumed a 1D exponential covariance function with a sill of 15 mm^2, a nugget of 5 mm^2 and a range of 20 km (*Sigmundsson* et al., 2015). We sampled the *a posteriori* probability distribution (MAP) using a Markov Chain Monte Carlo sampling algorithm (*Mosegaard and Tarantola*, 1995). In this approach initial values are chosen for the model parameters, and the likelihood function is calculated. A trial model is selected by taking a random step for all modelling parameters, and the likelihood of the trial model is compared to the initial model. The trial model is accepted if it fulfills one of two conditions: 1) The likelihood of the trial model is higher than the current model, or 2) The ratio of the trial model likelihood and the current model likelihood is greater than a random number chosen between 0 and 1. If accepted, the trial model becomes the current model, and a new trial model is selected by taking a random step from this model. If rejected, the random step is taken from the previous model. This is continued until a representative sampling of the probability distribution is obtained. To ensure fast convergence, we perform a sensitivity test every 500 trial models to set the maximum step size for each model parameters. We ensure that all model parameters contribute approximately equally to the change in likelihood, and that approximately half the trial models are accepted (*Hooper et al.*, 2013).

For our initial model, we assumed uniform overpressure in the dike, and solved for 13 model parameters: the far field separation due to plate spreading, five overpressures and five mogi volume changes (one for each time period), and finally the depth and depth extent of the dike. The red arrows in Fig. 4.3 show the MAP GNSS model predictions for the model described above with uniform magma overpressure in the entire dike. This model provides a reasonably good fit for the GNSS observations. The LOS displacements vectors predicted by the MAP model are shown in the second column of Fig 4.2. Even though the far field displacements measured by GNSS are fairly well predicted by the model, the InSAR near-field displacements are clearly underpredicted. This underprediction is also present for some of the GNSS stations that are close to the tip of the dike, where predicted vectors point too far northwards, suggesting a lack of model opening in the tip of the dike.

To create additional opening in the tip of the dike, additional stress is required. This can either come from variations in the deviatoric stress field, or from additional magma overpressure inside the dike. Decreased topography along the propagation path can be expected to increase overpressure, either due to decreasing lithosotatic pressure, for a dike at a fixed depth with respect to sea level, or decreasing magmastatic head for a dike that remains at a depth of constant mean pressure. To test if this could generate the additional opening required in the tip of the dike, we separate the depth of the final dike segment from the depth of the other three, solving for them both. We assume that additional overpressure is generated either by reduced topography above the dike which stays at constant depth with respect to sea level, or by the dike moving with the reduced topography, which lowers the magmastatic head the magma has to overcome. In both cases, the overpressure is proportional to the density, of the rock and magma, respectively. We assume a mean pressure gradient of 25 kPa/m, corresponding to a density of approximately 2500 kg/m^3. This increases the number of parameters to solve for by one (the depth difference between the final segment and the remainder of the dike), bringing the total to 14 for this variable overpressure model.

The predicted GNSS deformation vectors for the variable overpressure model are shown by the green arrows in Fig. 4.3, and the predicted LOS InSAR deformation for the four interferograms is shown in the third column of Fig. 4.2. The fit of the variable overpressure model predictions for both the GNSS and the InSAR deformation measurements is much improved compared to the standard model, especially for the InSAR data. The predicted depth of the final dike segment is 206^{221}_{194} m below the surface, and the depth of the other three segments is 620^{660}_{600} m. In these values, and subsequent values like it, the normal scripted number is the MAP value prediction, and the super- and subscript values represent the 95% probability range. The predicted extent of the dike in depth is 5710^{5760}_{5600}.

The time evolution of the magma overpressure is displayed in Fig. 4.4. For the uniform overpressure model (Fig. 4.4a), the overpressure continues to increase over time, albeit at a slower rate, reaching a maximum of of just below 10 MPa. For the variable overpressure model (Fig. 4.4b), the magma overpressure seems to flatten off after the 24th of August at around 8 MPa. This flattening might be expected once the dike stops propagating, and the flow reaches a steady state. In the final dike segment, however, the magma overpressure rises to almost 19 MPa for the variable overpressure model. This value is very high, and likely higher than the host rock can sustain without propagating further. Furthermore, the far field separation due to plate spreading for the variable overpressure model is only $0.47^{0.65}_{0.26}$ m, resulting in almost no strike-slip motion on the final dike segment. This contradicts observations on the ground (*Hjartardóttir et al.*, 2015), previous modelling results(*Sigmundsson* et al., 2015), InSAR offset tracking results (*Jónsson et al.*, 2016) and focal mechanisms (*Ágústdóttir et al.*, 2016), all of which indicate significant strike-slip motion on the fault.

The variable overpressure model shows that the deformation measurements can be fit well by creating additional opening in the tip of the dike. However, the very large magma overpressure required to do this and the lack of strike-slip motion that this model predicts makes the model less plausible. The additional opening therefore likely comes predominantly from the deviatoric stress field. We explore this option further by imposing a large far field separation. We set the far field separation (U in Eq. 4.3) to 2 m, and shift the rift axis to line up with the final dike segment to maximize the relative influence of the deviatoric stress field on this segment. The red arrows in Fig. 4.5 show the model predictions for the GNSS vectors for this model. The effect of the shearing of the dike along most of its length is clearly visible in the vectors closest to the dike. The left-lateral strike-slip motion on the dike rotates the deformation vectors to the west of the dike southward, and deformation vectors to the east of the dike northward, leading to an overall poor fit. Furthermore, the InSAR LOS deformation predictions (Fig. 4.6,

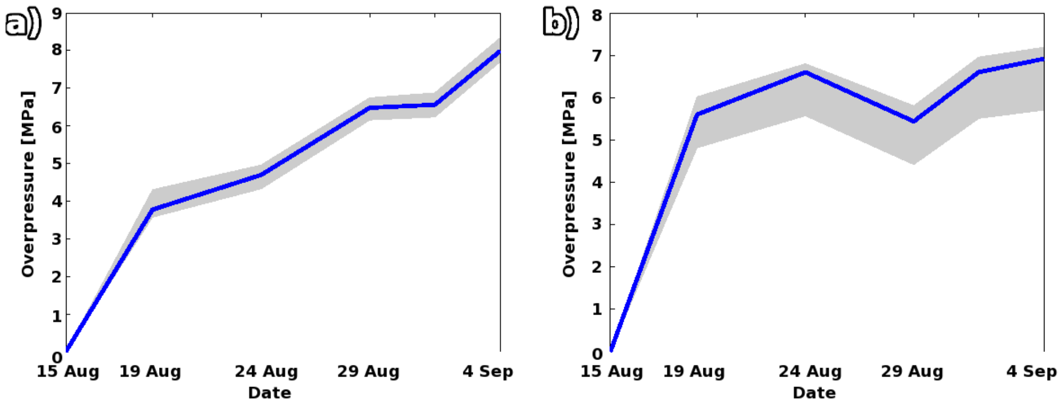

Figure 4.4: Magma overpressure predicted by a) uniform overpressure and b) variable overpressure models. The blue lines indicate the MAP model. The gray area indicates the 95% probability range of model realisations. For the variable overpressure model, it is the magma overpressure in the early, deeper segments that is plotted.

middle column) still underpredict the observed values.

Given that a deviatoric stress field due to uniform plate spreading, even with its position optimized for the final dike segment, cannot explain the deformations observed, we therefore hypothesize that the deviatoric stress field must vary along the dike. The rift axis is well constrained by GNSS in the Askja area, just north of the Holuhraun fissure (*Sturkell and Sigmundsson*, 2000). As mentioned above, ground observations of shearing of the graben, and strike-slip focal mechanisms at the tip of the dike suggest that the deviatoric stress field at the tip of the dike largely follows this direction. However, further south there are fewer GNSS observations. The magnitude and direction of the stress field could be very different here. We investigate this possibility by applying the deviatoric stress field only on the final dike segment, and assuming only opening caused by the magma overpressure on the early dike segments. We fix the position of the rift axis to the original location, and solve for the far field separation parameter of the arctangent model. The green arrows in Fig. 4.5 show the model predictions for the GNSS vectors for the variable far field separation model, and the right column of Fig. 4.6 shows the InSAR LOS predictions for this model. Even with a simplified representation of what is likely a more complicated stress field, the model is able to fit the measurements well.

Fig. 4.7 shows the maximum likelihood opening predicted for each patch during the five time periods for the variable far field separation model. The maximum opening is just over 4 m, in the final segment of the dike. The maximum strike-slip motion predicted is 0.8 m. Our model predicts a far field separation of $2.7_{2.6}^{2.9}$ m. The magma overpressure and volume contained in the dike are shown in Fig. 4.8.

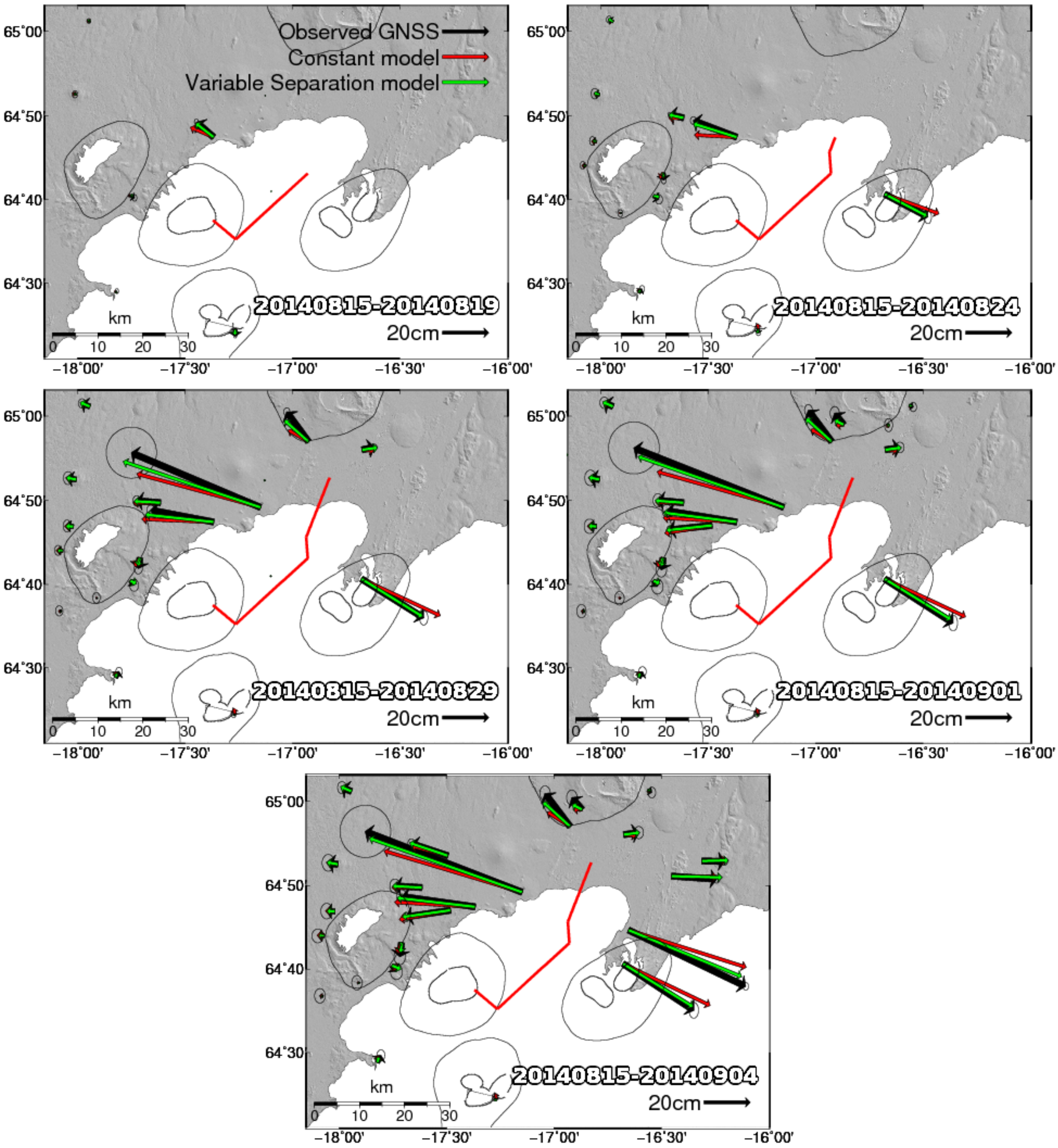

Figure 4.5: GNSS measured displacement vectors (black arrows) during the periods 15/08-19/08 (top left), 15/08-24/08 (top right), 15/08-29/08 (middle left), 15/08-01/09 (middle right) and 15/08-04/09 (bottom), as published in (*Sigmundsson* et al., 2015). The circles indicate the 95% confidence region. Also displayed are the best fit model predictions for the constant, large far field separation (red arrows) and the variable far field separation model (green arrows). The red trace shows the path of the dike used in the modelling.

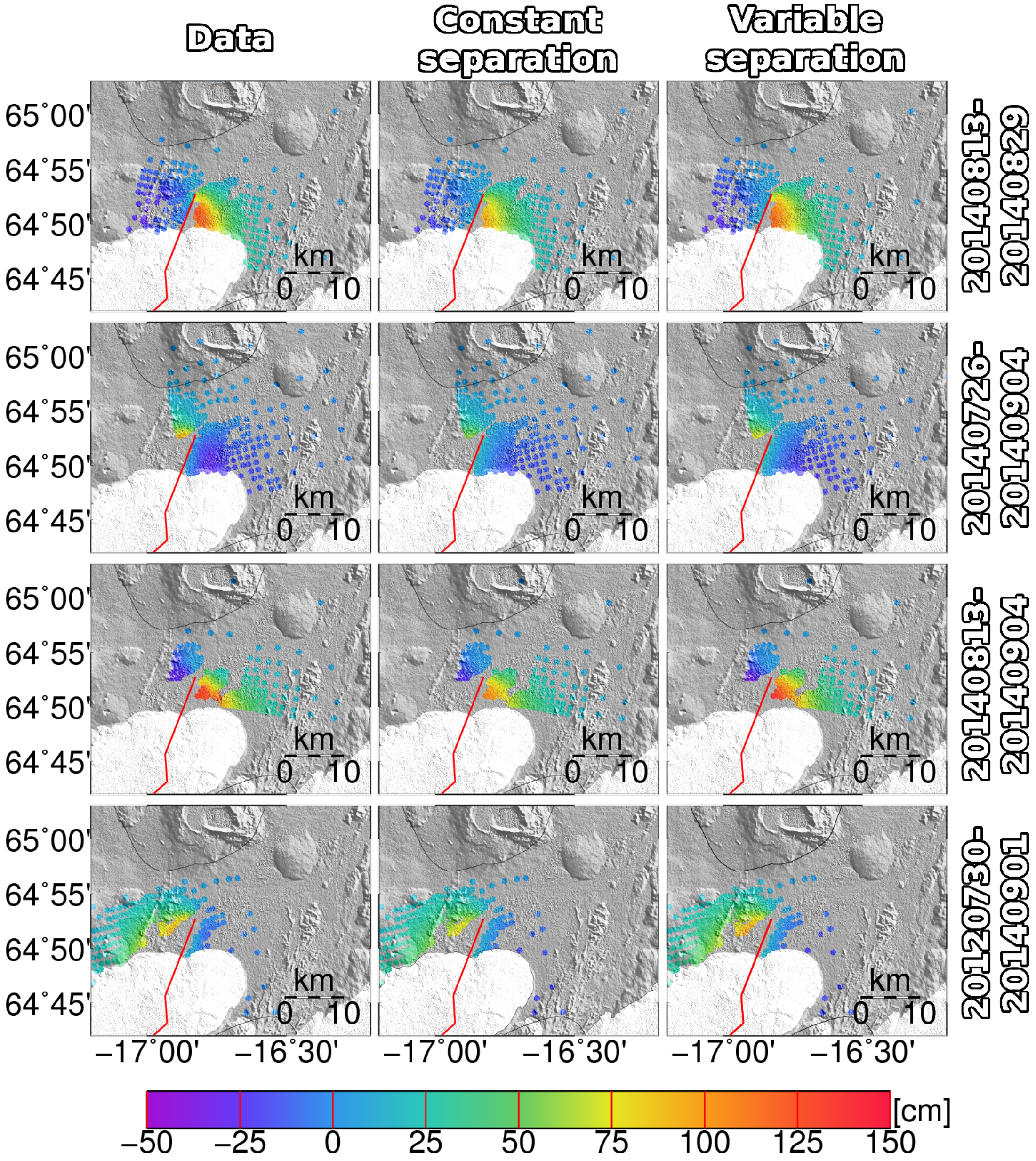

Figure 4.6: Interferograms covering the eruption. The left column shows the unwrapped phase values of the four interferograms 20140813-20140829 (first row), 20140730-20140901 (second row), 20140813-20140904 (third row) and 20120726-20140904 (fourth row). The second column shows the constant far field separation model prediction converted to the radar LOS, and the third column shows the variable far field separation predictions converted to the radar LOS. Both models have uniform overpressure. The constant far-field separation model has a 2 m far field separation imposed on it, while the variable far-field separation model has the plate spreading only applied on the final dike segment. Positive displacements are displacements towards the satellite. White area in the background is area covered by the ice cap. The red trace shows the path of the dike in the model.

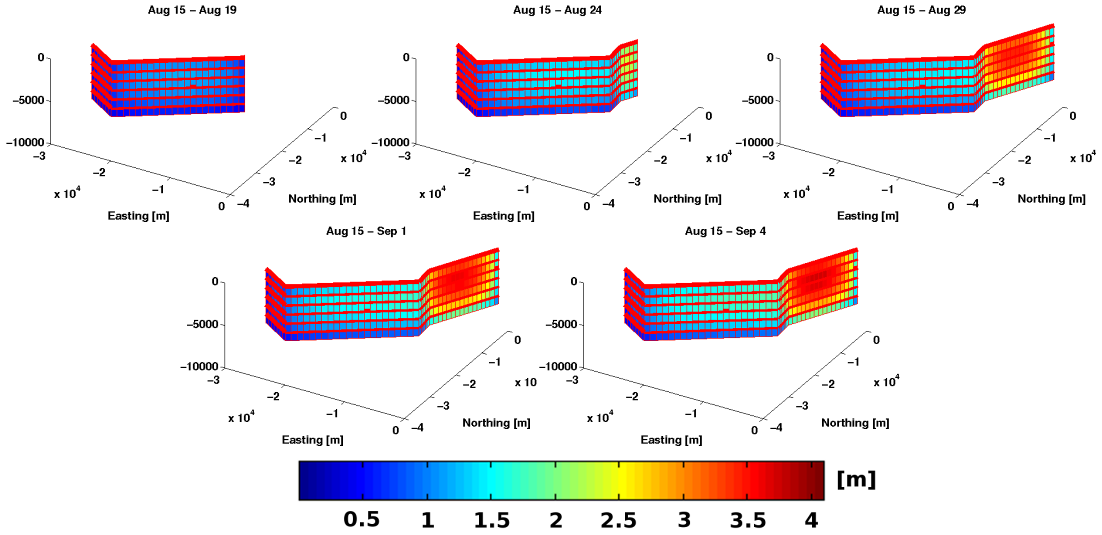

Figure 4.7: The opening in each patch for every time period predicted for the variable far field separation model. During the first two periods, part of the dike was not allowed to open as the dike hadn't yet reached its full extent. The Bárðarbunga caldera (not shown) is on the left side of the figure, the fissures (also not shown) on the right side.

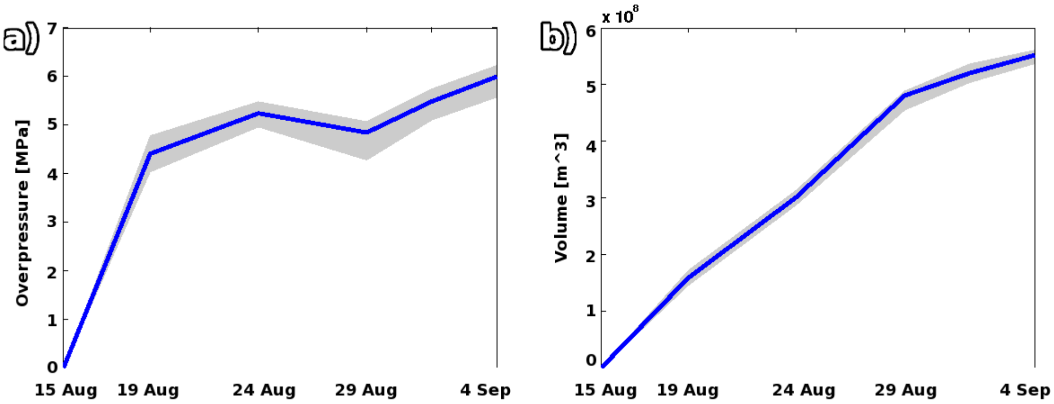

Figure 4.8: Predicted a) magma overpressure and b) volume contained in dike for the variable far field separation model. The blue lines indicate the maximum likelihood prediction of all model realisations. The gray area indicates the 95% probability range of model realisations.

4.4 Discussion

Our modeling results show that the opening required to fit the GNSS and InSAR observations cannot come from the pressure differential between magma and host rock alone. The deviatoric stress field must make a significant contribution to the tractions on the dike, especially in the final segment. We also show that the deviatoric stress field must change significantly between the early dike segments and the final dike segments to create the additional opening required in the final segment.

We propose two mechanisms that could cause the deviatoric stress field to change significantly along the dike. Firstly, the position and orientation of the central rift axis can be different. Although the rift axis is fairly well known north of Vatnajökull ice cap, the majority of the dike surface above the dike is covered by the ice cap, and the location and orientation of the axis in this area remains unclear. The second mechanism could be that part of the stress caused by plate spreading was released by previous eruptions in the area to the south, leading to a gradient in the deviatoric stress field from south to north. The Bárðarbunga system has had 23 confirmed eruptions in historic times, and nearby Grímsvötn volcano over 70 (*Thordarson and Larsen*, 2007), making these systems two of the most active volcanoes in the country. These eruptions, together with previously unknown eruptions that did not break the ice, could have relieved much more of the stress caused by the plate spreading in the region compared to the less volcanically active section of the rift further north.

Our variable deviatoric stress model yields a maximum of just over 4 m opening, accompanied by 0.8 m of maximum strike-slip motion in the final dike segment. This strike-slip motion is consistent with the findings by *Ágústdóttir et al.* (2016), who found exclusively left-lateral strike-slip focal mechanisms ahead of the dike tip during its propagation northward in the final dike segment.

The far field separation found for the variable deviatoric stress model is $2.7^{2.9}_{2.6}$ m, corresponding to 140-150 years of plate spreading. However, this value is highly dependent on the location of the rift, and even a small shift could decrease (if it moves closer to the final dike segment) or increase (if it moves further away) the far field separation, without affecting the fit in our current model setup.

The volume contained within the dike on the 4th of September for the variable deviatoric stress model is $0.55^{0.56}_{0.54}$ km^3 is very close to the volume found in (*Sigmundsson* et al., 2015). The time evolution of the intruded volume also follows a similar pattern, with the rate of volume contained in the dike slowing after the first 2 weeks of the eruption.

4.5 Conclusion

Using the boundary elements method we have modelled the evolution of the Bárðarbunga dike. Although we use only 14 model parameters in this approach, compared to hundreds in the kinematic approach of (*Sigmundsson* et al., 2015), we fit the data almost as well. Our results show that the dike overpressure rose rapidly in the first five days and then remained quasi-static for the remainder of the dike propagation and early eruption period. Our results further show that the deviatoric stress field set up by plate spreading is responsible for the majority of opening, as expected, but only for the last dike segment. The deviatoric stress field for the whole Bárðarbunga volcanic system cannot be explained by a straight rift axis with a constant far-field displacement. In the final, northern segment, the deviatoric stress field agrees with the GNSS plate spreading observations, but in the earlier segments further south it must change orientation and/or magnitude to fit the observations. Despite the dike propagation path itself being consistent with a deviatoric stress field due to uniform plate spreading along a straight rift axis (*Heimisson et al.*, 2015), our results imply that this was not the case; either the rift axis is not straight in this region, or most of the deviatoric stress has been released beneath the ice cap by intrusions, many of which could have been hidden by the ice cap. The 2014 event at Bárðarbunga shows that stress constrained modelling of rifting episodes can not only shed light on the present, but also on the past. The distribution of opening of the dike implies that previously unknown intrusions might have released much of the stress build up over the last two centuries due to plate spreading beneath the Vatnajökull icecap. Especially in difficult to study areas, like subglacial volcanoes or volcanoes in remote locations, mechanical models of the stress field can provide us a glimpse into the past.

References

Ágústdóttir, T., J. Woods, T. Greenfield, R. Green, R. White, T. Winder, B. Brandsdóttir, S. Steinthórsson, and H. Soosalu (2016), Strike-slip faulting during the 2014 Bardarbunga-Holuhraun dike intrusion, central Iceland, *Geophys. Res. Lett.*, *43*, 1495–1503, doi:10.1002/2015GL067423. 4.3, 4.4

Auriac, A., F. Sigmundsson, A. Hooper, K. Spaans, H. Björnsson, F. Pálsson, V. Pinel, and K. Feigl (2014), InSAR observations and models of crustal deformation due to a glacial surge in Iceland, *Geophys. J. Int.*, *198*, 1329–1341, doi:10.1093/gji/ggu205. 4.3

Chen, C., and H. Zebker (2001), Two-dimensional phase unwrapping with use of statistical models for cost functions in nonlinear optimization, *J. Opt. Soc. Am. A*, *18*(2), 338–351, doi:10.1364/JOSAA.18.000338. 4.2

Decriem, J., T. Árnadóttir, A. Hooper, H. Geirsson, F. Sigmundsson, M. Keiding, B. G. Ófeigsson, S. Hreinsdóttir, P. Einarsson, P. LaFemina, and R. A. Bennett (2010), The 2008 May 29 earthquake doublet in SW Iceland, *Geophysical Journal International*, doi:10.1111/j.1365-246X.2010.04565.x. 4.2

Gudmundsson, M., K. Jónsdóttir, A. Hooper, H. E.P., S. Halldŕsson, B. Ófeigsson, S. Cesca, K. Vogfjörd, F. Sigmundsson, T. Högnadóttir, P. Einarsson, O. Sigmarsson, A. Jarosch, K. Jónasson, E. Magnússon, S. Hreinsdóttir, M. Bagnardi, M. Parks, V. Hjörleifsdóttir, F. Pálsson, T. Walter, M. Schöpfer, S. Heimann, H. Reynolds, S. Dumont, E. Bali, G. Gudfinnsson, T. Dahm, M. Roberts, M. Hensch, J. Belart, K. Spaans, S. Jakobsson, H. Gudmundsson, G.B. Fridriksdóttir, V. Drouin, T. Dürig, G. Adalgeirsdóttir, M. Riishuus, G. Pedersen, T. van Boeckel, B. Oddsson, M. Pfeffer, S. Barsotti, B. Bergsson, A. Donovan, M. Burton, and A. Aiuppa (2016), Gradual caldera collapse at Bárdarbunga volcano, Iceland, regulated by lateral magma outflow, *Science*, *[in press]*. 4.1

Hartley, M., and T. Thordarson (2013), The 1874-1876 volcano-tectonic episode at Askja, North Iceland: Lateral flow revisited, *Geochem. Geophys. Geosyst.*, *14*(7), 2286–2309, doi:10.1002/ggge.20151. 4.1

Heimisson, E., A. Hooper, and F. Sigmundsson (2015), Forecasting the path of a laterally propagating dike, *J. Geophys. Res. Solid Earth*, *120*, 8774–8792, doi: 10.1002/2015JB012402. 4.3, 4.3, 4.5

Herring, T. A., R. W. King, and M. S. C. (2010), *GAMIT reference manual*, 10.4 ed. 4.2

Hjartardóttir, A., P. Einarsson, M. Gudmundsson, and T. Högnadóttir (2015), Fracture movements and graben subsidence during the 2014 Bárðarbunga dike intrusion in Iceland, *J Volc Geoth Res*, *310*, 242–252, doi:http://dx.doi.org/10.1016/j.jvolgeores.2015.12.002. 4.3

Hjartarson, A. (2003), Postglacial lava production in Iceland, Ph.D. thesis, University of Copenhagen. 4.1

Hooper, A., B. Ófeigsson, F. Sigmundsson, B. Lund, P. Einarsson, H. Geirsson, and E. Sturkell (2011), Increased capture of magma in the crust promoted by ice-cap retreat in Iceland, *Nature Geoscience*, *4*, 783–786, doi:10.1038/ngeo1269. 4.3

Hooper, A., J. Pietrzak, W. Simons, H. Cui, R. Riva, M. Naeije, A. Terwisscha van Scheltinga, E. Schrama, G. Stelling, and A. Socquet (2013), Importance of horizontal seafloor motion on tsunami height for the 2011 M_w=9.0 Tohoku-Oki earthquake, *Earth and Planetary Science Letters*, *361*, 469–479, doi:10.1016/j.epsl.2012.11.013. 4.3

Jónsson, S., W. Xu, J. Ruch, and T. Wang (2016), Rifting events in the red sea and in iceland observed using sar image offsets, Prague. 4.3

Just, D., and R. Bamler (1994), Phase statistics of interferograms with applications to synthetic aperture radar, *Appl. Opt.*, *33*(20), 4361–4368. 4.2

Kampes, B. (1999), *Delft Object-oriented Radar Interferometric Software: User's manual and technical documentation*, v4.02 ed. 4.2

Mogi, K. (1958), Relations between eruptions of various volcanoes and the deformations of the ground surfaces around them., *Bulletin of the Earthquake Research*, *36*, 99–134. 4.3

Mosegaard, K., and A. Tarantola (1995), Monte carlo sampling of solutions to inverse problems, *Journal of Geophysical Research*, *100*(B7), 12,431–12,447. 4.3

Okada, Y. (1992), Internal deformation due to shear and tensile faults in a half-space, *Bull. Seism. Soc. Am.*, *82*(2), 1018–1040. 4.3

Riel, B., P. Milillo, M. Simons, P. Lungren, H. Kanamori, and S. Samsonov (2015), The collapse of bárdarbunga caldera, iceland, *Geophys J Int*, *202*, 446–453, doi:10.1093/gji/ggv157. 4.1

Schmidt, A., S. Leadbetter, N. Theys, E. Carboni, C. Witham, J. Stevenson, C. Birch, T. Thordarson, S. Turnock, S. Barsotti, L. Delaney, W. Feng, R. Granger, A. Hort, M.C. Höskuldsson, I. Ialongo, E. Ilyinskaya, T. Jóhansson, P. Kenny, T. Mather, N. Richards, and J. Shepherd (2015), Satellite detection, long-range transport, and air quality impacts of volcanic sulfur dioxide from the 2014-2015 flood lava eruption at Bárdarbunga (Iceland), *J. Geophys. Res.: Atmospheres*, *120*, 9739–9757, doi:10.1002/2015JD023638. 4.1

Segall, P. (2009), *Earthquake and Volcano Deformation*, Princeton University Press, Princeton. 4.3

Sigmundsson *et al.*, F. (2015), Segmented lateral dyke growth in a rifting event at Bárdarbunga volcanic system, Iceland, *Nature*, *517*, 191–195, doi:10.1038/nature14111. 4.1, 4.2, 4.3, 4.3, 4.3, 4.3, 4.5, 4.4, 4.5

Spaans, K., and A. Hooper (2016), InSAR processing for volcano monitoring and other near-real time applications, *J. Geophys. Res. Solid Earth*, *121*, doi:10.1002/2015JB012752. 4.2

Sturkell, E., and F. Sigmundsson (2000), Continuous deflation of the Askja caldera, Iceland, during the 1983–1998 noneruptive period, *J. Geophys. Res.: Solid Earth*, *105*(B11), 25,671–25,684, doi:10.1029/2000JB900178. 4.3, 4.3

Thordarson, T., and G. Larsen (2007), Volcanism in Iceland in historical time: Volcano types, eruption styles and eruptive history, *J GEODYN*, *41*(1), 118–152, doi:10.1016/j.jog.2006.09.005. 4.1, 4.4

Chapter 5

Sentinel-1 for large earthquakes: Application to the 2015 Chile and 2016 Ecuador earthquakes

Karsten Spaans[1] and Andrew Hooper[1]

[1] *COMET, School of Earth and Environment, University of Leeds, United Kingdom*

Abstract

With the successful launch and commissioning of the Sentinel-1A satellite, a new era for InSAR deformation measurements has begun. Sentinel-1 has three potential key advantages, compared to previous missions, for the study of large earthquakes and their postseismic response: i) The ability to cover large swaths by using the TOPS acquisition mode, ii) The ability to extract azimuth motions from burst and subswath overlap regions with higher precision than previously possible, and iii) High overall coherence due to consistently short revisit times. Here we test how well these potential advantages are met in practice using two case studies: the 2015 Mw=8.2 Illapel, Chile earthquake and the 2016 Mw=7.8 Ecuador earthquake. In both cases the wideswath mode is able to capture the whole earthquake in a single image. The coregistration precision required to avoid burst edge discontinuities in merged TOPS mode interferograms is easily attained using enhanced spectral diversity, but large azimuth offsets can still result in burst discontinuities. We also demonstrate that both the burst and subswath overlap regions can be effectively used to measure large azimuth offsets, but that measurements of small azimuth offsets are limited by ionospheric disturbances and decorrelation noise. Finally we show that although coherence is generally good, even a twelve day revisit time is not sufficient to extract sufficient signal in areas of marginal coherence due to croplands or heavy vegetation. However, this limitation can be partly offset by using better estimates

of coherence, such as those provided by the newly-developed RapidSAR algorithm.

5.1 Introduction

It is nearly three decades since the first demonstrations of interferometric synthetic aperture radar (InSAR) were published (*Gabriel et al.*, 1989, *Li and Goldstein*, 1990). Since then, it has become one of the main techniques to measure surface deformation (see e.g. *Pinel et al.* (2014)), complimenting other geodetic techniques like GNSS and levelling with its dense spatial sampling and near-global coverage. One of the main areas in which InSAR has made a large impact has been surface motions following seismic events (e.g., *Wright et al.* (2001), *Fialko* (2006)). Arguably, the launch of Sentinel-1 has started a new era of opportunities using InSAR. The high acquisition frequency, and free availability of InSAR data opens up a plethora of possibilities. The Sentinel-1 satellite is unique in that its normal operation mode is the TOPS acquisition mode (*De Zan and Guarnieri*, 2006). This wide-swath mode allows it to greatly increase the width of the area of the Earth surface it acquires from 100 km to 250 km. By increasing the area it covers, it greatly reduces the revisit time, which aids the coherence (*Zebker and Villasenor*, 1992, *Touzi et al.*, 1999) of interferograms.

Sentinel-1 is the first satellite to operate in TOPS mode operationally. The TOPS mode achieves wide coverage by sweeping its radar beam in flight direction, along what is called a burst. After completing the burst sweep, it switches to the second subswath, again sweeping a burst. After doing this one more time in the third subswath, it returns to the first subswath, and restarts the process. Fig. 5.1 provides a schematic overview of the sweeping and switching of the beam between bursts and subswaths. The sweeping of the beam allows each pixel to be imaged by the same number of radar pulses, which is not the case for traditional wide-swath modes (*De Zan and Guarnieri*, 2006). This new mode inevitably leads to several new challenges during processing, particularly when it comes to coregistration accuracy (*Prats-Iraola et al.*, 2012). Due to the sweeping of the beam, the central Doppler frequency varies along each burst. Any misregistration between the master and slave images therefore results in a phase ramp along the burst (*Prats-Iraola et al.*, 2012). At the edges between bursts, this results in a phase discontinuity. TOPS mode therefore requires a far higher coregistration accuracy than was previously required, on the order of a thousandth of a pixel. However, these initial challenges have largely been overcome, and Sentinel-1 data is being used globally to study surface deformation (e.g., (*González et al.*, 2015) and (*Elliott et al.*, 2016)).

The Rapid timeseries InSAR (RapidSAR) method (*Spaans and Hooper*, 2016) was developed to take advantage of the high-quality, continuous data stream offered by Sentinel-1. The focus during the development of the technique was on volcano monitoring, to allow timely extraction of magma movements during intrusive or eruptive events. The method generates high quality coherence estimates for each individual in-

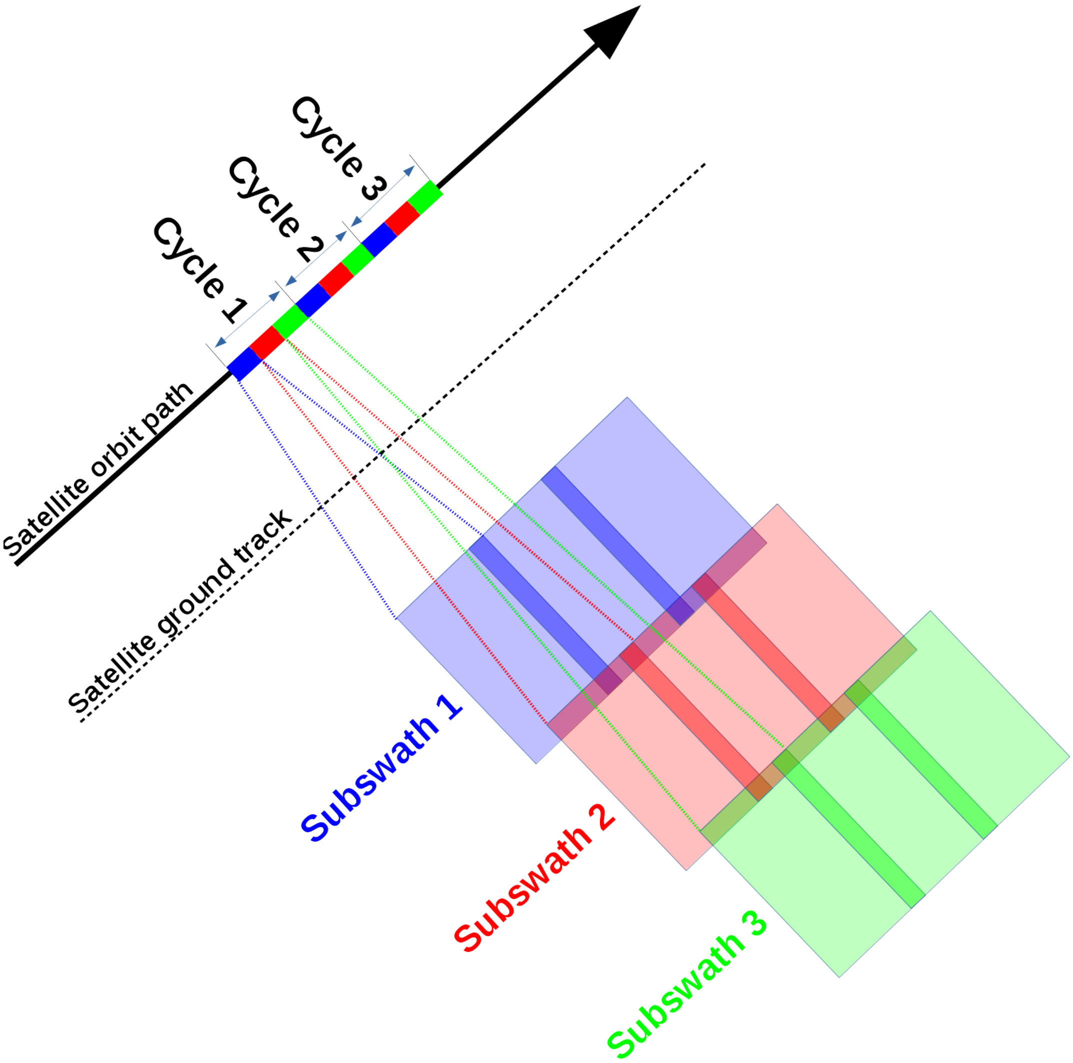

Figure 5.1: Schematic overview of the TOPS acquisition mode. The beam sweeps in flight direction to acquire a burst. It then switches to the next two subswaths to acquire a burst in each of them. The cycle then repeats itself.

terferometric combination. These individual coherence estimates are used to optimize the signal extraction from each interferogram, avoiding the selection compromise inherent in most other time series techniques (*Hooper et al.*, 2011a, *Spaans and Hooper*, 2016). Although the method was developed for near-real time monitoring of volcanoes, the technique can also be applied to other applications.

In this paper, we explore the potential offered by Sentinel-1 for large earthquakes (>M_w=7.5) by looking at two case studies; The Mw=8.2 2015 Illapel, Chile earthquake (*Melgar et al.*, 2016), and the Mw=7.8 2016 Ecuador earthquake. Specifically, we will investigate three potential key advantages of Sentinel-1, compared to other satellites: i) The large coverage achieved by using the TOPS acquisition mode, ii) The azimuth offsets that can be extracted with high precision in the TOPS mode overlap regions and iii) The good overall coherence due to short, consistent revisit times.

5.2 InSAR methods

We use the Gamma software (*Werner et al.*, 2000) to form interferograms, and use the RapidSAR method (*Spaans and Hooper*, 2016) to estimate the coherence. This method uses the amplitude behaviour to find, for each pixel, neighbouring pixels with similar scattering mechanisms. These so-called siblings are then used to calculate the coherence for each pixel using (*Spaans and Hooper*, 2016):

$$\hat{\gamma} = \frac{\left|\frac{1}{n}\sum_{i=1}^{n} M_i \cdot \bar{S}_i\right|}{\sqrt{\frac{1}{n}\left(\sum_{i=1}^{n} M_i \cdot \bar{M}_i \sum_{i=1}^{n} S_i \cdot \bar{S}_i\right)}}, \tag{5.1}$$

where n represents the number of points in the ensemble, M represents the master image signal for an arbitrary point, and S represents the slave image signal. The overline indicates the complex conjugate. Although the boxcar method also uses Equation 5.1 to estimate coherence, the RapidSAR method uses the ensemble of siblings to establish the phase variability, not a rectangular two-dimensional boxcar window. As described in *Spaans and Hooper* (2016), this avoids the majority of problems the boxcar method has with smearing out of high amplitude targets and erroneously high coherence estimates for points in areas of no coherence due to chance. Figure 5.2 shows a comparison between a boxcar and RapidSAR coherence estimate for the area surrounding the town of Esmeraldas in Ecuador. The RapidSAR coherence estimate shows little smearing or erroneously high coherence estimates, leading to a much sharper image. The airfield to the right of the city can be seen in high detail, and close inspection of the city of Esmeraldas even reveals individual city blocks.

In the RapidSAR algorithm, the coherence is used in two ways (*Spaans and Hooper*, 2016). Firstly, it is used to weight the multilooking of interferograms, allowing higher coherence points to dominate the multilook averaging. After multilooking, points with

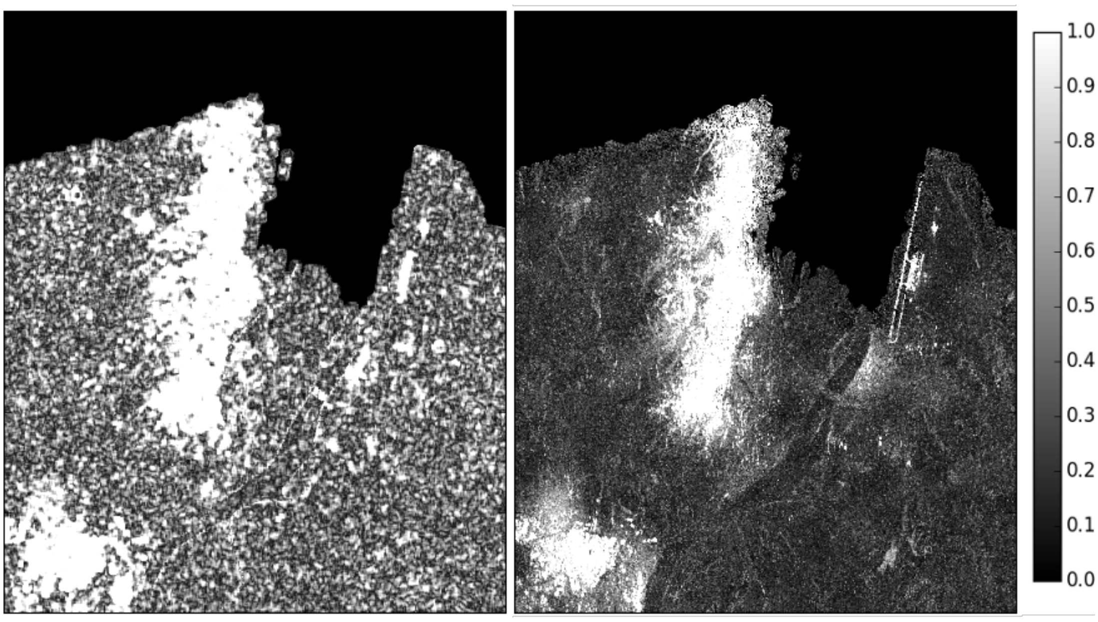

Figure 5.2: Close up view of a) a boxcar and b) a RapidSAR coherence estimate for the ascending co-seismic interferogram of the 2016 Ecuador earthquake (see Section 5.4). A 5x5 window was used for the boxcar coherence estimation, and 9 SAR images were used to estimate siblings for the RapidSAR coherence estimate, with a 41x41 search window. Both coherence estimations were done on full resolution in azimuth, and 5x multilooked in range interferograms, resulting in approximately square pixels.

sufficient coherence are selected. Points can be selected in full resolution, but selection after multilooking reduces the number of false positive selections, that is, points which have an erroneously high coherence estimate by chance. After multilooking and selection, we filter the interferograms using a Goldstein filter (*Goldstein and Werner*, 1998). We use the SNAPHU software (*Chen and Zebker*, 2001) to do the phase unwrapping, i.e. turn the modulo-2π interferometric phase values into a continuous deformation field. We fill any gaps caused by the point selection using a region growing approach (*Hooper et al.*, 2007).

The burst overlap regions of TOPS mode Sentinel-1 images allow for azimuth offsets to be extracted using a process known as spectral diversity (*Scheiber and Moreira*, 2000, *Prats-Iraola et al.*, 2012, *Grandin et al.*, 2016), sometimes referred to as multi-aperture interferometry (MAI). Due to the movement of the satellite platform and the sweeping of the radar beam, there is a Doppler frequency difference between the same pixel in overlap regions between consecutive bursts. Movements in azimuth direction result in a phase difference for the same pixel between the two bursts. By taking the double difference interferogram, these azimuth movements can be extracted in the burst overlap regions. The subswaths also overlap, and thus also allow extraction of azimuth offsets. However, as the difference in Doppler frequency is less, the precision is lower. We use the Gamma software to generate the double difference interferograms in overlap regions.

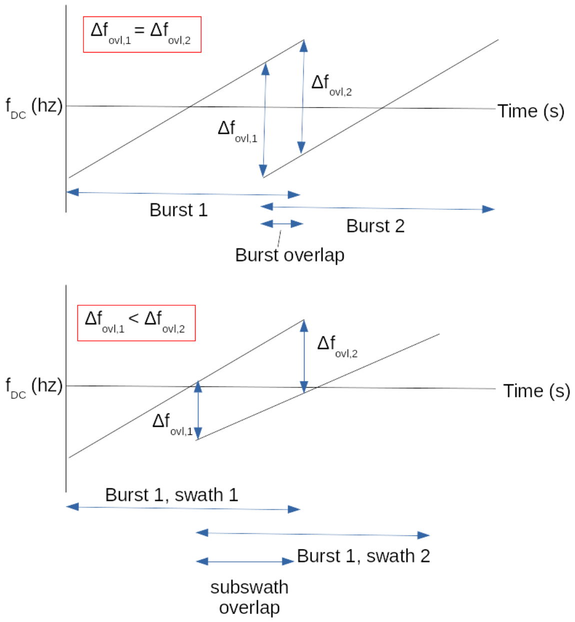

Figure 5.3: Schematic overview of the difference in central Doppler frequency for a) burst and b) subswath overlap regions. Because the central rate of Doppler frequency change with time is the same for bursts in the same swath, the difference in central Doppler frequency is constant in azimuth direction. The different Doppler frequency rate between subswaths results in a variable Doppler frequency difference in azimuth direction.

To transfer this phase difference into azimuth offsets, we use the well-known relation (*Prats-Iraola et al.*, 2012):

$$\Delta x_{azi} = \frac{\phi_{ovl}}{2\pi\Delta f_{ovl}} \frac{1}{\Delta t_{azi}}, \tag{5.2}$$

where Δx_{azi} is the azimuth offset for an arbitrary pixel, ϕ_{ovl} is the phase difference for that pixel in the overlap region, Δf_{ovl} is the difference in central Doppler frequency for that pixel, and Δt_{azi} is the azimuth sampling time per pixel. For burst overlap regions, Δf_{ovl} is constant per subswath. However, due to different sweep rates between subswaths, the Doppler frequency difference changes with azimuth for the subswath overlap regions. This effect is illustrated in Fig. 5.3. Fig. 5.4 gives an overview of the different overlap regions present in the interferometric wide-swath data from Sentinel-1, and the Doppler frequency differences and associated maximum azimuth offsets before wrapping occurs.

5.3 Illapel earthquake data and results

The Mw=8.3 Illapel, Chile megathrust earthquake occurred on the 16th of September, 2015. Studies have shown the fault slipping over a length of 250 km, with peak slip reaching 6 m (*Melgar et al.*, 2016). Despite the large size, only 13 people were killed.

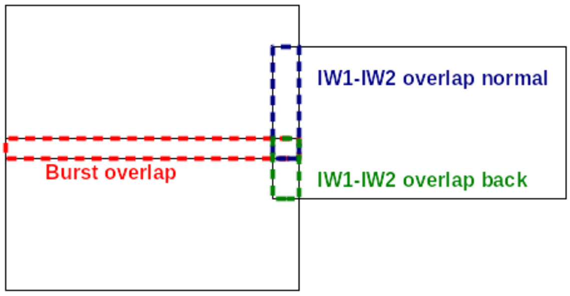

Overlap region	Δf_{ovl} (Hz)	Δx_{azi} (m)
Burst overlap IW1	4801	± 0.71
Burst overlap IW2	4035	± 0.85
Burst overlap IW3	4256	± 0.80
IW1-IW2 overlap normal	1647-2240	± 1.53-2.08
IW1-IW2 overlap back	2284-2648	± 1.29-1.50
IW2-IW3 overlap normal	1360-1531	± 2.24-2.52
IW2-IW3 overlap back	2651-2756	± 1.24-1.29

Figure 5.4: Schematic overview of the different overlap regions of Sentinel-1 interferometric wide-swath mode data. The table shows the Doppler frequency difference Δf_{ovl} and offset ranges Δx_{azi} associated with each overlap region.

However, the earthquake and resulting tsunami caused severe damage, and led to a million people being evacuated from the region (*Melgar et al.*, 2016). The Sentinel-1 satellite imaged the affected area in both the ascending and descending modes. Fig. 5.5 shows interferograms from both an ascending and a descending track. Processing details can be found in the Supplementary Materials, see Chapter A. Even though no optimal 12-day combinations were available, coherence is excellent, and the earthquake is imaged in exquisite detail. As the interferograms have such high coherence, we skipped the point selection in this case, using just weighted multilooking (10 in azimuth and 100 in range) and filtering. The unwrapped interferograms are shown in Fig. 5.6. The interferograms show over 1.5 m of LOS movement, with a slight offset in the area of maximum displacement between the ascending and descending tracks.

The LOS displacements alone have been used to model the slip on the fault on the assumption of a constant squinting direction (*Zhang et al.*, 2016, *Melgar et al.*, 2016). As discussed previously however, the sweeping of the beam within each burst changes the squint angle. Therefore, if there is significant azimuthal movement, we can expect a significant contribution to the phase. We find evidence for this in the wrapped interferograms. Fig. 5.7 shows a close-up view of an area of high deformation of the co-seismic interferogram shown in Fig. 5.5a). Burst discontinuities are clearly visible. Note that these discontinuities are not due to an overall coregistration error, but rather due to motion associated with the earthquake itself, causing a local “misregistration”. The discontinuities are relatively small, and after filtering do not hamper the unwrapping, but this might not always be the case, and regionally-variable co-registration strategies might be required for studies with high azimuth displacements. It is important to take

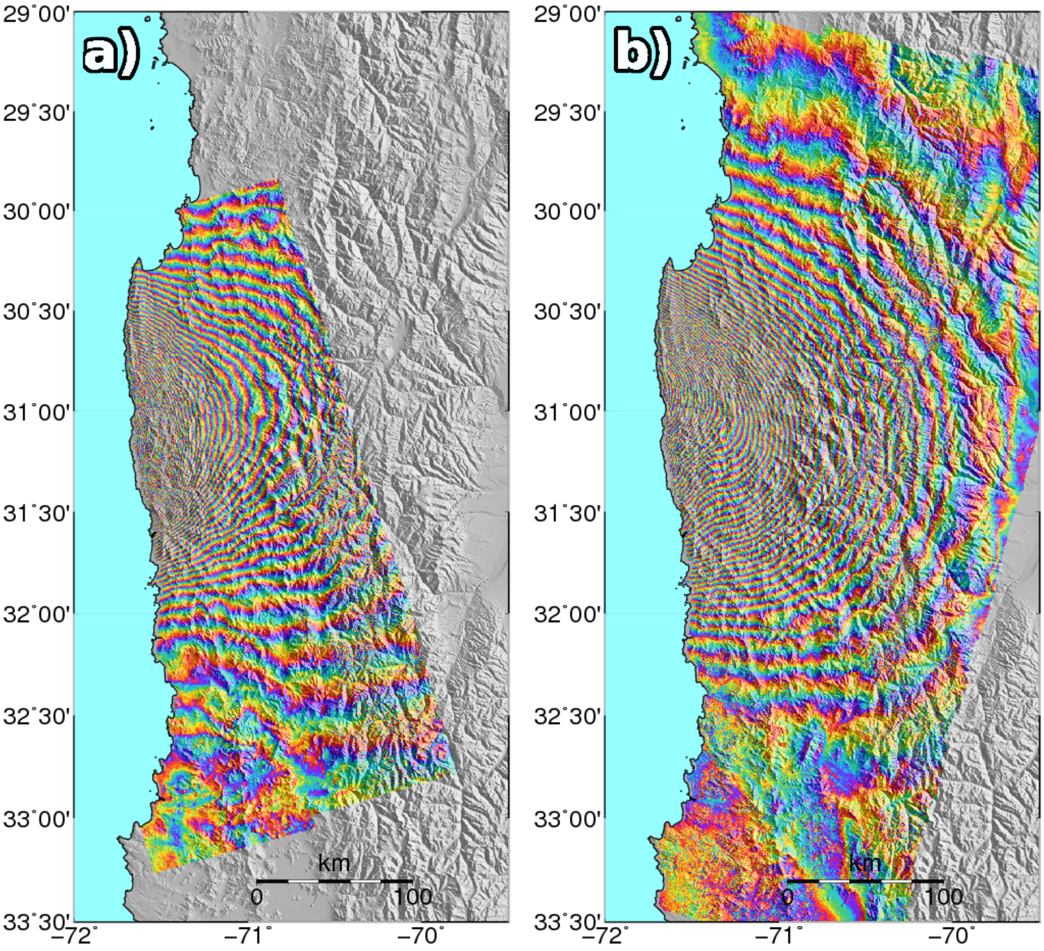

Figure 5.5: Wrapped, unfiltered co-seismic interferograms from the two viewing geometries, covering the Chile earthquake. a) Ascending interferogram (20150826-20150919) multilooked 20 times in azimuth and 100 times in range. b) Descending interferogram (20150731-20150917) multilooked 20 times in azimuth and 100 times in range.

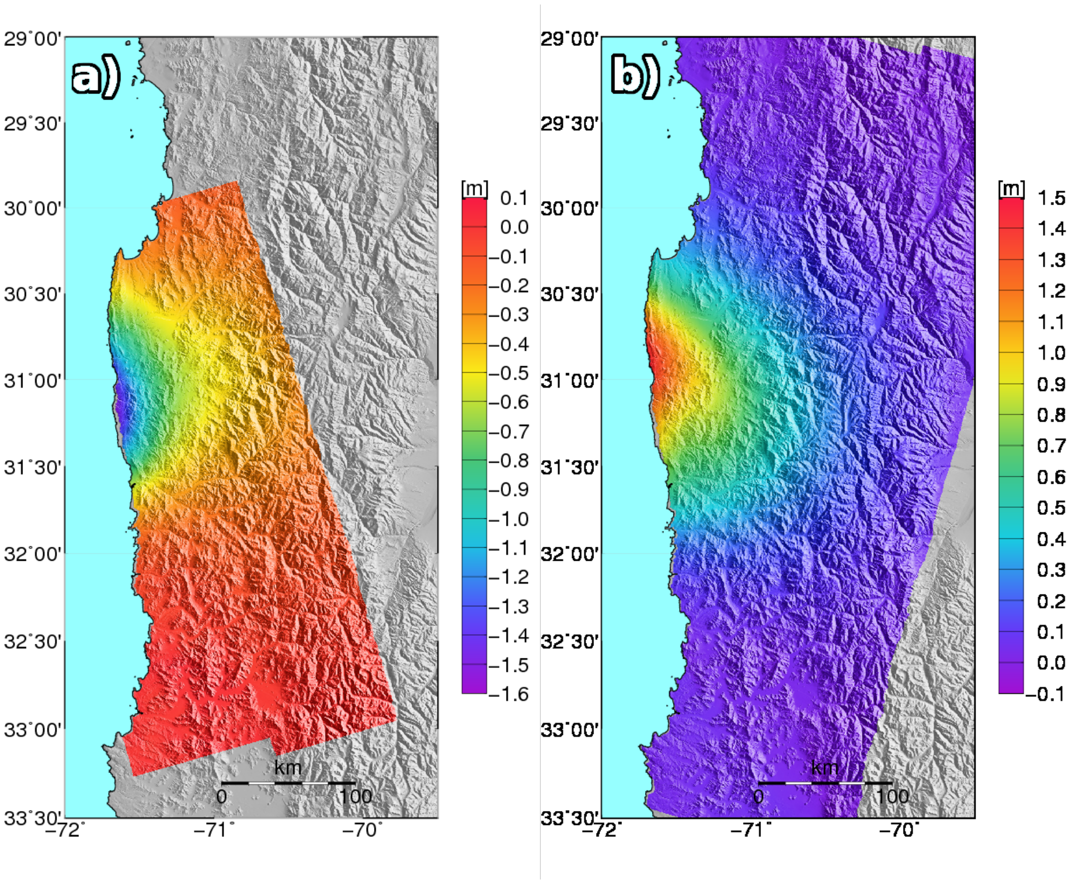

Figure 5.6: Unwrapped co-seismic interferograms from the two viewing geometries, covering the Chile earthquake. a) Ascending interferogram (26-Aug-2015 - 19-Sep-2015) b) Descending interferogram (31-Jul-2015 - 17-Sep-2015). Positive displacements represent movements towards the satellite

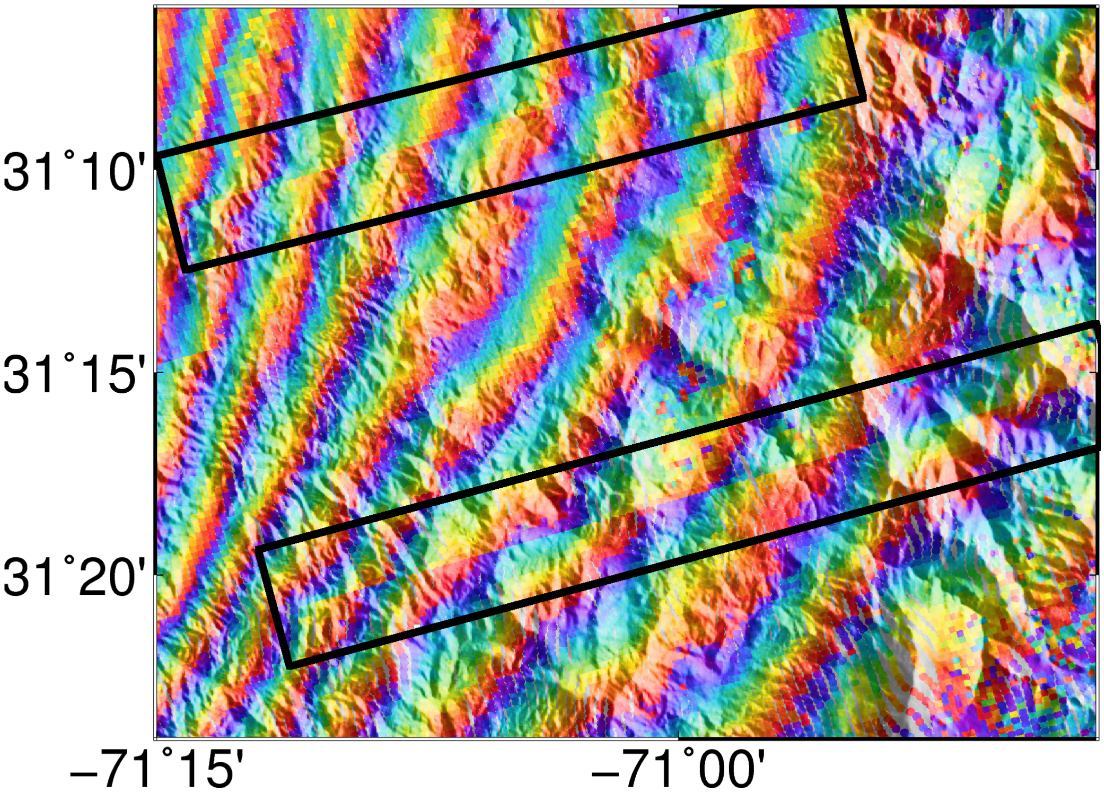

Figure 5.7: Close up look at the ascending interferogram shown in Fig. 5.5a). Two phase discontinuities due to azimuth movements are clearly visible.

the variable squint angle into account when modeling large earthquakes (*González et al.*, 2015).

Grandin et al. (2016) demonstrated that for the large co-seismic deformations, the burst overlap regions can be used to extract the azimuth movements using spectral diversity. As explained in Section 5.2, the subswath overlaps can be used as well. Due to the lower frequency difference (see table in Fig. 5.4), however, the precision is less for the subswath overlap regions compared to the burst overlap regions. Fig. 5.8 shows the azimuth offsets for the burst and subswath overlaps extracted using spectral diversity on the two combinations shown in Fig. 5.5. Within the overlap regions, this increases the number of viewing geometries from 2 to at least 3, and potentially more, where overlap regions of the ascending and descending tracks overlap.

The Sentinel-1 satellite also acquired data covering the post-seismic period. Fig. 5.9 shows wrapped interferograms covering the post-seismic period acquired in the ascending (17-Sep-2015 – 11-Oct-2015) and descending (17-Sep-2015 – 11-Oct-2015) tracks. Both tracks show potential deformation signal in the area of the earthquake, but both also contain significant nuisance signals, mainly tropospheric path delay. Although there are correction methods for tropospheric signals, for single interferograms it remains challenging to correct for atmosphere. As spectral diversity is a double difference method,

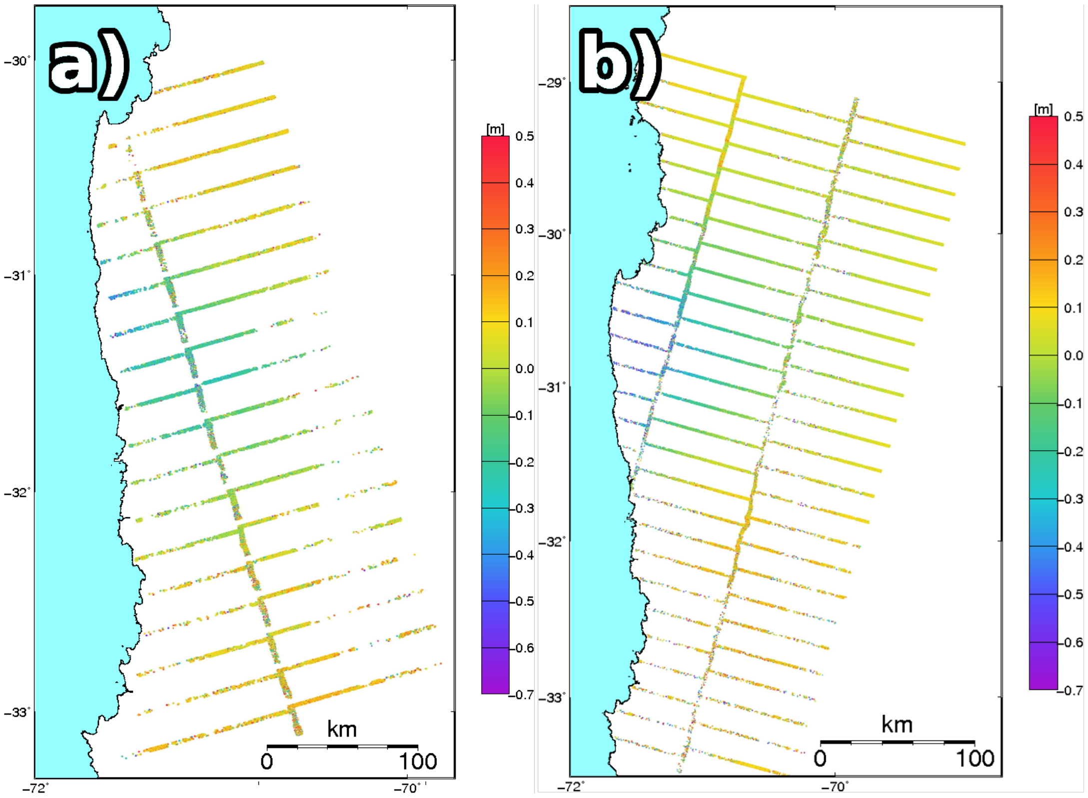

Figure 5.8: Azimuth offsets estimated using spectral diversity on the burst and subswath overlap regions, covering the Chile earthquake. a) Ascending azimuth offsets (26-Aug-2015 - 19-Sep-2015) b) Descending azimuth offsets (31-Jul-2015 - 17-Sep-2015). The azimuth offsets were filtered using a 5 by 5 kernel size median, and only points with a coherence greater than 0.5 are shown.

tropospheric signals largely cancel out. With sufficient coherence and multilooking, the theoretical precision of spectral diversity in the burst overlap regions approaches centimeter level (*Grandin et al.*, 2016), and could thus show post-seismic signal. The azimuth offsets of the burst overlap regions for the two interferograms of Fig. 5.9 are shown in Fig. 5.10. The ascending azimuth offsets of Fig. 5.10a) and the profile of Fig. 5.10c) show some spatially correlated signal of approximately 10 cm in the north part of the scene, which could be related to post-seismic deformation. However, the signal seems to cross the entire scene from west to east, making it much broader than any expected deformation. The signal is also no longer present in other spectral diversity azimuth offsets using the same master and subsequent acquisitions. This indicates that the signal is likely transient, and caused by variations in the total electron content (TEC) of the ionosphere. Due to the difference in squint angle, the radar signal from consecutive bursts travel through different parts of the ionosphere. It the TEC varies in azimuth direction, the radar beam experiences different phase advances, which does not cancel out when forming the double difference interferograms. The descending azimuth offsets of Fig. 5.10b) show no large scale signals, but do show short scale variations, which might also be due to ionosphere, and/or decorrelation noise. The ionospheric interference has a significant detrimental effect on the achievable accuracy. There is also a systematic offset of over 5 cm in the descending azimuth offsets, which indicates some residual misregistration. The most likely reason for this residual misregistration phase component are nuisance terms like ionospheric influence and/or noise due to incorrect coherence masks biasing the double difference phase. Although this misregistration is not severe enough to cause phase discontinuities in the wrapped interferograms, it does show up quite clearly in the double difference spectral diversity interferogram, which should also be taken into account when considering accuracy of said measurements.

5.4 Ecuador earthquake data and results

The Mw=7.8 Ecuador thrust earthquake occurred on April 16th, 2016, killing over 600 people and injuring tens of thousands. Finite fault modelling performed by the USGS shows the fault slipping over a length of approximately 50 km, with peak slip reaching approximately 4 m (*USGS*, 2016). The moment tensor solution shows that there was a right-lateral strike-slip component accompanying the thrusting component, as expected from the convergence rate of the Nazca and South American tectonic plates in the area. The Sentinel-1a satellite acquired SAR images covering the Ecuador earthquake in both an ascending track and a descending track. In the ascending track 18/19 (the track number changes due to crossing the equator), the pre-seismic image was acquired on the 29th of March, and the post-seismic image on the 22nd of April, 6 days after the earthquake. This 24-day interferogram is shown in Figure 5.11a). It is evident that the coherence is poor, even with the very high multilook factor of 20x100 in azimuth and

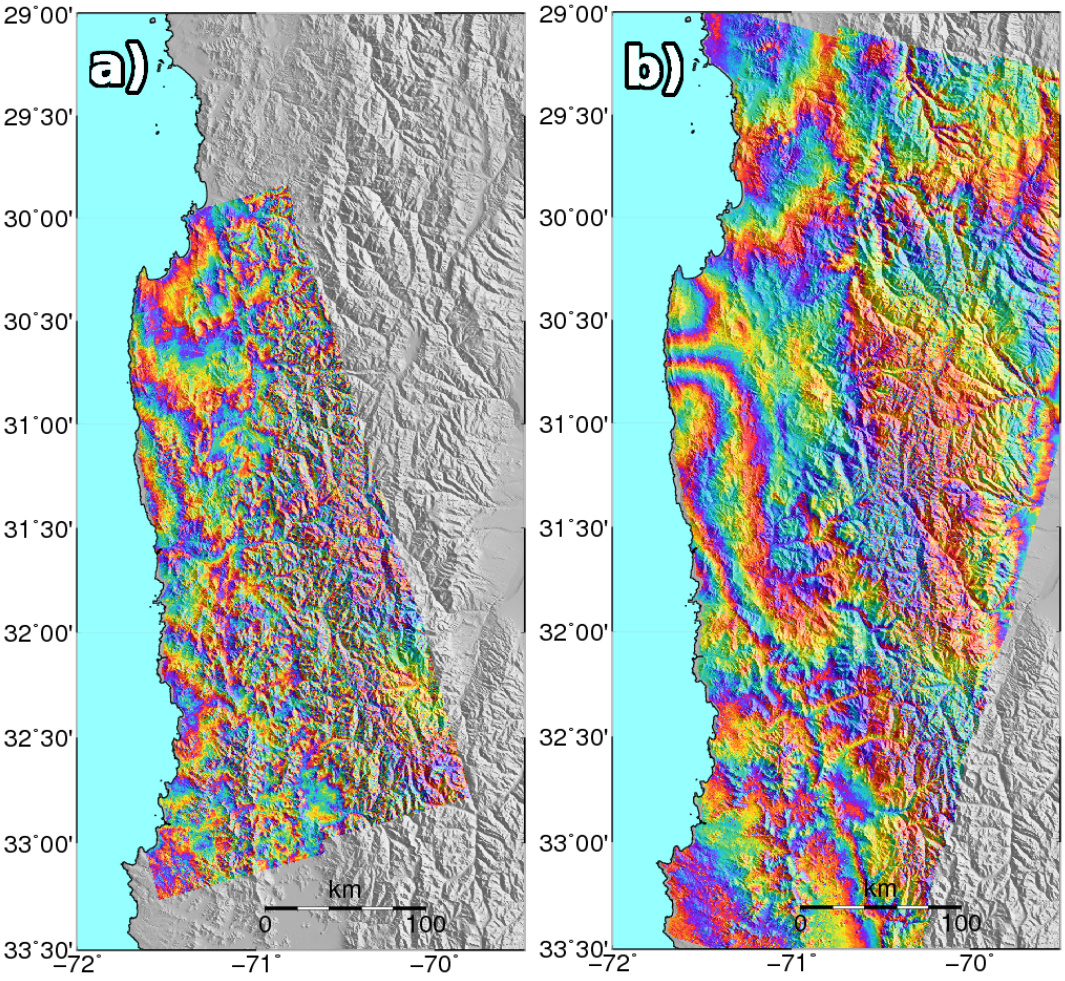

Figure 5.9: Post-seismic wrapped interferograms covering the 2015 Chile earthquake. Panel a) shows the ascending track (19-Sep-2015 – 1-Oct-2015) and panel b) shows the descending track (17-Sep-2015 – 11-Oct-2015). Both interferograms have been multilooked 20 times in azimuth and 100 times in range.

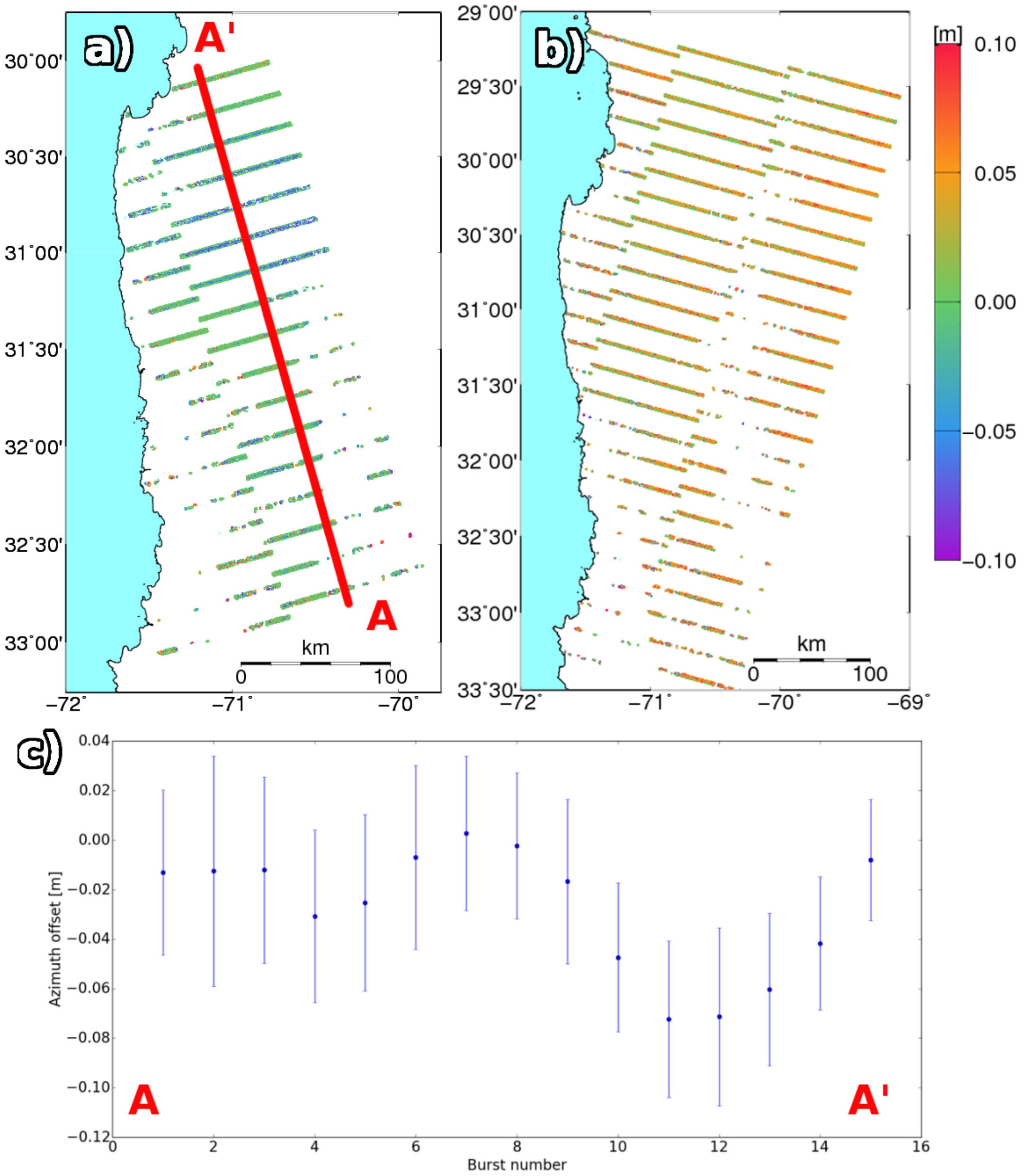

Figure 5.10: Post-seismic azimuth offsets covering the 2015 Chile earthquake. Panel a) shows the ascending track (19-Sep-2015 - 1-Oct-2015) and panel b) shows the descending track (17-Sep-2015 – 11-Oct-2015). The double difference phase was multilooked 10 times in range and 20 times in azimuth. The azimuth offsets were filtered using a 5 by 5 kernel size median, and only points with a coherence greater than 0.5 are shown. Panel c) shows profile A-A' (see red line in panel a), where each dot represents the mean azimuth offset in a burst, and the bars show the standard deviation of the azimuth offset within the burst. The profile shows a clear spatially correlated offset signal in several of the later bursts.

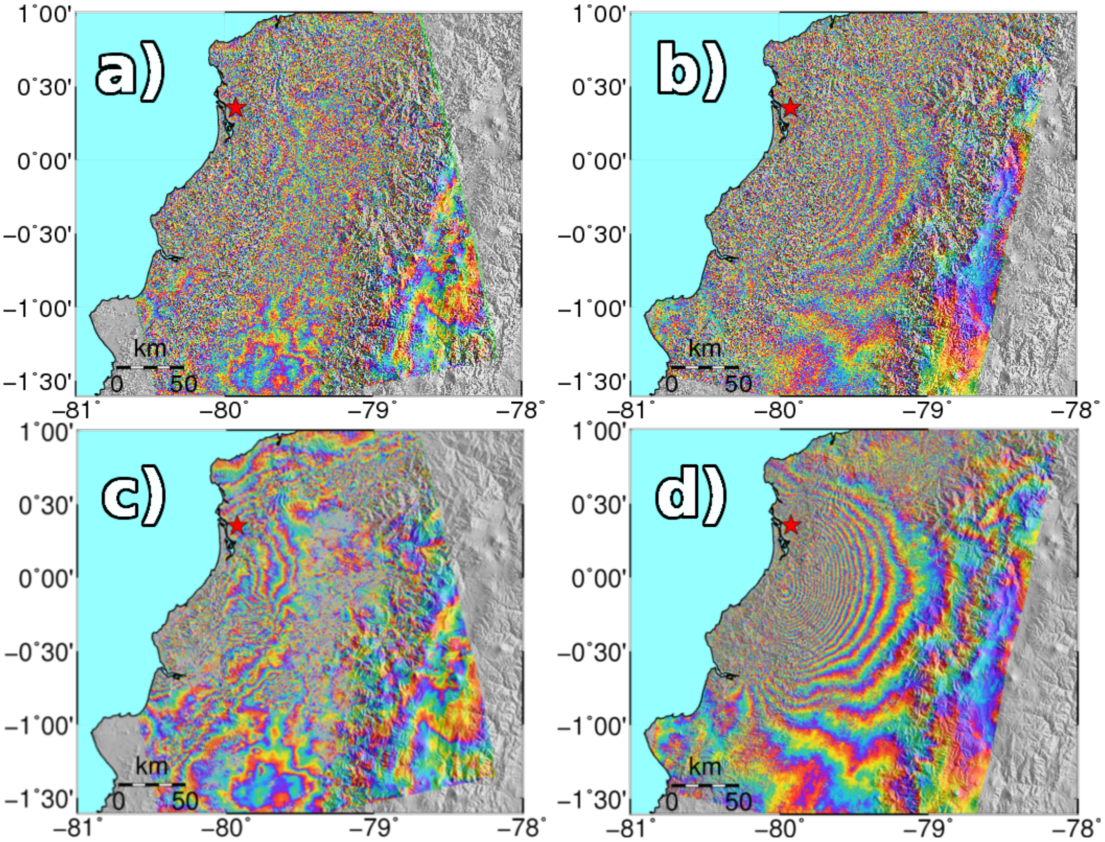

Figure 5.11: Wrapped co-seismic interferograms from the two viewing geometries, covering the Ecuador earthquake. a) Ascending interferogram (29-Mar-2016 - 22-Apr-2016) multilooked 20 times in azimuth and 100 times in range. b) Descending interferogram (12-Apr-2016 - 24-Apr-2016) multilooked 10 times in azimuth and 50 times in range. c) Ascending interferogram after RapidSAR point selection and filtering. d) Descending interferogram after RapidSAR point selection and filtering. The red star indicates the epicenter of the earthquake.

range. The poor coherence is due to heavy vegetation cover in the low lying coastal areas. For the descending acquisitions in track 40, the pre-seismic acquisition was on the 12th of April, and the post-seismic acquisition on the 24th of April, allowing a 12-day interferogram to be formed (Figure 5.11b)). The coherence in the 12-day combination is significantly better than the 24-day interferogram, even though the multilook factor is lower (10x50). There is however still significant decorrelation in the area of high deformation.

Even though the coherence is poor, the RapidSAR weighted multilooking and point selection manages to extract a significant amount of signal, especially in the descending interferogram, but also in the ascending combination. Details on the InSAR data and processing can be found in the supplementary material in chapter A. The interferograms, after filtering, are shown in Figure 5.11c) and d) for the ascending and the descending interferograms, respectively. By using the combination of weighted multilooking, point selection and filtering, we are able to extract signal for most of the area of interest. The

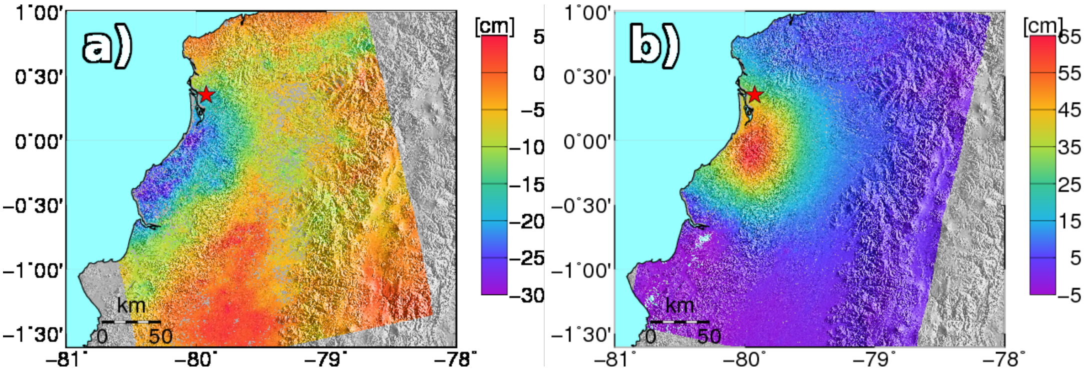

Figure 5.12: Unwrapped co-seismic interferograms for a) the ascending interferogram (29-Mar-2016 - 22-Apr-2016) and b) the descending interferogram (12-Apr-2016 - 24-Apr-2016), covering the Ecuador earthquake. The red star indicates the epicenter of the earthquake.

descending interferogram (Figure 5.11d)) shows a nice pattern of concentric circular deformation. The ascending interferogram (Figure 5.11c)) shows a less smooth fringe pattern, indicating significant tropospheric signal being present.

The unwrapped phase values for the points selected using the RapidSAR approach are shown in Figure 5.12. The ascending, poor coherence interferogram has some aliasing problems at the coast, where point density is low. However, the shape of the co-seismic deformation is well resolved. A shift in the center of deformation can be seen between the ascending and descending interferograms, indicating a strike-slip component to the slip on the fault.

In an attempt to extract more information from the data, we calculated the co-seismic azimuth offsets using spectral diversity. Fig. 5.13 shows the resulting azimuth offsets. The poor coherence has an even larger effect on the azimuth offsets, but the mountainous area to the east provides some measurements. The descending combination shows some high frequency variability between bursts overlaps, most likely due to ionospheric effects, as argued for the Illapel postseismic. The ascending azimuth offsets are spatially smoother between bursts overlaps and indicate approximately zero azimuthal movement.

Even though coherence is poor, the unwrapped interferograms are of sufficient quality to enable us to do some preliminary modelling to assess the slip on the fault. To model the Ecuador earthquake, we used the Okada dislocation model (*Okada*, 1992). We applied a Markov chain Monte Carlo algorithm (*Mosegaard and Tarantola*, 1995, *Hooper et al.*, 2011b) to sample the posterior probability distribution of the slip on each patch. Briefly, this method starts with an initial model realisation, and calculates the likelihood value. A random trial step is then taken for each model parameter, resulting in a trial model realisation. This trial model realisation is accepted based on the ratio between its likelihood ratio and the current model. If the ratio is above a random number between 0 and 1, it is accepted and becomes the new current model. If it is rejected,

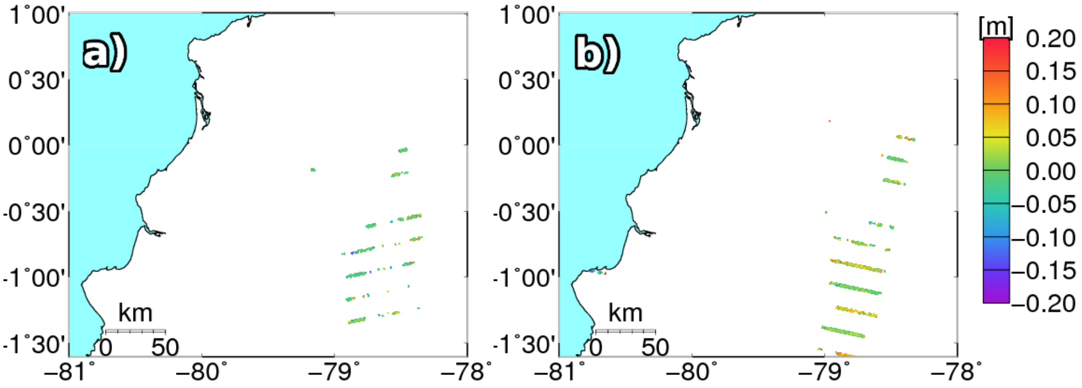

Figure 5.13: Azimuth offsets from spectral diversity for a) the ascending interferogram (29-Mar-2016 - 22-Apr-2016) and b) the descending interferogram (12-Apr-2016 - 24-Apr-2016), covering the Ecuador earthquake. Points were filtered using a 5 by 5 kernel size median filter, and only points with coherence over 0.4 are shown.

the current model remains unchanged. This process is repeated until the *a-posteriori* probability distribution is sufficiently sampled. We adapt the relative step size for all model parameter at regular intervals to ensure equal contribution of each model parameter to the likelihood function, and scale the step size such that at approximately half the model realisations are accepted.

We used the unwrapped interferograms to constrain our modeling. We fix the position of the fault using the constraints from seismic observations. We define a fault 250 kilometers long and 150 kilometers wide, and divide it into 104 patches, 13 in strike, and 8 in dip direction. Our fault plane has a dip of 15 degrees and a strike of 27 degrees. The top of our fault plane is at 700 m depth, and the center of the top of the fault plane is located at 80.86°W and 0.29°. We solve for the slip magnitude and rake of the slip. We assumed the *a-priori* probability for slip to be constant between 0 and 10 m, and 0 outside this range, and for the rake to be constant between 0 (right-lateral strike-slip) and 100 (almost pure dip-slip, with a small left-lateral strike-slip component), again with 0 probability outside this range.

Figure 5.14a) shows the median slip of 500,000 model realisations. The maximum median slip is in the order of 2.5 meters, and there is a significant strike-slip component to the slip. The standard deviation of the slip on each patch is shown in Figure 5.14b). The standard deviations are quite large, but this is largely due to a trade-off between neighbouring patches. This indicates that we constrain the magnitude quite well, but there is some uncertainty in the location of the maximum slip. This trade-off between slip on neighbouring patches is illustrated nicely by Figure 5.15, which shows the histograms of slip on the two highest slipping patches in panel a) and b). Panel c) shows the correlation between the slip on these two patches, which shows a clear inverse relationship.

Our modeling indicates that the slip on the fault was mostly offshore and did not

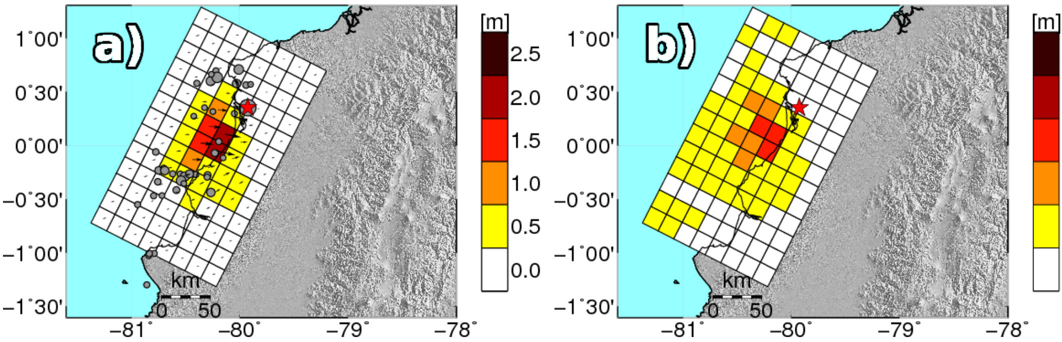

Figure 5.14: a) Median and b) standard deviation of the magnitude of slip for 500000 model realisations. The vectors on panel a) indicate the median rake of the slip. The circles indicate aftershocks with a magnitude greater than 4.5 Mw.

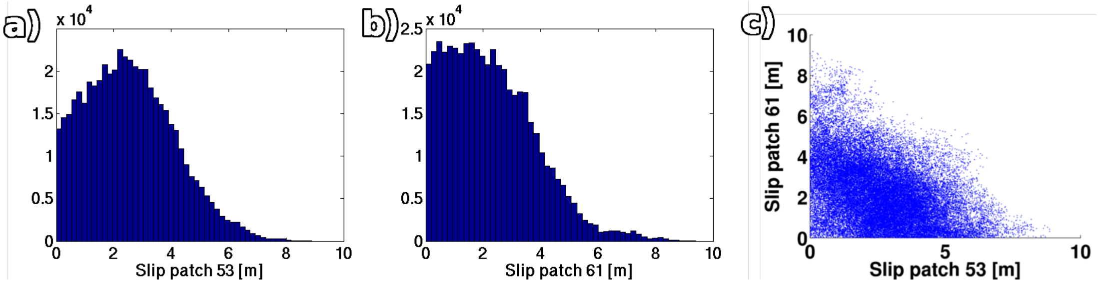

Figure 5.15: Histograms (a) and b)) and correlation scatter plot (c)) of the two highest slipping patches shown in Figure 5.14 a).

reach the trench. The aftershocks, indicated by the grey circles in Figure 5.14 outline the area of high slip nicely as well, lending support for our model. The rake of the slip shows a significant right-lateral strike slip component, which matches the direction of convergence between the Nazca and South-American plate, and is also present in the moment-tensor solutions. Our model maximum a-posteriori probability model predicts a moment magnitude of $7.9 \cdot 10^{20}$ Nm, which is slightly higher to the $7.1 \cdot 10^{20}$ Nm in the USGS catalogue. This small difference can be explained by aftershocks and aseismic slip, and uncertainty in the shear modulus used during modeling. The deformation on the other hand is underestimated by the model, which implies that the assumed fault geometry or rheology are wrong. For rapid modeling response, we relied on prior fault knowledge to speed up the modeling.

5.5 Discussion and conclusions

Since the launch of Sentinel-1 in 2014, it has become clear that the mission is having a large impact on earth surface deformation studies. In the case of both the Chile and Ecuador earthquakes, the wide swath coverage means that the earthquake could be imaged in single interferograms. The fact that the data are freely available, and within hours of acquisition, has led to rapid generation of results, for scientific publication, and also for timely dissemination on social and traditional media.

One of the largest unknowns before the operational use of Sentinel-1 was the extent of problems that would be encountered with burst discontinuities caused by slight misregistrations. Although the coregistration issues with Sentinel-1 interferometric wide swath mode have been largely resolved, the issue of burst discontinuities due to azimuth motions and ionospheric perturbations remains. We show that these discontinuities are not necessarily a problem for filtering and unwrapping.

The Ecuador data demonstrates the value of the RapidSAR method in providing fast, accurate coherence estimates. The combination of weighted multilooking and point selection is shown to be effective at extracting signal from poor quality interferograms. In the case of the Ecuador earthquake, the data processed using RapidSAR was invaluable in producing fast estimates on the magnitude and location of slip.

One of the big opportunities Sentinel-1 TOPS mode offers is the use of the overlap regions to estimate azimuth offsets with high precision. *Grandin et al.* (2016) demonstrated how a three dimensional deformation field could be interpolated using the burst overlaps, although in practise interpolating between burst overlap regions might not be the preferred option. In fact, for modelling purposes, the approach taken by *González et al.* (2015) of including the change in squint angle change within the bursts in the LOS vector for each pixel eliminates the need to calculate azimuth offsets altogether. We show, however, that when a visualistion of azimuthal displacement is desired, also the subswath overlap regions can be used to visualize azimuth offsets in addition to the burst overlaps for large enough displacements. v The Chile post-seismic and Ecuador co-seismic data demonstrate the influence variable ionospheric TEC content can have on estimating azimuth offsets. Although there are theoretical descriptions of the precision achievable with spectral diversity (*Bamler and Eineder*, 2005), these do not take into account ionospheric path delays, which clearly have a significant influence on the measurements, perhaps not on the precision, but certainly on the accuracy. Also, in the case of significant TEC variations in azimuths, the coregistration offset will vary significantly as well. Similar to the case of azimuth motions, a variable coregistration offset would then be required to remove burst discontinuities. The azimuth offsets for the Ecuador earthquake demonstrate the sensitivity of azimuth offsets to coherence. Azimuth offsets are more influenced by decorrelation than LOS interferograms, which limits their use in areas of marginal coherence.

The short revisit time of Sentinel data means that coherence is generally good. However, as the Ecuador data clearly demonstrated, challenging conditions still lead to poor coherence. The difference between the 12 and 24 day combinations shown in Fig. 5.11 clearly argues for 12, or even 6 day repeats when Sentinel-1B becomes operational, in these challenging areas. We argue that an acquisition strategy which takes scattering properties/expected coherence and its seasonal variability into account should be considered.

The two years since the launch of the Sentinel-1 satellite have seen a number of exciting results and methods come to the fore. Here we have shown that Sentinel-1 does offer some key advantages compared to other satellites in terms of coverage, data availability, coherence and measurements of azimuth offsets. We believe there is still a host of opportunities out there to be explored and exploited, and look forward to what the coming years have to bring in terms of InSAR applications.

References

Bamler, R., and M. Eineder (2005), Accuracy of differential shift estimation by correlation and split-bandwidth interferometry for wideband and delta-k SAR systems, *IEEE Geosc. Rem. Sens. Lett.*, *2*(2), 151–155, doi:10.1109/LGRS.2004.843203. 5.5

Chen, C., and H. Zebker (2001), Two-dimensional phase unwrapping with use of statistical models for cost functions in nonlinear optimization, *J. Opt. Soc. Am. A*, *18*(2), 338–351, doi:10.1364/JOSAA.18.000338. 5.2

De Zan, F., and A. Guarnieri (2006), TOPSAR: Terrain observation by progressive scans, *Ieee Transactions On Geoscience And Remote Sensing*, *44*(9), 2352–2360, doi:10.1109/TGRS.2006.873853. 5.1

Elliott, J., R. Jolivet, P. González, J.-P. Avouac, J. Hollingsworth, M. Searle, and V. Stevens (2016), Himalayan megathrust geometry and relation to topography revealed by the Gorkha earthquake, *Nature Geosc*, *9*, 174–180, doi:10.1038/NGEO2623. 5.1

Fialko, Y. (2006), Interseismic strain accumulation and the earthquake potential on the southern San Andreas fault system, *Nature*, *441*(7096), 968–971, doi:10.1038/nature04797. 5.1

Gabriel, A., R. Goldstein, and H. Zebker (1989), Mapping small elevation changes over large areas: Digital radar interferometry, *J GEOPHYS RES*, *94*(B7), 9183–9191. 5.1

Goldstein, R., and C. Werner (1998), Radar interferogram filtering for geophysical applications, *Geophysical research letters*, *25*(21), 4035–4038. 5.2

González, P., M. Bagnardi, A. Hooper, Y. Larsen, P. Marinkovic, S. Samsonov, and T. Wright (2015), The 2014-2015 eruption of Fogo volcano: Geodetic modeling of Sentinel-1 TOPS interferometry, *Geophys Res Lett*, *42*, 9239–9246, doi:10.1002/2015GL066003. 5.1, 5.3, 5.5

Grandin, R., E. Klein, M. Métois, and C. Vigny (2016), Three-dimensional displacement field of the 2015 M_w 8.3 Illapel earthquake (Chile) from across- and along-track Sentinel-1 TOPS interferometry, *Geophys Res Lett*, *43*, doi:10.1002/2016GL067954. 5.2, 5.3, 5.3, 5.5

Hooper, A., P. Segall, and H. Zebker (2007), Persistent scatterer interferometric synthetic aperture radar for crustal deformation analysis, with application to Volcán Alcedo, Galápagos, *Journal of Geophysical Research*, *112*(B7), doi:10.1029/2006JB004763. 5.2

Hooper, A., D. Bekaert, K. Spaans, and M. Arıkan (2011a), Recent advances in SAR interferometry time series analysis for measuring crustal deformation, *Tectonophysics*, *514-517*, 1–13, doi:10.1016/j.tecto.2011.10.013. 5.1

Hooper, A., B. Ófeigsson, F. Sigmundsson, B. Lund, P. Einarsson, H. Geirsson, and E. Sturkell (2011b), Increased capture of magma in the crust promoted by ice-cap retreat in Iceland, *Nature Geoscience*, *4*, 783–786, doi:10.1038/ngeo1269. 5.4

Li, F., and R. Goldstein (1990), Studies of multibaseline spaceborne interferometric synthetic aperture radars, *IEEE Trans Geosci Remote Sensing*, *28*(1), 88–97. 5.1

Melgar, D., W. Fan, S. Riquelme, J. Geng, C. Liang, M. Fuentes, G. Vargas, R. Allen, P. Shearer, and E. Fielding (2016), Slip segmentation and slow rupture to the trench during the 2015, Mw8.3 Illapel, Chile earthquake, *Geophys. Res. Lett.*, *43*, 961–966, doi:10.1002/2015GL067369. 5.1, 5.3, 5.3

Mosegaard, K., and A. Tarantola (1995), Monte carlo sampling of solutions to inverse problems, *Journal of Geophysical Research*, *100*(B7), 12,431–12,447. 5.4

Okada, Y. (1992), Internal deformation due to shear and tensile faults in a half-space, *Bull. Seism. Soc. Am.*, *82*(2), 1018–1040. 5.4

Pinel, V., M. Poland, and A. Hooper (2014), Volcanology: Lessons learned from synthetic aperture radar imagery, *J. Volcanol. Geotherm. Res.*, *289*, 81–113, doi:10.1016/j.jvolgeores.2014.10.010. 5.1

Prats-Iraola, P., R. Scheiber, L. Marotti, S. Wollstadt, and A. Reigber (2012), TOPS interferometry with TerraSAR-X, *IEEE Trans Geosc Rem Sens*, *50*(8), 3179–3188, doi:10.1109/TGRS.2011.2178247. 5.1, 5.2

Scheiber, R., and A. Moreira (2000), Coregistration of interferometric SAR images using Spectral Diversity, *IEEE Trans. Geosci. Remote Sens.*, *38*(5), 2179 – 2191, doi:10.1109/36.868876. 5.2

Spaans, K., and A. Hooper (2016), InSAR processing for volcano monitoring and other near-real time applications, *J. Geophys. Res. Solid Earth*, *121*, doi:10.1002/2015JB012752. 5.1, 5.2, 5.2, 5.2

Touzi, R., A. Lopes, J. Bruniquel, and P. Vachon (1999), Coherence estimation for SAR imagery, *IEEE Trans Geosc Rem Sens*, *37*(1), 135–149. 5.1

USGS (2016), M7.8 coastal ecuador earthquake of 16 april 2016, *http://earthquake.usgs.gov/earthquakes/eqarchives/poster/2016/20160416.jpg*. 5.4

Werner, C., U. Wegmüller, T. Strozzi, and A. Wiesmann (2000), Gamma SAR and interferometric processing software, *ESA Envisat Symposium*. 5.2

Wright, T., E. Fielding, and B. Parsons (2001), Triggered slip: observations of the 17 August Izmit (Turkey) earthquake using radar interferometry, *Geophys. Res. Lett.*, *28*(6), 1079–1082. 5.1

Zebker, H., and J. Villasenor (1992), Decorrelation in interferometric radar echoes, *IEEE Trans. Geosci. Remote Sens.*, *30*(5), 950–959. 5.1

Zhang, Y., G. Zhang, E. Hetland, X. Shan, S. Wen, and R. Zuo (2016), Coseismic fault slip of the september 16, 2015 Mw 8.3 Illapel, Chile earthquake estimated from insar data, *Pure Appl. Geophys.*, *73*, 1029–1038, doi:10.1007/s00024-016-1266-3. 5.3

Chapter 6

Discussion and conclusions

My aim in this thesis was to take a step forward in using InSAR to monitor volcanoes. In Section 1.4 I defined four objectives. In this chapter, I want to return to these objectives, and discuss how Chapters 2 to 5 tie in with these objectives. In will finish this chapter by discussing the outlook for InSAR for volcano monitoring and other applications.

6.1 Rapid and accurate coherence estimation

The first objective I wanted to achieve with this thesis was to develop a method to rapidly and accurately estimate coherence for newly processed interferograms, to obtain high-quality deformation measurements over volcanic areas in near-real time. In Chapter 2, I described the RapidSAR method, a new method I developed to allow InSAR to be used to monitor volcanoes in near-real time. Previously, when fast results were required, the boxcar ensemble coherence method was used. However, this method struggles in areas of marginal coherence. Alternatively, time series methods provide good quality point selections, but these methods are generally slow, and select one set of points for the entire time series, forcing these methods to compromise between losing signal in some interferograms to reduce noise in others. In the RapidSAR method, I use a time series of interferograms to identify for each pixel an ensemble of siblings, points that have similar scattering characteristics. I then use this ensemble of siblings to estimate an individual coherence estimate for each interferogram. By using the sibling ensemble, I overcome most of the problems that the boxcar method has, while at the same time retaining an individual coherence estimate to avoid the selection compromise inherent to most other time series methods. By assuming the sibling information does not change rapidly in time, I can estimate the ensemble of siblings for each pixel on an initial data set. When a new image is acquired, this means I only have to take into account interferometric combinations made with this new image. This reduces the amount of data that has to be processed significantly, speeding up processing times.

In Chapters 2 and Chapter 5, I compare coherence estimates using the boxcar method to estimates using the RapidSAR method. The comparison clearly shows that the RapidSAR method is able to extract a higher quality coherence estimate, as it does not suffer from the smearing effect of high amplitude targets, and generates far less erroneously high coherence estimates in incoherent areas. Furthermore, in Chapter 2, I use phase variability of selected points as a proxy for the quality of point selections using the different coherence estimates to quantify the coherence estimate quality. In the same chapter, I compare the RapidSAR selection to a small baseline time series method selection. This comparison clearly shows that the small baseline method suffers from the selection compromise, and that RapidSAR is able to extract more signal while reducing the overall noise levels in the final products.

Chapters 4 and 5 describe examples of InSAR studies where RapidSAR was successfully applied. Chapter 4 describes modeling of the Bárðarbunga eruption, which was constrained using InSAR data that was processed using RapidSAR (for the scenes where sufficient images were available). Although RapidSAR was developed with mainly volcano monitoring in mind, Chapter 5 shows that RapidSAR can also be successfully applied to studying and rapid response to seismic events. As especially the 2016 Ecuador earthquake demonstrates, the weighted multilooking and selection procedure of RapidSAR is able to extract useful deformation signal from very poor quality interferograms.

6.2 Finding and correcting for nuisance deformation signals

The second objective was to explore different sources of deformation around volcanoes that might mimic magmatic movement, and finding ways to correct for them. In Chapter 3, I describe a joint InSAR and GNSS study covering the Katla volcanic system and the surrounding area. In the early naughties, continuous GNSS stations were starting to become operational in the area. Although limited in number, these stations showed interesting movements away from the central caldera for several years, which were interpreted as being caused by increased pressure in the magma chamber (*Sturkell et al.*, 2008). In Chapter 3, I use a larger number of GNSS stations, and a long time series of InSAR images to show that no deformations which could be associated with pressure increase in the magma chamber could be detected. In fact, the initial GNSS stations that showed the movement away from the caldera follow the regional trend of surrounding stations.

I compared the InSAR and GNSS deformation measurements to predictions by a GIA model (*Schmidt et al.*, 2012), and managed to show that the deformations seen could be explained by the viscous response of the earth to melting ice caps around Iceland. This study was a good example of deformation signals caused by other processes being able to mimic magmatic signals. The improved availability of InSAR measurements, and our improved ability to extract signal from these interferograms, will likely prove vital to pinpoint the source of deformation, allowing us to continue to better separate magmatic signals from "nuisance" deformation signals. Our ability to remove these signals often relies on models. To that end, I have been involved in two studies involving the modelling of surface deformations caused ice mass change studies during my PhD. These two studies resulted in new insights into the rheology beneath Iceland (*Auriac et al.*, 2013, 2014).

6.3 Advanced modelling of InSAR

The third objective was to utilize InSAR to constrain advanced models to make inferences about stress changes. In Chapter 4, I used the BEM to model the 2014 Bárðarbunga rifting episode. Simple kinematic dislocation models were used to perform initial modelling (*Sigmundsson* et al., 2015), which showed a relatively shallow dyke which opened several meters in certain areas, as well as shearing tens of centimeters. In Chapter 4, I used the BEM method to infer the stresses that resulted in the opening previously inferred. Specifically, I tested if the hypothesis of a uniform plate spreading used in previous studies (*Heimisson et al.*, 2015) holds. I showed that in the final dyke segment, the opening and shearing of the dyke an be explained well by the plate spreading observed north of the fissure by GNSS. However, in earlier dyke segments further south, the same plate spreading rate cannot explain the observations, and magma overpressure alone fits the deformation observations. This implies that the deviatoric stress field due to plate spreading must change from north to south. Chapter 4 is a good example of why it is important to use more advanced, mechanical modelling methods. The BEM allowed me to constrain the stresses involved directly, providing information on the physical realism of models and the stress field during the rifting event.

6.4 Unique properties of Sentinel

The final objective was to explore how the unique characteristics of the Sentinel satellite system can help us better study and monitor volcanoes and other surface deforming processes. In Chapter 5 I explored the effectiveness of Sentinel-1 in studying large earthquakes using data from two major earthquakes in South America.

Sentinel-1 currently has a 24-day revisit time over tectonically active regions, and an improved 12-day revisit time in certain areas. Although for many regions this 24-day revisit time might suffice (assuming there is flexibility in the case of events), in Chapter 5 I found that the 2016 Ecuador data clearly showed that for areas with particularly challenging surface conditions like dense vegetation, a 12-day revisit time provides far superior coverage of signals.

Before operational dissemination of Sentinel-1 data began, it was unsure if the required coregistration precision was going to be achievable on a consistent basis. For the Ecuador and Chile earthquakes, I showed that the overall coregistration accuracy needed to avoid consistent burst overlap discontinuities is easily achievable through spectral diversity, even in the presence of significant azimuth movements in the co-seismic interferograms. I also show, however, that these azimuth movements do create local phase discontinuities, which may or may not hamper filtering and unwrapping.

One of the advantages of the TOPS acquisition mode that Sentinel-1 uses is that it allows us to extract azimuth movements with potentially high precision. For the Chile earthquake, I showed that besides the burst overlap regions, the subswath overlap regions can be used as well, assuming the deformations are large enough. I further discussed that ionospheric influence will be a limiting factor in our ability to extract small signals. All in all, Sentinel-1 has resulted in a big step forward for the study of large earthquakes.

6.5 Outlook

The aim I had while working on this thesis was to develop a methodology that allows InSAR to be used as a volcano monitoring tool. RapidSAR is the result of this work, and presents a step towards full integration of InSAR into near-real time volcano monitoring. The algorithm has been successfully applied using data from volcanic (and seismic) events. It is currently being applied to process all data over Iceland as part of the FutureVolc programme (*Jordan et al.*, 2013). At the University of Leeds, an processing system is being developed that will consistently and automatically process all tectonically and volcanically active regions worldwide. Integration of at least parts of the RapidSAR methodology into this system is also planned. Although this system will process all data of interest, it would still be preferable to have RapidSAR, or similar processing methodologies, taken up by volcano observatories. This will ensure timely interpretation of data, and integration with other near-real time monitoring techniques. Another viable option would be to ensure rapid delivery of relevant data from the global processing system to observatories. Either option would allow InSAR to be integrated into the volcano monitoring pipeline in a systematic and robust way.

Although RapidSAR has been developed as part of the Iceland-based FutureVolc programme, it can contribute to volcano monitoring worldwide. With this in mind, one of the most challenging surface types for InSAR volcano applications remains jungle type vegetation (*Ebmeier et al.*, 2013). RapidSAR remains largely untested in these type of regions, however, the method should to be able to extract any significant signal present. Once a region is completely decorrelated, it becomes impossible to extract deformation information from the interferograms, as the signal-to-noise ratio approaches zero. The key in these regions is to have short baselines, to minimize the effect of changes in vegetation on the coherence. Volcanoes covered by dense jungle type vegetation will always remain challenging, but if there is signal present in the interferogram, RapidSAR should be able to extract most of it. I will therefore hopefully be able to convince other volcano observatories to integrate RapidSAR into their monitoring arsenal.

The superior quality of the coherence images produced by RapidSAR have potential as well. Coherence images have been used for land cover classification (*Engdahl and Hyyppä*, 2003) and natural disaster damage detection (*Watanabe et al.*, 2016). Both these techniques would benefit greatly from utilizing a sibling based ensemble during the coherence estimation to generate higher quality coherence images.

From a processing point of view, challenges also remain. Firstly, we do not deal with atmospheric signals. Atmosphere can be estimated from the InSAR data itself if there is a time series, but this does not tend to work well towards either end of the time series. Weather models are another option, but are currently too slow to integrate into a near-real time processing chain. For large signals, this is not a problem, as the influence of atmospheric path delays is reduced, but for smaller signals, atmosphere remains a problem. Improvements to the unwrapping algorithm used could be made to add information from the time domain to aid the phase unwrapping. The fact that RapidSAR does not select the same set of points in each interferogram complicates this, but this is a challenge that we should be able to overcome. Finally, integrating a timeseries inversion method with RapidSAR would increase its effectiveness in applications outside volcano monitoring, which require long time series to extract continuous motion. As with the phase unwrapping, gaps in the data are a challenge, but one that we should be able to overcome by exploiting time and space information.

Sentinel-1, TerraSAR-X, Cosmo-SkyMed, and similar satellites are imaging the world with unprecedented coverage, and methods like RapidSAR help us to extract the maximum amount of deformation measurements from these data. However, measurements are not enough, it is interpretations that are required. To interpret our measurements, we must first understand the type of process that causes them. Our understanding of many of these processes is expanding, but still limited. In this thesis I discussed the influence of ice mass changes around volcanoes, and other processes like geothermal water movements could have a similar mimicing effect. Spatial and temporal coverage of these areas is key in identifying the cause of deformations. Being aware of these processes for future studies is also not enough, we must be careful with previous studies, where such high resolution deformation measurements were not available.

The second piece of the puzzle to attach interpretations to the deformation measurements are models. Although many simplified models exist, which certainly have their place in early studies, additional insights often come from more advanced modeling, which can tell us about the relevant forces and stresses involved with the magma movements. Increased computational capabilities make these models more practical, and we should continue encourage their integration into volcano modeling. The holy grail here is really to being able to use these models in a predictive way. Although we are not there yet, we are getting close. The large amount of data that is being generated, and which should generate unprecedented amounts of deformation maps over volcanoes. With this, our knowledge of the stress fields surrounding these volcanoes should increase, potentially allowing us to predict the onset and location of eruptions.

The question that has not been answered is how these data will be interpreted. Manual inspection of each image will perhaps no longer be feasible, in which case automatic detection of volcanic (or other sources) deformation becomes a requirement. Novel machine learning techniques like neural networks are able to identify objects in images based on a training set, and these techniques might be applicable to deformation maps, allowing the automated system to automatically highlight areas that are likely deforming. Finally, rapid, (semi-)automated modelling could be integrated into monitoring systems, to further enhance the value created from the automatic global processing systems.

As I have mentioned several times in this thesis, Sentinel-1 arguably hails in a new era for InSAR deformation measurements. By using the TOPS acquisition mode, the satellite is able to cover large swaths of the Earth surface, reducing the revisit time, and thus improving coherence. It is vital that for deformation studies the coherence is optimized by keeping the revisit time low, especially for areas with for example dense vegetation. Any significant issues with processing Sentinel-1 data have been resolved, but challenges remain with large azimuth motions, ionospheric signals and atmospheric path delays, which should be tackled as soon as possible. The overlap regions allows plenty of opportunities as well. If the ionospheric signal in these measurements is removed or reduced, they will provide a very accurate measurement of azimuth motions, with numerous applications. Sentinel-1, and new techniques like RapidSAR will no doubt have an enormous impact on our ability to measure and monitor deformations globally. All in all, an incredibly exciting and challenging time lies ahead for InSAR.

References

Auriac, A., K. Spaans, F. Sigmundsson, A. Hooper, P. Schmidt, and B. Lund (2013), Iceland rising: Solid Earth response to ice retreat inferred from satellite radar interferometry and visocelastic modeling, *J. Geophys. Res. Solid Earth*, *118*, 1331–1344, doi:10.1002/jgrb.50082. 6.2

Auriac, A., F. Sigmundsson, A. Hooper, K. Spaans, H. Björnsson, F. Pálsson, V. Pinel, and K. Feigl (2014), InSAR observations and models of crustal deformation due to a glacial surge in Iceland, *Geophys. J. Int.*, *198*, 1329–1341, doi:10.1093/gji/ggu205. 6.2

Ebmeier, S., J. Biggs, T. Mather, and F. Amelung (2013), Applicability of insar to tropical volcanoes: Insights from Central America, *Geological Society, London, Special Publications*, *380*, 15–37, doi:10.1144/SP380.2. 6.5

Engdahl, M., and J. Hyyppä (2003), Land-cover classification using multitemporal ERS-1/2 InSAR data, *IEEE Trans. Geosc. Rem. Sens.*, *41*(7), 1620–1628. 6.5

Heimisson, E., A. Hooper, and F. Sigmundsson (2015), Forecasting the path of a laterally propagating dike, *J. Geophys. Res. Solid Earth*, *120*, 8774–8792, doi:10.1002/2015JB012402. 6.3

Jordan, C., F. Sigmundsson, K. Vogfjord, M. Gudmundsson, I. Kristinsson, S. Loughlin, E. Ilyinskaya, A. Hooper, A. Kylling, C. Witham, C. Bean, A. Braiden, M. Ripepe, and F. Prata (2013), Futurevolc: A European volcanological supersite observatory in Iceland, a monitoring system and network for the future, *2013 IEEE IGARSS*. 6.5

Schmidt, P., B. Lund, T. Árnardóttir, and H. Schmeling (2012), Glacial isostatic adjustment constrains dehydration stiffening beneath Iceland, *Earth Planet Sc Lett*, *359-360*, 152–161, doi:10.1016/j.epsl.2012.10.015. 6.2

Sigmundsson *et al.*, F. (2015), Segmented lateral dyke growth in a rifting event at Bárdarbunga volcanic system, Iceland, *Nature*, *517*, 191–195, doi:10.1038/nature14111. 6.3

Sturkell, E., P. Einarsson, M. Roberts, H. Geirsson, M. Gudmundsson, F. Sigmundsson, V. Pinel, G. Gudmundsson, H. Olafsson, and R. Stefansson (2008), Seismic and geodetic insights into magma accumulation at Katla subglacial volcano, Iceland: 1999 to 2005, *J Geophys Res-Sol Ea*, *113*(B3), B03,212, doi:10.1029/2006JB004851. 6.2

Watanabe, M., R. Thapa, T. Ohsumi, H. Fujiwara, C. Yonezawa, N. Tomii, and S. Suzuki (2016), Detection of damaged urban areas using interferometric SAR coherence change with PALSAR-2, *Earth, Planets and Space*, *68*(131), doi:10.1186/s40623-016-0513-2. 6.5

Appendix A

Supplemental material Chapter 5

This chapter describes the processing parameters used on the InSAR data presented in chapter 5. Section A.1 decribes the processing parameters for the data covering the Illapel earthquake, and section A.2 decribes the processing parameters for the data covering the Ecuador earthquake.

A.1 Illapel earthquake data

We processed two tracks covering the 2015 Illapel, Chile earthquake. The descending track was acquired in relative orbit number 156, and we used 16 images between 7 July 2015 and 7 June 2016. The master image was chosen to be 31 July 2015, and the first image to be obtained after the earthquake was on 17 September 2015. The ascending track was acquired in relative orbit 18, and we used 8 images acquired between 9 July 2015 and 18 November 2015. The master image was chosen to be 26 August 2015, and the first image after the earthquake was on the 19th of September, 2015.

We performed the RapidSAR sibling identification (*Spaans and Hooper*, 2016) using all available combinations. A search window size of 41 pixels was used, and the amplitude and amplitude difference thesholds were set to 5% and 15% difference, respectively. Due to the high coherence of the interferograms, we deviated from the default RapidSAR procedure by skipping the point selection. We used weighted multilooking (*Spaans and Hooper*, 2016) (10 times in azimuth and 100 times in range), and filtered the interferograms using the Goldstein filter (*Goldstein and Werner*, 1998). To unwrap the interferograms, we used the open source Snaphu software (*Chen and Zebker*, 2001).

A.2 Ecuador earthquake data

We processed two tracks covering the 2016 Ecuador earthquake. The descending track was acquired in relative orbit number 40, and we used 17 images acquired between 18 April 2015 and 24 April 2016. The master image was chosen to be 12 April 2016, and the first image to be acquired after the earthquake was on 24 April 2016. The ascending track was acquired in relative orbit 18/19. There are two orbit numbers, as the scene crosses the equator in the ascending direction, changing the relative orbit number. We processed 8 images between 28 April 2015 and 22 April 2016. The master image was chosen to be 29 March 2016, and the first image to be acquired after the earthquake was on 22 April 2016.

We used all available interferometric combinations to identify the RapidSAR siblings. We used a search window size of 41 pixels, and amplitude and amplitude difference thresholds of 5% and 15%, respectively. We used weighted multilooking factors of 20 times in azimuth and 100 times in range for the low coherence ascending scene, and 10 times in azimuth and 50 times in range for the higher coherence descending scene. We selected points using a phase variance threshold of 15 deg^2, and used the Goldstein filter to filter the resulting interferograms. We unwrapped the interferograms using the open source Snaphu software.

References

Chen, C., and H. Zebker (2001), Two-dimensional phase unwrapping with use of statistical models for cost functions in nonlinear optimization, *J. Opt. Soc. Am. A*, *18*(2), 338–351, doi:10.1364/JOSAA.18.000338. A.1

Goldstein, R., and C. Werner (1998), Radar interferogram filtering for geophysical applications, *Geophysical research letters*, *25*(21), 4035–4038. A.1

Spaans, K., and A. Hooper (2016), InSAR processing for volcano monitoring and other near-real time applications, *J. Geophys. Res. Solid Earth*, *121*, doi:10.1002/2015JB012752. A.1